NORTHWESTERN UNIVERSITY

Advances in Fundamental Single Molecule Studies with Surface-Enhanced Raman Spectroscopy

A DISSERTATION

SUBMITTED TO THE GRADUATE SCHOOL

IN PARTIAL FULFILLMENT OF THE REQUIREMENTS

for the degree

DOCTOR OF PHILOSOPHY

Field of Chemistry

By

Alyssa B. Zrimsek

EVANSTON, ILLINOIS

December 2016

ABSTRACT

Advances in Fundamental Single Molecule Studies with Surface-Enhanced Raman Spectroscopy

Alyssa B. Zrimsek

Surface-enhanced Raman spectroscopy (SERS) is a powerful technique for characterizing molecular systems. It combines the chemical selectivity of vibrational spectroscopy with plasmonic signal enhancement to achieve the ultimate limit of detection – a single molecule. By overcoming the effects of ensemble averaging, single molecule SERS (SMSERS) probes distributions in molecular interactions and dynamics. Deeper insight into phenomena normally obscured by ensemble averaging is attainable, including the principle mechanisms of SERS, the behavior of single molecules (SM) on plasmonic surfaces, and site-specific chemistries.

The research reported in this dissertation contributes to the advancement of the fundamental understanding of SMSERS. First, an introductory review of SMSERS is provided, encompassing the early development and current status of the technique. Second, a critical analysis of the isotopologue and bianalyte SM proofs is presented. This includes

experimental considerations and the proposal of more rigorous thresholds for reliably verifying SM detection. Third, the SM capability of discrete Ag nanopyramids fabricated by nanosphere lithography is proven. These nanoparticle arrays are a reproducible alternative to the commonly used, chemically-synthesized nanoparticles which are inherently polydisperse in shape, size, and aggregation state. In addition, they provide the first example of SMSERS without nanogaps. Fourth, the potential use of SM anti-Stokes SER scattering to measure temperatures of plasmonic junctions is investigated. It was demonstrated that SM temperature measurements with SERS are complicated by uneven enhancement of the anti-Stokes and Stokes SER scattering. Necessary considerations for reliably measuring temperatures with SERS are covered. Fifth, the generality of the relative intensity fluctuations between vibrational modes in SMSERS is explored. It was found that the signal fluctuations are not the result of surface diffusion and are wavelength dependent, occurring when excited on molecular resonance. Finally, this dissertation concludes with a review of recent applications and a discussion on future directions for SMSERS. All of the aforementioned research studies have contributed to the central goal of transitioning SERS into a robust technique for studying SM chemistry, allowing us to resolve the complexity of molecular interactions.

Professor Richard P. Van Duyne

Research Advisor

Acknowledgements

I first met Professor Richard P. Van Duyne during my REU at Northwestern University. I had such a great experience working in his group, I decided to return for graduate school. I need to thank him for all of his support and guidance as my research advisor. Professor Van Duyne allowed me to take charge of my own research, while always being ready to help when needed and constantly inspire me with new ideas. His enthusiasm for science has brightened all my endeavors over the past 5 years. My committee members Professor Tamar Seideman, Professor Toru Shiozaki, and my qualifier chair Professor Emily Weiss also deserve immense gratitude for their help shaping me into the scientist I am today. Their pertinent questions forced me to think about my research in new ways and to continue learning. I also want to thank my collaborator Professor George C. Schatz. His insight and wisdom have helped all of us answer many challenging research questions.

I was drawn to the Van Duyne Group because of the friendly, collaborative atmosphere. I have been surrounded by an amazing group of researchers who are always willing to work together to brainstorm ideas and troubleshoot problems. I want to thank Dr. Samuel Kleinman for being my mentor when I joined the group, introducing me to SERS experiments and teaching me about instrumentation. I would also like to thank the many collaborators and coworkers who have worked alongside me, whether for a small or large

research endeavor: Nolan Wong, Dr. Eric Pozzi, Dr. Anne-Isabelle Henry, Emma Vander Ende, Dr. Fernanda Cardinal, Dr. Bhavya Sharma, Michael McAnally, Dr. Bogdan Negru, Emily Sprague-Klein, Cassie George, Dr. Lauren Buchanan, and Dr. Stephanie Zaleski. Without their help this research would not have been possible.

I must also extend a heartfelt thanks to my parents, Kate and Robert Zrimsek, and my siblings, Darrelle Windham, Jeremy Zrimsek, and Chad Zrimsek, for all of their unwavering support during my graduate studies. It is through their encouragement and advice that I am able to be here today. Lastly, I would like to thank my fiancé, Cameron Gross for all of his help. We met 5 years ago during the first day of TGS orientation and have experienced the entirety of graduate school together. I look forward to our future adventures together!

List of Abbreviations

AFM	Atomic Force Microscopy
aS	Anti-Stokes
BG	Brilliant Green
BPE	1,2-Bis-(4-pyridyl)-ethylene
CE	Chemical Enhancement
CT	Charge Transfer
CTAB	Cetyltrimethylammonium Bromide
CV	Crystal Violet
DDA	Discrete Dipole Approximation
DFS	Dark Field Scattering
DMAB	4,4-Dimercaptoazobenzene
EC	Electrochemical
EF	Enhancement Factor
EM	Electromagnetic
FDTD	Finite Difference Time Domain
FON	Film Over Nanospheres
FWHM	Full-Width Half Maximum
GM-SERS	Gap-Mode Surface-Enhanced Raman Spectroscopy
HHD	Half-Half Dilution

HOMO	Highest Occupied Molecular Orbital
HRTEM	High-Resolution Transmission Electron Microscopy
LDF	Large Dilution Factor
LSPR	Localized Surface Plasmon Resonance
LT	Low Temperature
LUMO	Lowest Unoccupied Molecular Orbital
MV	Methyl Viologen
NB	Nile Blue
NSL	Nanosphere Lithography
NRS	Normal Raman Scattering
***p*-ATP**	*Para*-Aminothiophenol
***p*-NTP**	*Para*-Nitrothiophenol
PS	Polystrene
PSF	Point Spread Function
QD	Quantum Dot
R6G	Rhodamine 6G
R800	Rhodamine 800
RBTIC	Rhodamine B Isothiocyanate
REP	Raman Excitation Profile
RR	Resonance Raman
S	Stokes
SASERS	Single-Aggregate Surface-Enhanced Raman Spectroscopy
SEF	Surface-Enhanced Fluorescence

SEM	Scanning Electron Microscopy
SERS	Surface-Enhanced Raman Spectroscopy
SM	Single Molecule
SMSERS	Single Molecule Surface-Enhanced Raman Spectroscopy
SMTERS	Single Molecule Tip-Enhanced Raman Spectroscopy
SPM	Scanning Probe Microscopy
TDDFT	Time-Dependent Density Functional Theory
TEM	Transmisson Electron Microscopy
TERS	Tip-Enhanced Raman Spectroscopy
TP	Thiophenol
UHV	Ultra-High Vacuum

Table of Contents

List of Tables

List of Figures

CHAPTER 1

Introduction to Single Molecule SERS

1.1. Motivation and Background

Molecular systems and nanoscale environments are neither static nor simple. Ensemble averaging obscures the vast complexity and heterogeneity of all accessible molecular microstates. Important information with regard to site-specific behavior, distributions in molecular dynamics and interactions, and chemistry cannot be obtained on the ensemble level. Over the past several decades, several analytical techniques have been used to overcome the effects of ensemble averaging including single molecule fluorescence spectroscopies,[1–5] scanning probe microscopies (SPM),[6–8] and force spectroscopies such as magnetic and optical tweezers.[9–11] While many of these single molecule (SM) techniques can provide information about the molecular electronic states, surface topography, or even the behavior of a single molecule under stretching or torsional mechanical force, most are limited by their lack of chemical specificity. Unlike the aforementioned techniques, Raman spectroscopy can access the chemical content of a molecular system through the observation of molecular vibrations. As such, Raman scattering provides great chemical specificity, and yields what is often referred to as a chemical or vibrational "fingerprint." In 1997, Nie and Emory[12] and Kneipp et al.[13] both claimed SM detection of resonant dyes by surface-enhanced Raman spectroscopy (SERS). These first observations of single molecule SERS (SMSERS) opened new possibilities towards obtaining the vibrational

spectrum of a single molecule. SMSERS is ideal for obtaining deeper insight into the mechanisms of SERS, the behavior of single molecules on surfaces and in plasmonic cavities, and chemistries obscured by ensemble averaging.*

1.1.1. Scope of the Introduction

This introduction sets the stage for the following chapters by covering the progress in SMSERS towards understanding the fundamental behavior of single molecules with high chemical sensitivity. First, we introduce Raman spectroscopy, the electromagnetic and chemical enhancement mechanisms, and Rhodamine 6G, a quintessential molecule in SMSERS. Then, we highlight the development and current understanding of the phenomena underlying SMSERS, which includes hot spots and plasmonic substrate design, signal fluctuations and heterogeneity, and verifying SM detection. For a thorough coverage of the field of SMSERS, we direct the reader to relevant reviews on SMSERS EFs[15] and characterizing hot spots.[16]

1.1.2. Raman Spectroscopy

Raman spectroscopy is a method for studying the inelastic scattering of light. An excitation photon induces a dipole in the molecule yielding inelastic light scattering. Stokes scattering occurs when the scattered photon is lower in energy than the incident photon by a quantum (or more) of vibrational energy (positive Raman shift relative to excitation), leaving the molecule in the first vibrational state (v=0 to v=1). Anti-Stokes scattering occurs when the scattered photon is higher in energy than the incident photon (negative

*This Chapter is reproduced in part with permission from reference [14]. Copyright 2016 American Chemical Society.

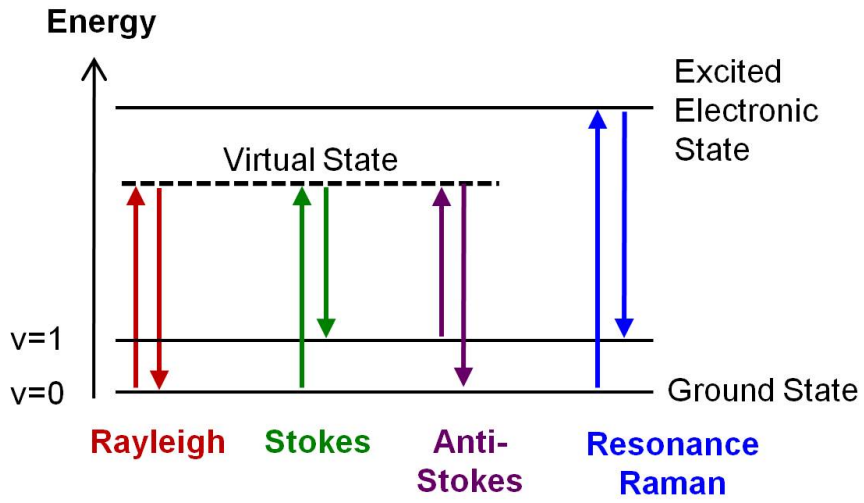

Figure 1.1. Energy diagram showing the spectroscopic transitions involved in Rayleigh (elastic scattering), Raman (inelastic scattering), and resonance Raman scattering. Two pathways can be found in Raman: either the scattered photon has a lower energy than the adsorbed photon (Stokes scattering), or inversely, the scattered photon has a higher energy than the scattered photon (anti-Stokes scattering).

Raman shift relative to excitation), leaving the molecule in the ground state (v=1 to v=0), as visualized in Figure 1.1. The Stokes and anti-Stokes scattering are symmetric about the Rayleigh (i.e., elastic) scattering (v=0 to v=0). Under equilibrium conditions, the intensity of the anti-Stokes normal Raman scattering is related to the populations of excited vibrational states which follow a Boltzmann distribution. While Raman spectroscopy provides detailed chemical and structural information of molecular systems, the efficiency of the inelastic scattering process is very low, as only 1 in 10^8 photons is Raman scattered. To enhance the inelastic scattering probability, resonance Raman (RR)

scattering occurs when the incident laser is near an electronic transition of the molecule of interest, increasing the signal by an additional factor of 10^2-10^6.[17–20]

1.1.3. Electromagnetic and Chemical Enhancement Mechanisms

To achieve single molecule detection with Raman spectroscopy requires the large signal enhancements of SERS. The two main mechanisms of signal enhancement are the electromagnetic (EM) mechanism and the chemical enhancement (CE) mechanism. Enhancement factors (EF) are used to quantify the signal enhancement and are generally defined as the ratio of the normalized SERS signal over the normalized normal Raman signal of the same molecule, as follows:

$$EF_{SERS} = \frac{I_{SERS}/N_{SERS}}{I_{NRS}/N_{NRS}} \tag{1.1}$$

where I_{SERS} and I_{NRS} are the intensities of the SERS and normal Raman spectroscopy (NRS) signals, respectively, and N_{SERS} and N_{NRS} the number of molecules contributing to the SERS and NRS signals, respectively.

The EM mechanism of SERS relies on a phenomenon known as the localized surface plasmon resonance (LSPR). The LSPR is the collective oscillation of surface conduction electrons of noble metal plasmonic nanoparticles that are smaller in size compared to the wavelength of incoming light. A physically intuitive diagram of the LSPR is shown in Figure 1.2. The LSPR creates regions of intense EM field about a nanoparticle surface, known as hot spots, which can produce EFs ranging from 10^5-10^{10}.[16,21–25] The EM mechanism combined with RR is the most common strategy used to achieve single molecule sensitivity with SERS or, more accurately, surface-enhanced resonance Raman spectroscopy

(SERRS). For simplicity, however, we will use SERS throughout the remainder of this dissertation. The EM mechanism in relation to SMSERS will be discussed in Section 1.2 of this introduction.

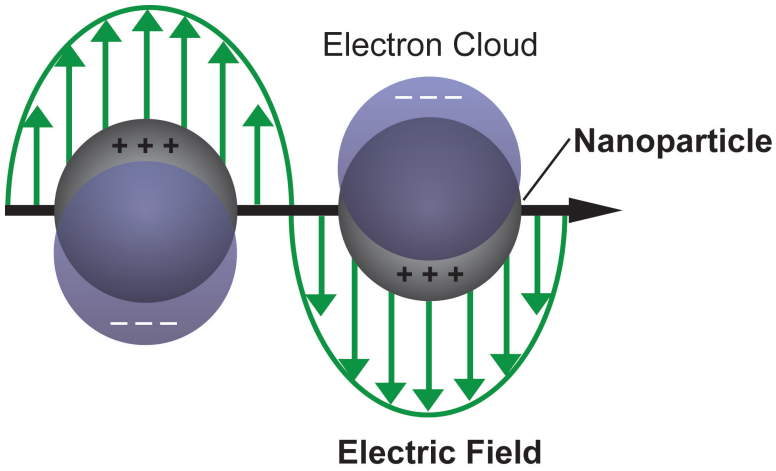

Figure 1.2. Schematic drawing (not to scale) of a plasmonic nanosphere when the electric field component of incident light induces an oscillation of the electron cloud at a frequency defined by the nanosphere size and shape, known as the localized surface plasmon resonance.

The CE mechanism is typically the smallest contributor to the signal enhancement with EFs on the order of 10^1-10^2. The CE is postulated to arise from two main processes:[26–32] enhancements from charge transfer (CT) resonances between the molecule and the SERS substrate,[26,32] and 2) nonresonant changes in the molecular polarizability upon surface binding.[27,28,31] There are two general mechanisms considered for CT processes. The first considers a "transient" charge transfer which is a temporary electron (or hole) transfer between the molecule and the metal surface leading to enhancements in the Raman scattering.[33] The second mechanism considers the formation of intermediate

electronic states resulting when charge is transitioned between the molecule and the metal through the formation of metal-molecule complexes. These new electronic states would promote resonance Raman scattering which is not present in the molecule alone. For example, CT processes can be treated as an excitation from the ground electronic state of the neutral molecule to that of its radical anion.[26,32] Another study by Park et al.[34] found that only a small fraction of the molecules studied experienced a significant (10^1-10^3) contribution of CT to the overall SERS EF, suggesting that there are local "active sites" where the molecules can chemically or electronically interact with the metal.

Enhancements can also result from changes in the polarizability of a molecule upon surface binding. Morton and coworkers conducted time-dependent density functional theory (TDDFT) simulations of meta- and para-substituted pyridines with different functional groups on a silver cluster. By changing the functional groups on pyridine, they were able to modulate the chemical interactions between the pyridine ring and the metal cluster. The TDDFT simulations revealed that altering the energy difference between the highest occupied molecular orbital (HOMO) of the metal and the lowest unoccupied molecular orbital (LUMO) of the analyte lead to increases in enhancement. It also revealed the enhancements did not result from CT to the pyridine ring. They verified this trend by examining substituted benzenethiols, small molecules, and silver clusters of varying size. Their results imply that molecules with significant stabilization of the HOMO-LUMO gaps can experience strong CE, reaching as high as 10^3.[27] Another study experimentally and theoretically investigated the CE of substituted benzenethiols. They found the CE ranged from 10^1-10^2 with more strongly electron donating groups yielding larger enhancements.[31] While there are multiple chemical enhancement processes, the main takeaway for

SMSERS is that the enhancement is generally on the order of 10^1-10^2, but in theoretical calculations has been shown to reach as high as 10^3. Utilization of CE in combination with EM enhancement, may help probe a wider spectrum of molecular systems with SMSERS.

1.1.4. Rhodamine 6G

Rhodamine 6G (R6G) is a highly fluorescent cationic dye shown in Figure 1.3. The molecule contains a xanthene chromophore and phenyl moiety. Ethylamine and methyl substituents are located on the xanthene ring and an ester substituent is located on the phenyl moiety. R6G has a strong visible absorption ($\lambda_{\mathrm{max,ethanol}}$ = 528 nm) and is highly fluorescent with a quantum yield of ∼0.95.[35] When the incidence laser is near the electronic transition of R6G, the signal is increased by a factor of $\sim 10^6$ with a RR cross section of $\sim 2.3 \times 10^{-22}$ cm^2 molecule^{-1}.[18] The RR scattering corresponds to the S_0-S_1 transition, which is an excitation from the HOMO to the LUMO, where both orbitals are localized on the xanthene chromophore and the nitrogen of the ethylamine substituents.[36] In SERS, the strong fluorescence of R6G is quenched due to nonradiative interactions with the metal surface. Fluorescence quenching, excitation on molecular resonance, and the SERS effect (EFs $\sim 10^7$-10^8) allow R6G to be readily detected with SM sensitivity, leading to its popularity as a probe molecule in SMSERS.

Normal Raman scattering and RR scattering spectra of R6G have been calculated using TDDFT.[37–39] The assignments for select bands of R6G are provided in Table 1.1. In addition, an isotopically-edited analog of R6G is commonly used in verifying single molecule detection with SERS. As shown in Figure 1.3, the carboxyphenyl group of R6G is deuterated (R6G-d_4), resulting in a shift of 610 cm^{-1} band to 600 cm^{-1} and an additional

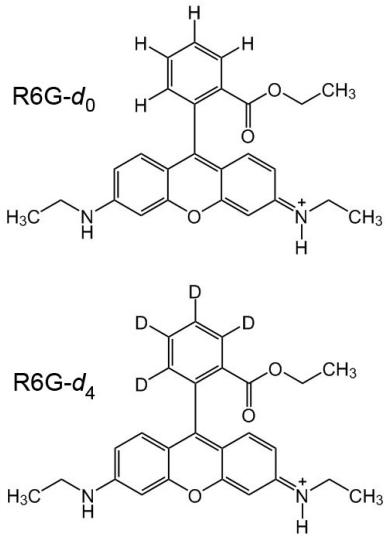

Figure 1.3. Schematic of the Rhodamine 6G isotopologues. The phenyl moiety is isotopically-edited with deuterium.

band at 1335 cm^{-1}.[40] The RR cross section for R6G has also been quantified by Shim and coworkers using stimulated Raman spectroscopy. The cross section for the isotopically sensitive 610 cm^{-1} band is $4.1x10^{-23}$ cm^2 $molecule^{-1}$. Table 1.1 summarizes the cross sections for additional R6G bands.[18]

In a SERS experiment, R6G is adsorbed on a plasmonic metal surface. As such, it is important to consider the absorption spectra of R6G in solution and on a Ag surface. R6G is known to form dimers at high concentrations in solution.[41] The molecule can form J-type (head-to-tail dipole moments) and H-type (parallel dipole moments) dimers. The absorption of H-type dimers is expected to be blue-shifted from the R6G monomer absorption and the absorption of J-type dimers is expected to be red-shifted.[42,43] To examine whether dimers form on a Ag surface Zhao et al., collected absorption spectra at various dosing concentrations (0.6 μM, 6 μM, and 0.1 mM) of R6G on a Ag film followed by deconvolution of the absorption spectra with Guassian curves (dashed lines) as shown

Table 1.1. Assignment and resonance raman cross section of select vibrational bands of R6G.

BP86 [cm^{-1}]	**Experiment [cm^{-1}]**	**Assignment**	**Exp. Cross Section [cm^2 x 10^{-23}]**
610	610	ip XRD	4.1 ± 0.5
616		op XRD	
748		op C-H bend	
754		op C-H bend	
765	771	ip XRD	2.1 ± 0.3
1185	1185	ip XRD, C-H bend, N-H bend	1.4 ± 0.2
1297	1311	ip XRB, N-H bend, CH_2 wag	1.8 ± 0.2
1346	1362	XRS, ip C-H bend	2.6 ± 0.3
1497	1509	XRS, C-N str, C-H bend, N-H bend	2.2 ± 0.3
1551	1574	XRS, ip N-H bend	1.6 ± 0.2
1643	1651	XRS, ip C-H bend	2.0 ± 0.3

The BP86 (Becke-Perdew XC Potential) assignments are from reference [37]. ip: in plane. op: out of plane. XRD: xanthene ring deformations. XRB: xanthene ring breath. XRS: xanthene ring stretch. str: strech. Experimental assignments are from a Ag film over nanosphere (AgFON) substrate incubated in a solution of R6G and collected with λ_{ex} = 532 nm, t_{aq} = 0.1 sec, and P_{ex} = 150 μW. Experimental cross sections are from reference [18].

in Figure 1.4.[36] As the concentrations were increased the authors observed that the major absorption band was red-shifted and the ratio of the two bands at ∼500 nm and ∼540 nm increased (Figure 1.4). The shifting in peak position and increase of the ratio of those two bands, strongly indicate the formation of dimers. The authors assigned the blue-shifted peak of the deconvoluted Gaussian curves to H-type dimers and the red-shifted peak to J-type dimers. These results indicated that both dimers and momomers formed on the Ag surface, even though, in solution the concentration was low enough to avoid dimer formation.[36] In SMSERS, it is important to consider molecular dimer (or larger aggregate)

formation as it can skew the accuracy of SM proofs and the fundamental interpretation of the behaviors of SMs on surfaces, as seen in the shifting of the molecular absorption for R6G dimers.

A recent study by Klingsporn et al. also investigated the adsorbate-surface interactions of a R6G/Ag(111) system using low-temperature (LT) and ultra-high vacuum (UHV) tip-enhanced Raman spectroscopy (TERS) in combination with TDDFT. The LT-TERS spectra showed peak shifts of up to 20 cm^{-1} for multiple modes (e.g., 1132, 1205, 1327, 1350 cm^{-1}) when compared with room-temperature SERS and TERS. As determined from the TDDFT calculations, these modes had greater character from the xanthene ring and/or ethylamine moieties. The authors hypothesize that the moieties in closest proximity the Ag(111) surface will exhibit the greatest perturbations in the observed Raman frequencies. As such, they proposed R6G is oriented edgewise along its xanthene moiety with its ethylamine substituent against the Ag(111) surface.[44]

R6G is ideal for SMSERS. Excitation on resonance with the molecular absorption provides additional signal enhancements of up to 10^6, allowing the molecule to be detected with SM sensitivity. In this section, we have highlighted the properties of R6G as they relate to SERS including peak assignments, RR cross sections, and adsorbate-surface interactions. In order to fully investigate the fundamental mechanisms of SERS, it is necessary to consider the properties of the molecule being probed.

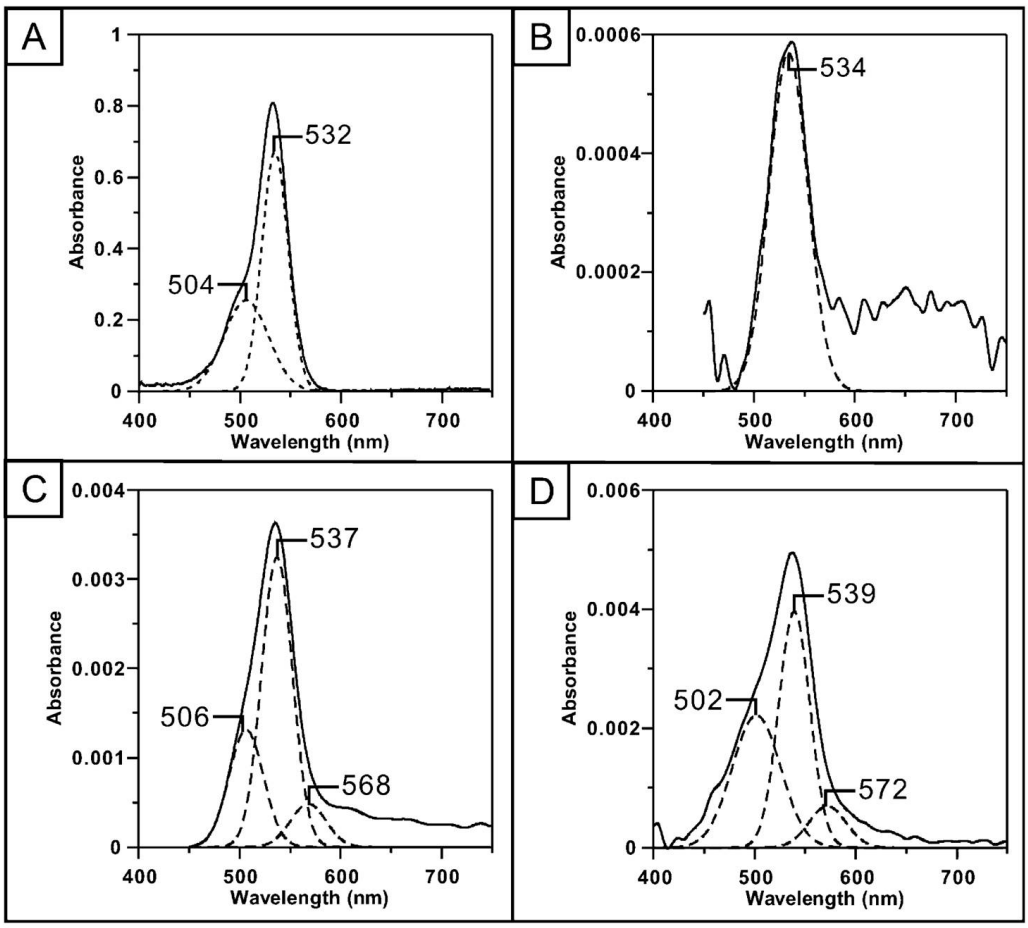

Figure 1.4. A) Absorption spectra of R6G in ethanol, B) 0.6 μM R6G on a Ag surface, C) 6 μM R6G on a Ag surface, D) 0.1 mM R6G on a Ag surface. The dashed lines represent deconvolution of the spectra into Gaussian bands. Adapted with permission from reference [36]. Copyright 2007 American Chemical Society.

1.2. Hot Spots and Plasmonic Nanostructures

After the first demonstrations of SMSERS, early studies set out to understand the specific nanoparticle structures (i.e., hot spots) giving rise to SM detection. These investigations focused on the most commonly used SMSERS substrates: salt-aggregated Ag nanoparticles (e.g., Lee and Meisel Ag colloids).[12,19,22,45] Nie and Emory collected atomic force microscopy (AFM) images of nanoparticles resulting in SMSERS; but, it was unclear whether aggregation of the nanoparticles was necessary or if a single "hot" particle was trapped within an aggregate.[12] A subsequent study correlated SMSERS-active nanoparticles with AFM and found that all of the SERS-active nanoparticles were aggregates,[45] supporting the importance of aggregation to obtain SMSERS detection. AFM correlation, however, provided only limited structural information for elucidating the nature of the SMSERS hot spots.

Camden et al., completed the first comprehensive characterization of hot spots using a correlated experimental and theoretical approach. After locating SMSERS-active nanoparticle aggregates, they conducted high-resolution transmission electron microscopy (HRTEM) to image the aggregate structures, followed by theoretical calculations to model the EM field enhancements of the aforementioned structures.[22] Figure 1.5 shows correlated A) HRTEM, B) SMSERS spectrum, C) and D) discrete dipole approximation (DDA) calculations of the EM field enhancement calculated as $|E_{loc}|^4/|E_0|^4$. The DDA calculations indicate that the dimer structure in A) can provide enhancements of 10^8 at 532 nm excitation in the crevice sites of the nanoparticle dimer junction (i.e., hot spot). These results have been corroborated in multiple studies.[16,22,23]

It is important to remember all of these studies were performed on electronic resonance with the molecule of interest. R6G, for example, has a RR cross section integrated over all observable modes (514 nm excitation) of 2.3 x10^{-22} cm^2 $molecule^{-1}$ compared with a nonresonant molecule at ~10^{-28} to 10^{-30} cm^2 $molecule^{-1}$. Assuming the total enhancement is a multiplication of the RR contributions (up to 10^6 for R6G) and the EM enhancement (10^8), these values are in good agreement with the total EFs of 10^{14}, claimed in early studies.[12,13]

Hot spots from plasmonic structures are not exclusive to nanoparticle junctions. The EM enhancement of individual nanoparticles can be improved with the introduction of sharp features. For example, EFs at the corners of nanobars[25] have been calculated to reach as high as 10^5, the tips of nanopyramids[46] as high as 10^8, and the sharp tips of Au nanostars[47] as high as 10^9-10^{10}. We can, therefore, define hot spots as local areas of intense EM field (EFs = 10^5-10^{10}) occurring at sharp edges, nanoparticle gaps and crevices, or other geometries with a sharp nanoroughness (typically <10 nm). A demonstration of SM sensitivity from individual nanoparticles was performed with SERS substrates fabricated by nanosphere lithography (NSL),[48–52] which will be discussed in Chapter 3. While the understanding of the plasmonic structures that are SMSERS-active has improved, challenges in the rational design and reproducibility of SERS substrates still remain and will be addressed in Section 1.2.3.

1.2.1. Enhancement Factor Distributions

EFs are not uniform across a SERS substrate or even within an individual hot spot. This implies that molecular positioning is an important consideration for fundamental and

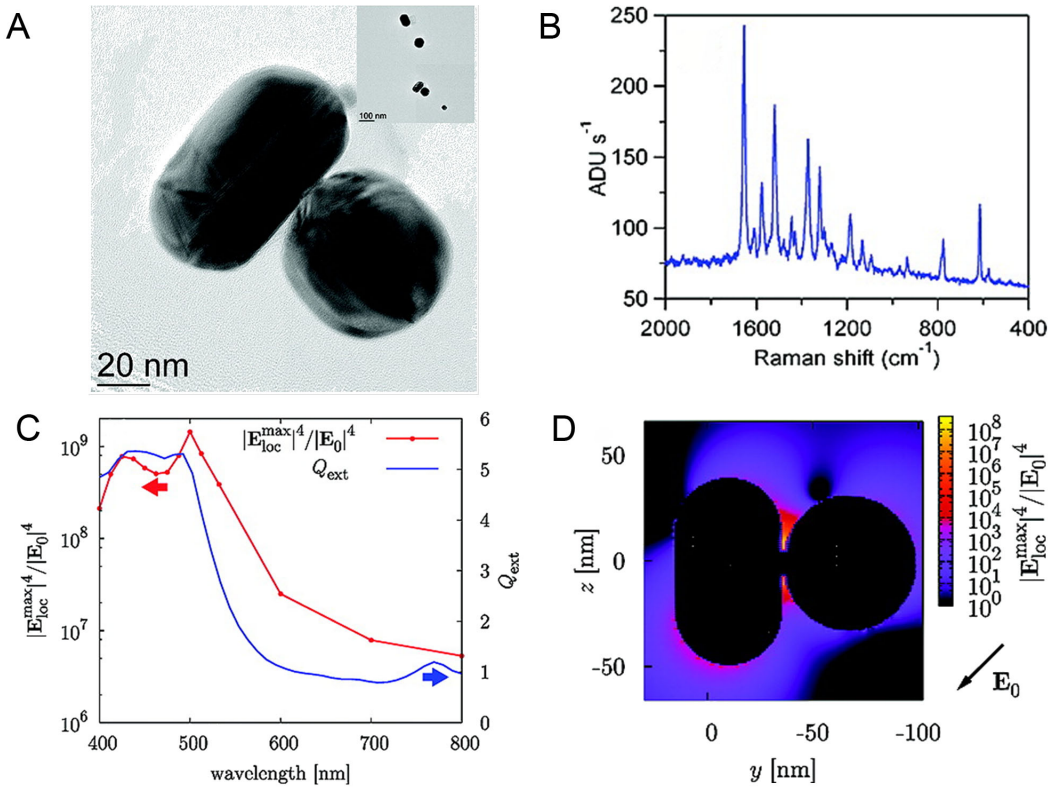

Figure 1.5. A) HRTEM image of a SMSERS-active nanoparticle dimer with correlated SER scattering in B. The optical properties of the nanoparticle aggregated in A obtained from 3D calculations using DDA are provided in C and D. C) Extinction efficiency (blue trace) and maximum SERS enhancement (red trace) for each wavelength calculated as $|E_{loc}|^4/|E_0|^4$. D) Contour plot of the enhancement. The maximum enhancement value is 3.9×10^8 at 532 nm in the crevice sites of the nanoparticle dimer junction. Adapted with permission from reference [22]. Copyright 2008 American Chemical Society.

analytical SERS studies and quantifying EFs. To investigate EF distributions, Fang and coworkers[53] compared the percentage of molecules contributing to the SERS signal with respect to the contributions from the EM enhancement by photochemical hole burning of a AgFON. Essentially, laser pulses were used to photochemically damage molecules adsorbed to the AgFON. Molecules in the highest enhancing regions (i.e., experiencing the highest EFs) are photo-damaged first, resulting in a loss of signal. As the electric fields created by the laser pulses are increased, molecules in increasingly lower enhancing regions will be subsequently photo-damaged, leading to further decreases in the SERS signal. By monitoring the signal loss with respect to the fields created by the laser pulses, they found that ∼25% of the SERS signal is generated by less than 0.01% of the molecules on the substrate surface, which were located in the highest enhancing regions of up to 10^9.[53] This study highlights the importance of molecular location in SMSERS experiments, but it was focused on EF distributions across an entire SERS substrate with ensemble coverage. For SMSERS, a molecule is only detectable when located in a hot spot, thus it is also important to consider the EF distribution within hot spots.

Interrogation of individual hot spots was performed by Le Ru and coworkers for the hot spot created by a nanoparticle gap, theoretically[54] and experimentally.[15] In both studies, they found the EF probability distribution of the nanoparticle gaps followed a long-tail distribution with an average EM enhancement of $\sim 10^7$ and a max as high as $\sim 10^{10}$-10^{11}. EFs as low as $\sim 10^7$-10^8 were found to be sufficient to observe the SER scattering of a single resonant molecule but nonresonant molecules require higher EFs ($\sim 10^9$-10^{11}) as visualized in Figure 1.6.[55,56] These EF values are assuming typical experimental conditions with no additional contributions from chemical enhancements.

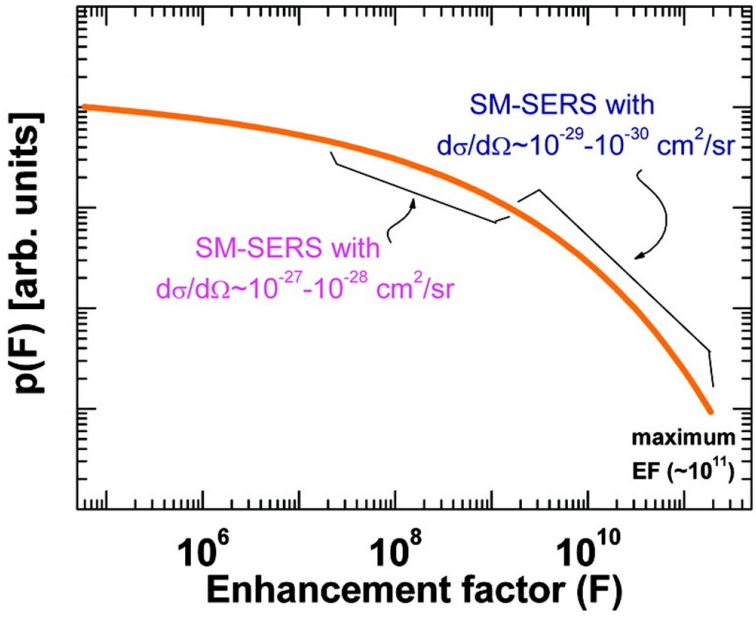

Figure 1.6. Typical long-tail probability distribution for the SERS enhancement factor (p(F)) for a SMSERS-active substrate. Molecules with differential Raman scattering cross sections of $\sim 10^{-27}$ cm^2 sr^{-1} molecule^{-1} are observable as single molecules with EFs $\sim 10^8$ under typical experimental conditions, while nonresonant molecules with differential Raman scattering cross sections of $\sim 10^{-30}$ cm^2 sr^{-1} molecule^{-1} require enhancements of $\sim 10^{11}$, at the high end of the distribution. Adapted with permission from reference [56]. Copyright 2009 American Chemical Society.

An important take-away of these studies is that the calculated EF is critically affected by molecular location with respect to the hot spots of a SERS-active substrate. A difference of only 2 nm in the location of the molecule can result in an order of magnitude change in the EF, which can ultimately dictate whether a molecule is detected or not. It is also difficult to distinguish between multiple molecules experiencing a weaker EF

and a single molecule experiencing a higher EF.[55] As a consequence, molecular binding affinity is an important consideration when using two different analytes to verify SM detection, as we will discuss in more detail in Chapter 2. An additional consequence of the EF distribution across a SERS substrate is the large intensity distributions observed for SM events spanning as high as 3 orders of magnitude for R6G and just over 2 orders of magnitude for CV at 532 nm excitation.[57] The influence of EF variability in a single hot spot can also be visualized in the anti-Stokes-to-Stokes scattering ratios of SMs which is discussed in Section 1.5.3 and Chapter 4. All of these findings imply that molecular binding affinity and positioning of molecules within a hot spot are important considerations for fundamental and analytical SERS studies and quantifying EFs.

1.2.2. Super-Localization of SMSERS Hot Spots

Resolving the location of a single molecule in a hot spot would aid in understanding the coupling between a molecule and the EM fields of the nanoparticle. In SERS, however, obtaining nanometer spatial resolution for molecular location is restricted by the diffraction limit, which is approximately half of the emission wavelength (i.e., ~250 nm with 532 nm excitation). Super-resolution fluorescence microscopy techniques such as photoactivated localization microscopy (PALM), stochastic optical reconstruction microscopy (STORM), and stimulated emission depletion (STED) microscopy have demonstrated sub-20 nm resolution of fluorescent molecules in biologically relevant systems overcoming the diffraction limit.[58,59]

In 2010 to overcome this limitation with SERS, Stranahan and Willets combined the principles of super-resolution fluorescence microscopy with SERS, coined super-localization

SERS.[60,61] They successfully imaged the spatial profile of R6G molecules on single Ag colloidal nanoparticle aggregates with sub-15 nm spatial precision.[62] In super-localization SERS, there are two emission sources in a diffraction limited spot: 1) the SER-signal and 2) the nanoparticle background. By exploiting the on-off blinking of SMSERS signals they were able to fit the location of both emitters. The locations were determined by fitting the R6G SERS signal and the nanoparticle background to a two-dimensional Gaussian point spread function (PSF), with the peak of the fit defined as the centroid position. The authors found that the spread of centroid positions on a single nanoparticle aggregate (20-100 nm) was much greater than that of the expected nanoparticle aggregate hot spot junction size (1-10 nm). Subsequent work by Weber and Willets investigated this observation by combining super-localization SERS with correlated scanning electron microscopy (SEM) nanoparticle structure measurements.[60] The authors reported an excellent agreement between the location of the hot spots for Ag nanoparticle aggregates and the SERS centroid positions. Figure 1.7 shows the centroid positions for the R6G SERS signal overlaid on the SEM image of the corresponding nanoparticle aggregate. Interestingly, the spatial origin of the SERS centroids suggests that the molecule is confined to the surface of only one of the nanoparticles within the aggregate. From these studies, they concluded that the large spread of centroid positions was caused by the diffusion of a R6G molecule between multiple hot spots, greatly extending the SMSERS-active area on the nanoparticle aggregate.

Using an isotopologue approach (discussed in Section 1.3) can further illuminate the behavior of distinct molecules on a nanoparticle surface. Weber and Willets used this approach to verify that the shifting centroid positions are due to the movement of R6G

molecules on the surface and not to molecular reorientation or random nanoparticle emission by demonstrating that a nanoparticle aggregate with both R6G isotopologues (R6G-d_0 and R6G-d_4, Figure 1.3) had spatially distinct centroid positions.[63] Using super-localization SERS to watch the centroid positions of distinct molecules on a nanoparticle aggregate with sub-15 nm spatial precision lends itself to exploring the nanoscale reactivity of nanoparticles, such as the site-specificity of electrochemical,[64,65] catalytic, or photochemical reactions.

1.2.3. Rational Design of SMSERS Substrates

The design of new substrates for SMSERS has focused primarily on improving reproducibility of nanoparticle size, shape, degree of aggregation, increasing hot spot density, and positioning molecules with control into a hot spot. Lithographically-prepared substrates such as nanoantennas[67,68] (Figure 1.8A) and nanopyramid arrays[52] (Figure 1.8B) are one avenue to improve substrate reproducibility. Nanoantennas have been reported to have EFs of up to $\sim 10^{13}$ due to the combination of an optimized local EM field enhancement (10^{11}) and antenna directionality (10^2),[67,68] with excellent control over hot spot positioning. However, nanoantenna fabrication is complicated and costly. The multi-step, top-down fabrication requires electron beam lithography and alignment with nanoscale precision. On the other hand, NSL used to fabricate arrays of nanopyramids is a facile, cost-effective, and easily tunable approach to prepare nanoparticles.[48–51,69,70] However, the nanoparticle arrays are subject to packing defects due to small variations in nanosphere size. For NSL, nanospheres are dried into a close-packed monolayer on glass coverslips,

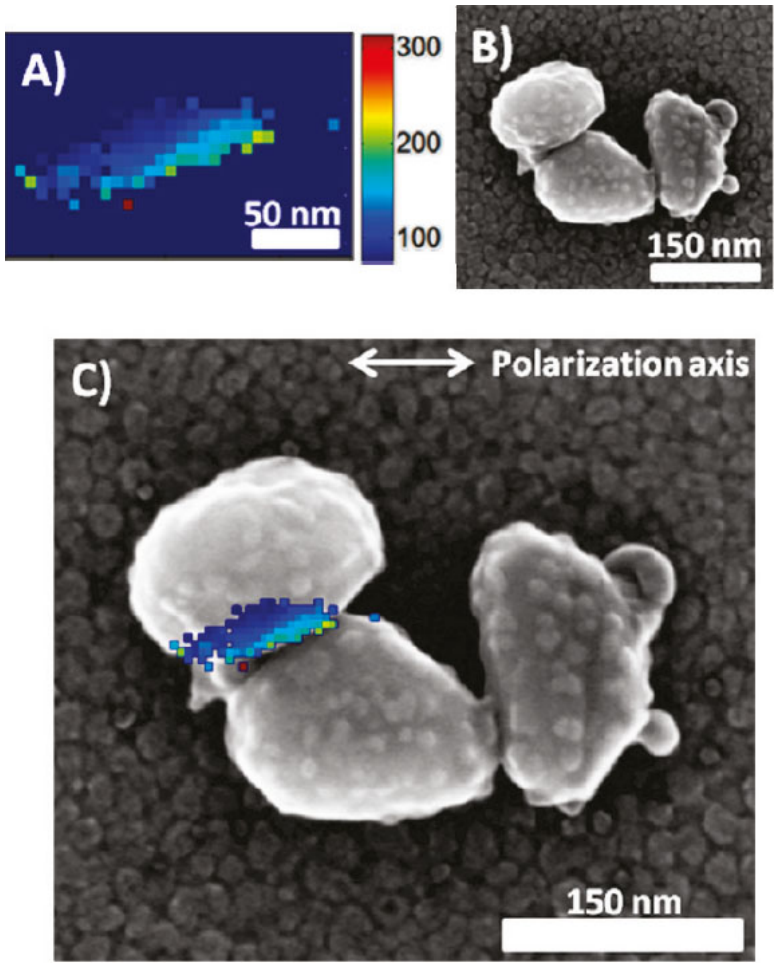

Figure 1.7. A) R6G SERS signal intensity spatial map and B) SEM image of the Ag nanoparticle trimer from which the data in A was collected. C) Overlay of A and B. Adapted with permission from reference [66]. Copyright 2011 American Chemical Society.

onto which a layer of metal is deposited. Removal of the nanospheres leaves behind an array of nanopyramids created in the interstitial sites of the close-packed monolayer (Figure 1.8B and Figure 3.2). Outside of NSL and nanoantenna fabrication, other efforts have focused on improving the reproducibility of chemically-synthesized Ag nanoparticles. One

strategy is to use DNA self-assembly and other linking molecules[71] to form controlled nanoparticle dimers or larger aggregates.[72–74]

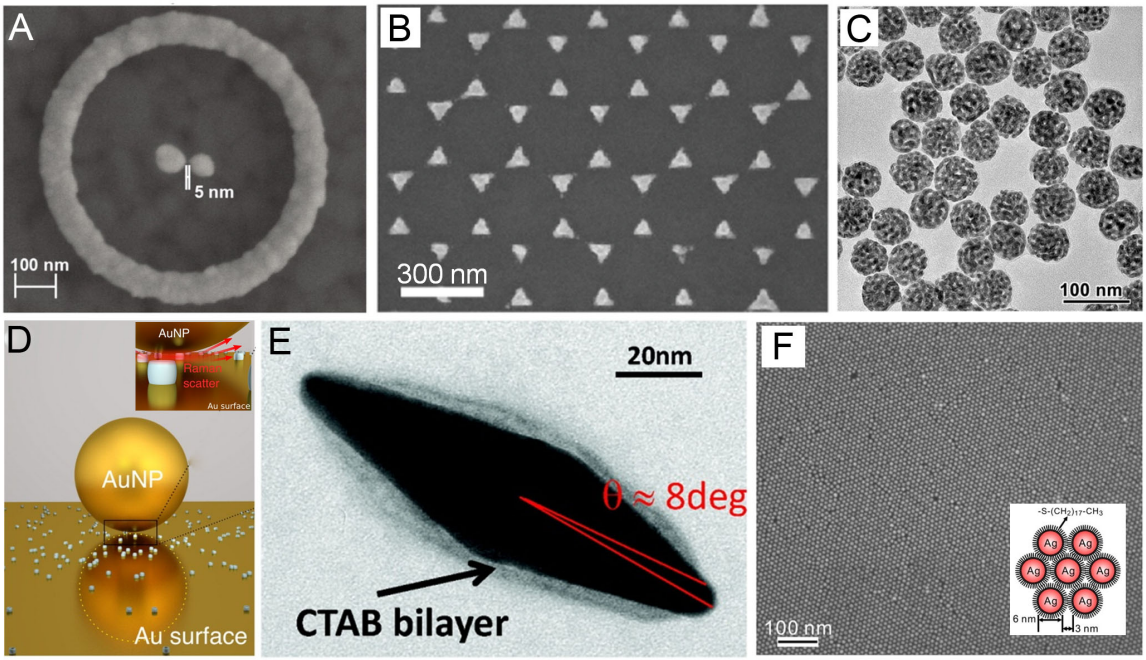

Figure 1.8. A) Lithographically-prepared nanoantennas with directional Raman scattering,[68] B) tunable nanopyramid array fabricated by nanosphere lithography,[52] C) porous Au-Ag nanospheres with increased hot spot density due to the introduction of nanoroughness,[75] D) schematic of a GM-SERS experiment with Au nanoparticles located over a Au film,[76] E) TEM image of CTAB-stabilized bipyramids,[77] and F) close-packed monolayer of Ag nanospheres on a quartz substrate with an image area of 1 × 0.7 μm^2.[78] The inset shows that the interparticle gap is regulated by the thiolate chain length. Adapted with permission from references [52, 68, 75–78]. Copyright 2011, 2013, 2015, and 2016 American Chemical Society.

An alternative strategy to improve reproducibility is gap-mode SERS (GM-SERS), a simple nanoparticle-based analog to TERS. In GM-SERS, the analyte of interest is adsorbed onto a smooth metallic thin film, upon which nanoparticles are deposited. The molecules of interest are consequently located in the film-nanoparticle gap, as shown in Figure 1.8D.[76] The benefit of GM-SERS is that it does not require the random aggregation of nanoparticles, which improves substrate reproducibility, assuming the nanoparticles are monodisperse in size. An additional advantage of GM-SERS is the possibility to observe site-specific chemistry on thin film surfaces that are not inherently plasmonic.[79–81] GM-SERS has recently been used to study single molecule host-guest interactions, which we discuss in detail in Chapter 6 Section 6.1.4.

Increasing the hot spot density of SERS substrates is also an important parameter in substrate design. For aggregated Ag colloids, typically only 1% of the nanoparticles are SMSERS-active,[22] making the collection of statistics in SMSERS studies challenging. Attempts to improve hot spot density include fabricating close-packed monolayers of Ag[78] (Figure 1.8F) and Au[82] nanoparticles, templated Ag nanocube arrays,[83] and synthesizing porous Au-Ag nanospheres[75] (Figure 1.8C). Porous Au-Ag nanoparticles, for example, create a high density of hot spots across the nanoparticle surface through the introduction of nanoscale features. Single porous particles were reported to have EFs on the order of $\sim 10^7$ compared with "smooth" single, spherical nanoparticles at $\sim 10^4$.[24,75,84,85]

Another major challenge is controlling the positioning of molecules within the plasmonic hot spot. One strategy to address this challenge was the fabrication of cetyltrimethylammonium bromide (CTAB)-coated bipyramids (Figure 1.8E).[77] The CTAB bilayer prevents the adsorption of positively charged dyes (crystal violet in this study) to the

nanoparticle surface except on the tip where CTAB was not present. In principle, this design would only allow the binding of molecules to the regions of highest enhancement.[77] The authors observed that every crystal violet molecule experienced an EF close to the maximum value expected for the bipyramid tips, suggesting success of this strategy. This bilayer approach, however, is not necessarily adaptable to gap-containing nanoparticles and is highly depending on the analyte's adsorption affinity. More recently, a plasmonic substrate was designed to reversibly trap single molecules in hot spots.[86] The substrate was fabricated through the electrostatic self-assembly of Au nanoparticles onto a Au and silica-coated silicon platform between which the molecule would be located. The hot spots were isolated by using a thermoresponsive polymer which acts as a gate for trapping the molecules through the heating and cooling of the substrate.

Over the past several years, great strides have been made toward improving SERS substrates. The majority of SMSERS experiments, however, still rely on the random aggregation of Ag nanoparticles. As the field moves forward, utilizing more reproducible nanoparticle substrates will allow for the systematic improvement of our fundamental understanding of SERS mechanisms and provide more reliable means of interpreting chemistry at the single molecule level. In addition, the ability to increase hot spot density while simultaneously controlling the positioning of molecules within those hot spots will greatly improve the collection of statistics for SMSERS.

1.3. Verification of SMSERS

Verification of SM detection is essential for SMSERS to be a robust analytical technique. In this section, we will highlight the complications of proving SM detection with

SERS including a discussion on the early strategies and their faults. Then, we will cover the most commonly accepted two-analyte methodology. Finally, we will conclude with a discussion on the role of sample preparation in reliable SMSERS.

1.3.1. Early Strategies

The first SMSERS studies adapted proof methodologies from SM fluorescence. SM detection in fluorescence spectroscopy is unequivocally proven through the observation of photon antibunching, which is based on the phenomenon that single molecules cannot emit two fluorescence photons simultaneously.[87] However, this strategy is not possible for SMSERS because the lifetime of Raman scattering is short ($<10^{-14}$ sec) relative to fluorescence (10^{-9} sec).[88] Another strategy to confirm SM detection, also common in SM fluorescence, is to sufficiently dilute the target molecule concentration to achieve, on average, one or fewer molecules within the probe volume. While this is an effective strategy for fluorescence spectroscopy, the addition of metallic nanoparticles complicates the process. Unequivocally proving SMSERS detection using only ultra-low concentrations would require knowledge of the contributions from molecular binding affinity and diffusion, molecule and nanoparticle concentrations, the position of the molecule relative to plasmonic hot spots, and the number of nanoparticle hot spots within the probe volume. As a consequence, ultra-low concentrations as a justification for SMSERS are not adequate. This is further highlighted by Darby et al., where the authors found that the dilution procedure used to prepare samples could artificially create the appearance of SMSERS due to the competition between molecular diffusion and adsorption to the nanoparticles.[89] Instead,

most strategies have employed ultra-low concentrations with additional protocols to prove SMSERS ranging from the observation of fluctuations to a statistical analysis.

In 1997, Nie and Emory noted that the Raman signals would suddenly disappear or change during a period of continuous illumination.[12] This blinking behavior, or the on/off fluctuation of the SERS signal was initially viewed as validation of SM detection.[90,91] Andersen et al., however, demonstrated that Ag colloids exhibit blinking that is independent of the molecule being probed and that this phenomenon was observed in both the presence and absence of a probe molecule.[92] A second study observed large spectral fluctuations for an amorphous carbon layer deposited on SERS substrates.[93] Furthermore, blinking has been observed at surface coverage above the SM level.[40,93,94] While fluctuations are a characteristic behavior of single molecules, they do not exclude the possibility of multiple molecules or other phenomena causing the fluctuations.[40,92–94] Therefore, the use of a fluctuation argument is inadequate evidence for SM detection. Another indirect strategy to verify SM detection is the observation of a polarization-dependent SER signal.[12] This, however, requires the ability to deconvolute the polarization-dependence of the plasmonic structures from that of the SER scattering of the analyte.

Others have provided evidence for SM detection using a combination of ultra-low analyte concentration and a statistical analysis of the SERS intensities.[13] At ultra-low concentrations the number of molecules that bind to the nanoparticle surface should follow a Poisson distribution. This analysis assumed that the difference in the SER intensity between events could be attributed to 0, 1, 2, or 3 molecules being probed. However, it was demonstrated that a valid SMSERS Poisson distribution requires the variation in intensity between SERS events to be less than a factor of 2 and a minimum 10,000 sample

events would need to be recorded,[54,95] a highly impractical feat for SMSERS. Furthermore, the variation in intensity between SM events has been shown to span as high as 3 orders of magnitude, considerably greater than a factor of 2.[40,54,57] As a consequence, the existence a Poisson distribution of SERS intensities alone is not a valid proof of SM detection.

1.3.2. Current Methodologies

In 2006, Le Ru et al. introduced a bianalyte approach for proving SM detection. This approach involves dosing the SERS-active substrate with two analytes at equimolar concentrations and determining whether the SERS events contain a single analyte or a combination of both analytes.[96] While the bianalyte approach is a useful means of proving SMSERS detection, there can be experimental complications such as the analytes having different Raman scattering cross sections or affinities to the SERS-active substrate.[57] An alternative of the bianalyte approach is the isotopologue approach. The isotopologue approach uses a molecule and its isotopically-edited analog as bianalyte pairs (i.e., isotopologues).[19,40] Example isotopologue pairs used in SMSERS include R6G-d_0/d_4,[40] CV-d_0/d_{12},[19] and porphycene-d_0/d_{12}.[97] This approach is advantageous because isotopologues inherently have identical surface binding affinities, extinction coefficients for molecular electronic resonances, and Raman scattering cross sections, while bianalyte partners will not have identical values for these properties. Furthermore, the isotopic-editing results in frequency shifts of the vibrational modes. For example, Figure 1.9 shows the SERS spectrum of R6G-d_0 and R6G-d_4. Upon isotopic-editing of the phenyl moiety the peak at 611 cm^{-1} shifts to 601 cm^{-1} with an additional peak appearing at 1335 cm^{-1}.[40] These peak shifts allow identification of the R6G isotopologue(s) present in the SERS spectra.

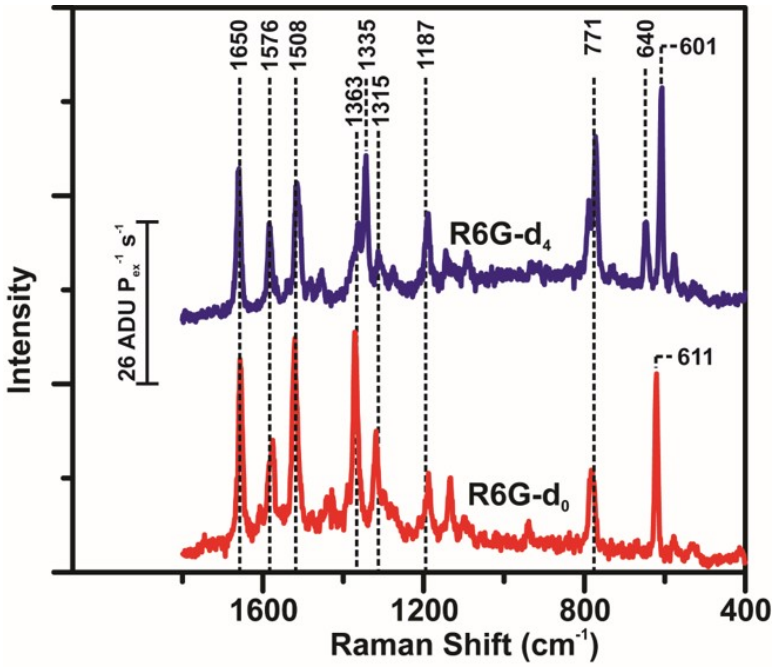

Figure 1.9. Spectra of R6G isotopologues collected with λ_{ex} = 532 nm, t_{aq} = 150 sec, and P_{ex} = 15,000 W/cm^2. Upon isotopic-editing the peak at 611 cm^{-1} shifts to 601 cm^{-1} with an additional peak appearing at 1335 cm^{-1}. Adapted with permission from reference [40]. Copyright 2007 American Chemical Society.

The ratio of counts of individual analyte events to events with both analytes is used to verify SM detection. This ratio can be described using a Poisson-binomial distribution.[40,57] At sufficiently low coverage, the probability that a molecule is bound to the nanoparticle aggregate follows a Poisson distribution. Once bound, the probability that the molecule detected is either analyte 1 or analyte 2 follows a binomial distribution. Therefore, the overall probability that analyte 1 and/or analyte 2 will be detected in a given spectrum

is the product of both distributions:

$$P(\alpha, n_1, n_2) = \frac{e^{-\alpha}}{n_1! n_2!}(\frac{\alpha}{2})^{(n_1+n_2)} \tag{1.2}$$

where α is the average number of molecules per spectrum, and n_1 and n_2 are the number of analyte 1 and analyte 2 molecules detected in the SER spectrum, respectively. P is the probability that n_1 analyte 1 and n_2 analyte 2 molecules at α-coverage will be detected for a given spectrum, assuming a 50:50 probability that either analyte 1 or analyte 2 as the identity of a given molecule. For $\alpha = 1$, 76% of the spectra must have individual analyte character to verify SMSERS. The influence of different detection probabilities for bianalyte pairs on the proof of SM detection will be covered in Chapter 2. Appropriate implementation of SM proofs will greatly advance the use of SMSERS as an analytical technique.

1.3.3. Reliable Sample Preparation

Along with rigorous statistical analysis, proper sample preparation is essential to ensure consistent coverage of molecules on the SERS substrate. A typical SMSERS experiment involves incubating resonant molecules at ultralow concentrations (typically nM or pM) with Ag colloidal nanoparticles. Salt solutions such as NaCl or KCl are used to aggregate the colloids, creating hot spots with EFs on the order of $\sim 10^7$-10^8.[12,13,19,40,57,89]

Darby et al., investigated the effect of sample preparation on SMSERS experiments for dye/colloidal mixtures.[89] Figure 1.10 demonstrates two tested dilution procedures: 1) large dilution factors (LDF) and 2) half-half dilution (HHD). Due to the competition between molecular diffusion and adsorption, LDFs lead to uneven nanoparticle coverage

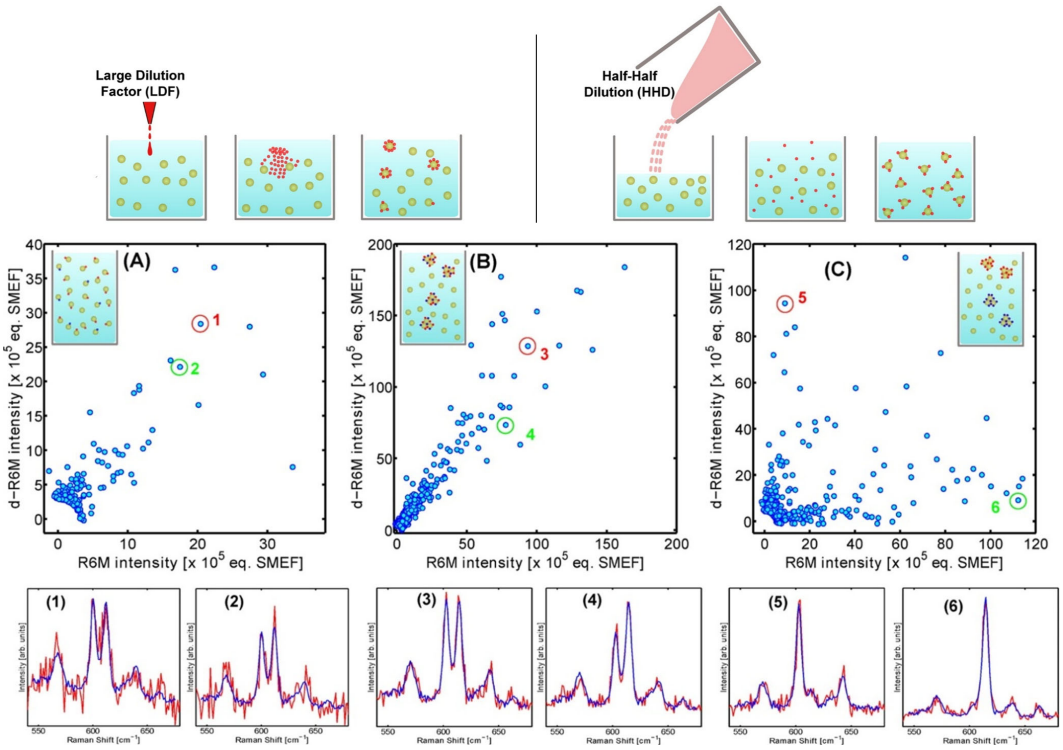

Figure 1.10. Top) Visual representation of two dilution methods for preparing SMSERS samples. Bottom) The effect of different sample dilution procedures on SMSERS. Scatter plots of the intensity for the isotopic-sensitive R6G mode (∼600 and 610 cm^{-1}) are shown. The samples were prepared in A) by premixing the two dyes with HHD, in B) by premixing the dyes with a 100x LDF, and in C) by adding the dyes individually with a 100x LDF. The inset shows a schematic of the expected molecular coverage. Below the scatter plots are representative SERS spectra indicated by the number 1-6 circled. Adapted with permission from reference [89]. Copyright 2014 American Chemical Society.

and the appearance of SM detection when it is not actually achieved. Premixing the dyes and using HHDs is recommended to obtain uniform coverage. Figure 1.10A shows experimental results from samples prepared using HHD. Figure 1.10B shows samples prepared with premixing of the dyes and a 100x dilution factor. Figure 1.10C shows samples in which the dyes were added to the colloid mixture sequentially with a 100x dilution factor. The overall SERS signal intensities in A are weaker than B and C, suggesting more uniform coverage as indicated in the schematic representations. Most strikingly, the majority of events in Figure 1.10C show SERS spectra with strong signals of only one isotopologue, when the majority of spectra should have had both analytes. This work illustrates that proper dilution is crucial for obtaining appropriate molecular coverage in SMSERS experiments.

Other practical considerations when preparing SMSERS samples are the choice of bi-analyte pair for proving SM detection,[57] analyte concentration, type of SERS substrate, the method of applying the analytes to the SERS substrate (e.g., solution-phase incubation,[12,13,40,89] spin-coating,[57] or Langmuir-Blodgett film deposition),[98,99] and laser power to limit photodegradation.[55] For example, SMSERS spectra of R6G have been observed down to 5 nW excitation.[100] Since a simple dilution procedure can significantly influence molecular coverage and EF distributions exist across a SERS substrate (discussed in Section 1.2.1), all studies should clearly define their experimental procedures to ensure accurate interpretation of results and reproducibility.

1.4. Nonresonant SMSERS

Resonant molecules are ideal for SMSERS because they provide RR enhancements as high as 10^6.[18–20] Conversely, SMSERS of nonresonant molecules with cross sections $\sim 10^{-29}$ to 10^{-30} cm^2 sr^{-1} $molecule^{-1}$ require SERS substrates to support EFs on the order of 10^9-10^{11}. Nonresonant SMSERS has been claimed for 1,2-bis-(4-pyridyl)-ethylene (BPE) with a benzotriazole dye as the bianalyte partner to verify SM detection.[56] For BPE, EFs of $\sim 10^9$ were necessary to achieve SM detection. In this study, the authors also attempted SM detection of adenine, but it was only possible in the rare cases when EFs reached as high as 10^{11}.[56] This study demonstrated that SM detection of nonresonant molecules is possible; however, the rarity of observing a SM event due to the high EF requirements makes these experiments very challenging. Therefore, in order to expand the scope of molecules that can be studied with SMSERS, it is necessary to gain additional enhancement from avenues besides molecular resonance.

One strategy is to use highly enhancing SERS substrates with EFs of 10^9 or higher, such as the nanoantennas discussed in Section 1.2.3. Wang and coworkers claimed the nanoantennas[67,68] had EFs as high as $\sim 10^{13}$, which would readily allow the detection of single nonresonant molecules. Another strategy is to take advantage of the CE mechanism in addition to the EM mechanism. The CE mechanism in SERS is generally accepted to contribute enhancements of 10^1-10^2 (Section 1.1.3). Theoretical calculations have also found that by tailoring the molecule with different functional groups, thereby altering the energy difference between the HOMO of the metal and the LUMO of the analyte,[27] the chemical enhancement can surpass 10^3. Utilization of CE in combination with EM enhancement, may help probe a wider spectrum of molecular systems with SMSERS.

1.5. Signal Fluctuations and Heterogeneity in SMSERS

One advantage of studies at the SM limit is they provide a viable route for investigating principle mechanisms of the SERS enhancement, the fundamental properties of spectroscopic phenomena, and single molecular properties otherwise obscured by ensemble averaging. We will highlight several recent studies focused on improving our fundamental understanding of signal fluctuations such as blinking and spectral wandering and the heterogeneity of SMSERS events.

1.5.1. Blinking

Signal fluctuations were originally used to validate SM detection. Despite the fact that this idea was later disproven,[40,92–94] the origin of signal fluctuations is still a highly debated topic in the SERS community. Blinking is described as the on-off cycling of the SMSERS signal and can last from ms to minutes.[13,90,101–104] The role of illumination power,[101] electrolyte concentration[101] temperature,[105,106] EM mechanism,[107,108] and excitation wavelength[94,103] have all been explored in relation to blinking behavior.

Itoh and coworkers conducted a quantitative analysis of blinking in SERS and surface-enhanced fluorescence (SEF) using Ag nanoparticle dimers functionalized with R6G.[108] They observed that the SERS and SEF signals varied from dimer to dimer but could be divided into three main categories: 1) stable, 2) fluctuating, and 3) intermittent. Stable refers to SERS signal with minimal changes in intensity throughout the entire temporal trajectory. Fluctuating refers to SERS signal that blinks continuously and intermittent refers to SERS signal that switches between periods of being stable and blinking. Correlated SERS, SEF, plasmon resonance spectra, and temporal trajectories

of the SERS and SEF were collected. The authors used intense NIR laser pulses to induce fluctuations in an otherwise stable signal. These laser pulses induced a 50 nm blue shift in the LSPR, which coincided with the onset of the unstable SERS signal. Based on these results and their reproduction of the SERS and SEF signals using the EM mechanism, (see reference [108] for more details on their quantitative analysis), they proposed two insights into blinking behavior. First, an unstable adsorption of R6G to Ag nanoparticles causes instability in the SERS and SEF signals. Unstable adsorption can alter the distance between the molecule and the nanoparticle surface overtime, leading to changes in the EF the molecule experiences and, therefore, the signal. Second, changes to the plasmon resonance of the Ag nanoparticles can induce blinking as it also alters the EF. Due to these insights, they suggest that the underlying cause of blinking can be attributed to photo-induced effects such as thermal heating of nanoparticle hot spots leading to plasmon resonance shifts, diffusion of the molecule around a hot spot, and/or photo-bleaching.

Kitahama and coworkers analyzed the bright (on) and dark (off) states of SERS blinking for thiacyanine using a power law analysis.[103,104,109] Power law statistics have been used to analyze long-range ordered non-exponential behavior in quantum dots (QD). The power law for fluorescence blinking of a single QD can be explained by a distribution in the passage of time required for a random walker to return to its starting point, which is approximated using a one-dimensional random walk model. Kitahama et al. postulated that blinking statistics in SERS will be similar due to the random molecular walk of an adsorbed molecule on the nanoparticle surface. Indeed, they observed that the power law reproduced the probability distribution of the occurrence of the bright and dark states over time.

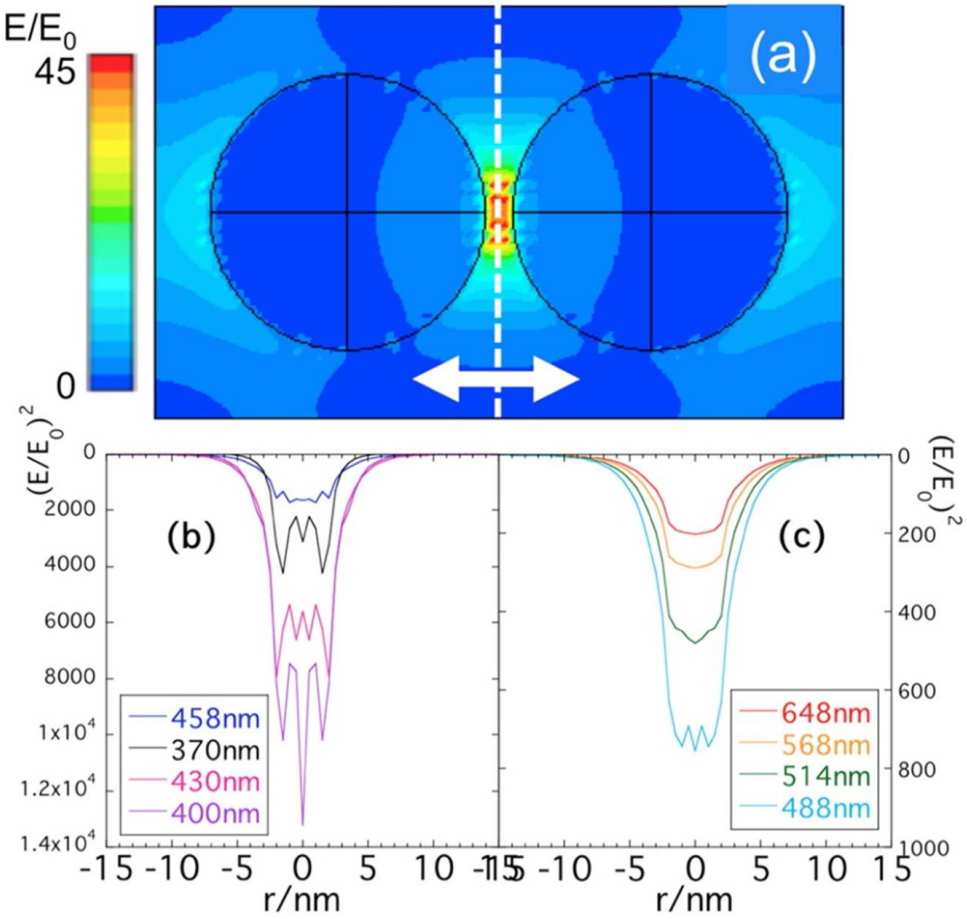

Figure 1.11. A) Calculated spatial distribution of the EF for a 20 nm diameter Ag dimer with a 2 nm gap. Excitation with horizontal polarization at 458 nm is shown. Calculated intensities in B and C show the optical trapping potential wells along the dashed vertical line in the nanoparticle gap. Adapted with permission from reference [104]. Copyright 2015 American Chemical Society.

Next, the authors monitored the power law exponent as they swept the excitation wavelength across the nanoparticle aggregate LSPR. When excited at the LSPR wavelength of the nanoparticle aggregate or with high laser power, the power law exponent

of the bright and dark blinking events approached -1.5, similar to what is expected for QD blinking. When excited off the LSPR wavelength and with lower excitation laser powers, the power law deviated from -1.5. They propose the high EM fields created when excited at the LSPR wavelength restrain the molecule by a surface-plasmon-enhanced optical trapping potential well around the nanoparticle junction. Subsequent studies by Kitahama and coworkers observed that a truncated power law reproduced the probability distribution of dark SERS events versus their duration time.[103,104] They proposed the truncation of the power law indicates a high energy barrier must be overcome for the molecule to undergo a transition from the non-emissive state to emissive state and that fast random molecular walking (i.e., surface diffusion into the nanoparticle junction) helps to overcome this energy barrier. Figure 1.11A shows a near field image of the EM field around a 2 nm Ag nanoparticle gap calculated by FDTD. Figure 1.11B-C show the periodic optical trapping potential well due to the EM field at various excitation wavelengths. The energy barrier is suggested to originate from the coupling of multi-polar surface plasmon resonances around the nanoparticle junction. This research highlights the importance of considering both the bright and dark SERS states to fully explain SERS blinking behavior.[104]

Additional proposed mechanisms for blinking include: 1) thermal diffusion in-and-out of the hot spot,[90,94,106] 2) thermally-stimulated molecular reorientation and chemical processes,[105] 3) photoionization due to charge transfer states,[101] and 4) metastable and non-emissive states of the molecule.[110] Based on the current studies, the overall consensus for the origin of blinking is thermally-stimulated movement of the molecules on the

nanoparticle surface, likely accompanied by photo-induced effects such as electron transfer or other chemical processes.

1.5.2. Spectral Wandering

Spectral wandering is the shift in frequency or spectral position for a particular vibrational mode. The frequency of the isotopically sensitive phenyl bands at 610 and 600 cm^{-1} for SM events of R6G-d_0 and R6G-d_4, respectively, have been observed in multiple studies, showing the peak centers can shift ± 5 cm^{-1} from event-to-event.[40,57,111] Similarly, spectral wandering was explored by Etchegoin et al., for Nile Blue (NB) and Rhodamine 800 (R800) at 77 K.[112] Using a high-resolution grating, the authors were able to observe inhomogeneous broadening of the 590 cm^{-1} and 2226 cm^{-1} modes of NB and R800, respectively. Figure 1.12 shows the individual SM events and average spectra for A) NB and B) R800. Multiple SM spectra of the $\sim$590 cm^{-1} mode for NB are shown to fit within the average of 7500 spectra collected, signifying that the average SERS signal is the average of a population of many molecules. As expected, the SM peaks appear within a range of $\sim$584-596 cm^{-1} with the majority of events centered at 590 cm^{-1}. The same trend is shown for the $\sim$2226 cm^{-1} cyano bond (C$\equiv$N) mode of R800. In a subsequent study, it was shown that the peak shifts for the $\sim$2226 cm^{-1} mode can also be attributed to natural isotopic substitutions from ^{12}C to ^{13}C and ^{14}N to ^{15}N.[113] These studies show that small frequency shifts observed in SMSERS spectra are generally attributed to different local environments and isotopic effects.[113] Additional studies have also observed homogenous broadening[114] and overtone and combinations bands[115] with SMSERS.

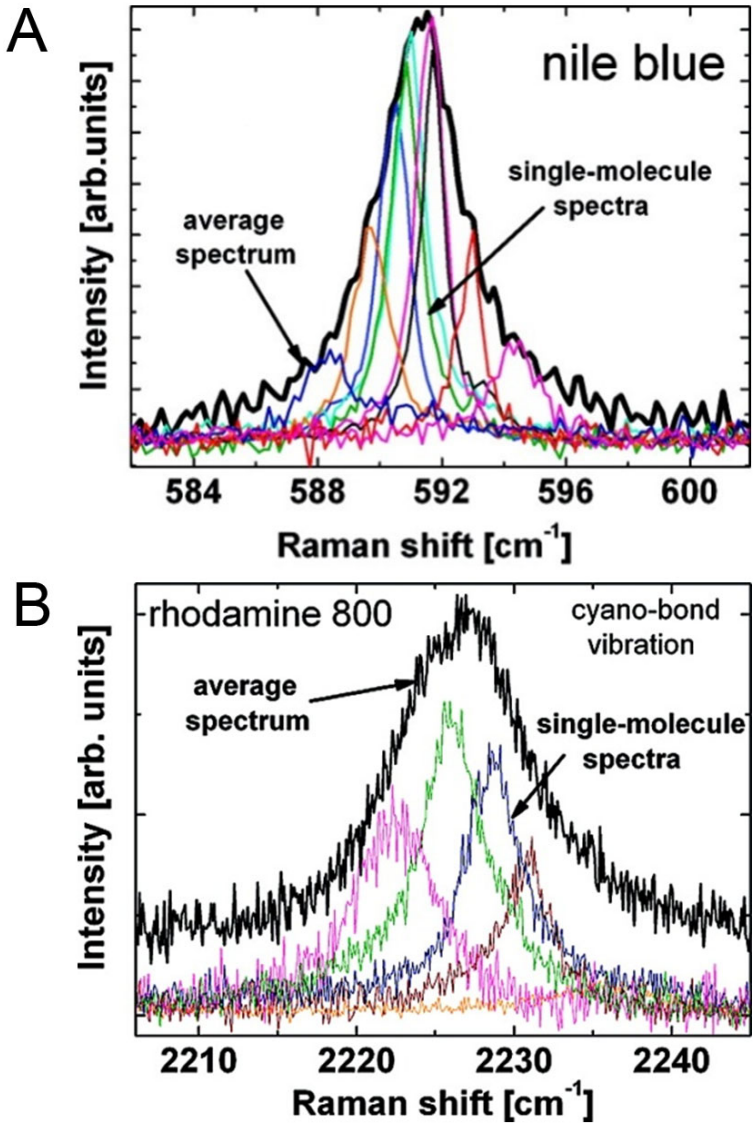

Figure 1.12. Inhomogeneous broadening observed for A) the ∼590 cm^{-1} peak of NB and B) the ∼2226 cm^{-1} mode of R800. The spectra were collected a 77 K with 633 nm excitation and a high-resolution 2400 lines/mm grating. Individual single molecule events are shown to fall within the average signal of over 7500 spectra (black trace) for both NB and R800. Adapted with permission from reference [112]. Copyright 2010 American Chemical Society.

1.5.3. Distribution in the Anti-Stokes-to-Stokes Scattering Ratio

Broad distributions in the anti-Stokes-to-Stokes scattering ratio (ρ) have been observed in SMSERS studies.[116–119] Anti-Stokes scattering depends on the population of the excited vibrational states. Increases in the anti-Stokes scattering intensity (i.e., increases in ρ) can be attributed to multiple factors including vibrational pumping, heating, and resonance effects that unevenly enhance the Stokes and anti-Stokes scattering. Several studies have focused on understanding how these effects lead to fluctuations in the anti-Stokes scattering intensity which cannot be accounted for by thermal population of the excited vibrational states alone.[116–120]

Vibrational pumping is the increase of the population of excited states through Stokes scattering.[120] The first conclusive demonstration of vibrational pumping in SERS was done by Maher et al., who used temperature scans to separate out the contributions of resonance effects and heating from those of vibrational pumping.[120] Building off this study, Galloway and coworkers, used low temperatures (77 K) and high power densities (4.48 x10^8 W m^{-2}) to verify the effect of vibrational pumping on ρ.[117] They showed that even though both NB and CV Stokes signals were present for many events, the anti-Stokes scattering would often be observed for only NB or only CV in the same, simultaneously collected spectrum. This result suggests that molecules can experience unequal contributions from vibrational pumping. While vibrational pumping is an important consideration at cryogenic temperatures, it is not a main contributor to ρ at room temperature, which is dominated by thermal population or resonance effects.

Two subsequent studies investigated the role of local field enhancements and plasmonic heating on ρ for SMs. Pereita dos Santos and coworkers studied ρ for brilliant green (BG)

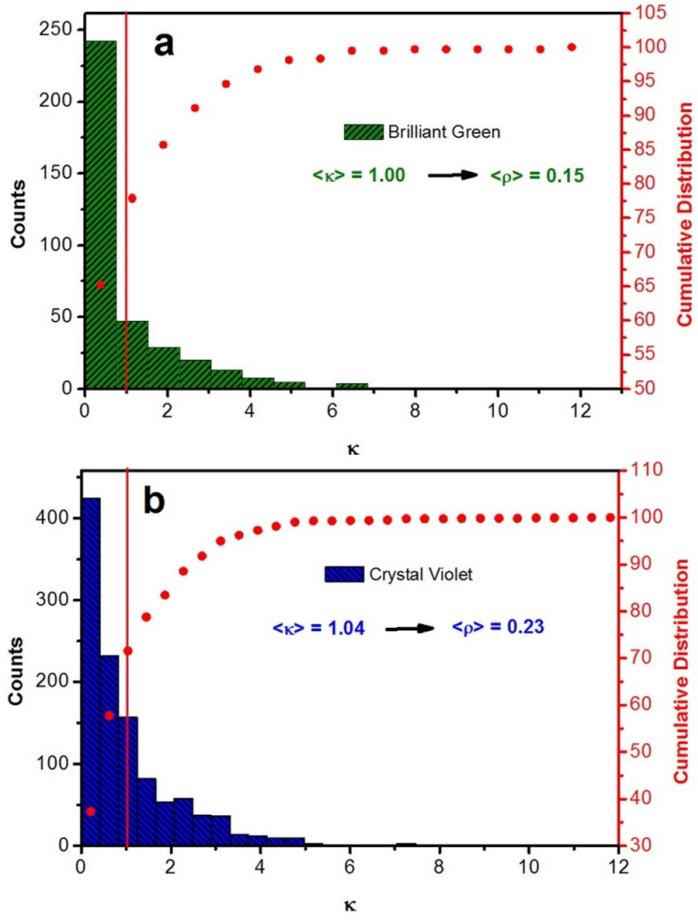

Figure 1.13. Histogram of counts for ρ for the 198 and 219 cm^{-1} modes of A) brilliant green and B) crystal violet, respectively, plotted as a normalized κ value. The κ value is ρ of a SM divided by the average ρ of the ensemble. Adapted with permission from reference [118]. Copyright 2012 American Chemical Society.

and CV shown in Figure 1.13.[118] They used a normalized κ value, defined as ρ of a SM divided by the ensemble averaged ρ. The mean κ values were 1.00 and 1.04 for BG and CV, respectively. The equal ρ for the SM and ensemble regimes showed that the average SERS signal is the combination of contributions from all the individual hot spots illuminated

during the SERS experiment. They also found that the distribution in κ values was the same for both analytes. As a consequence, the variability of ρ for different SM events is expected to result from nonequivalent enhancement of the Stokes or anti-Stokes scattering and not from a molecular effect. This conclusion was later supported by an investigation where the distribution of ρ for R6G was found to span more than 1.5 orders of magnitude, which will be covered in depth in Chapter 4.[116] The heterogeneous enhancement of the anti-Stokes and Stokes scattering is believed to be the main contributor to the distribution in ρ observed for SMs.

Another recent study by Pereira dos Santos et al., approached this phenomenon from a different perspective and used ρ of single CV molecules to probe the aggregation state of Ag colloids.[119] The experimental results were interpreted within the framework of generalized Mie theory simulations. Figure 1.14 shows the electric field enhancement profiles (E/E_0 as a function of incident wavelength) for the hot spots of Ag nanospheres of 25 nm in diameter. With increasing aggregation state, the resonances are red shifted and the maximum E/E_0 decreases. From these simulations, it is expected that for a Ag dimer at 633 nm excitation the anti-Stokes scattering would be enhanced relative to the Stokes scattering. For larger aggregates the Stokes scattering would be preferentially enhanced. They tested these predictions by using different KBr concentrations to influence the aggregation state of the Ag nanoparticles. Small aggregates (i.e., dimers and trimers) dominated with [KBr] $\leq$7.5 mM, and larger aggregates dominated at [KBr] $>$7.5 mM. At low KBr concentrations (2.5 mM), the anti-Stokes SERS signal was observed at 633 nm excitation but not at 785 nm, as seen in Figure 1.14C. As the KBr concentration was increased, shifting the resonances towards 785 nm excitation, the observation of SERS intensities at

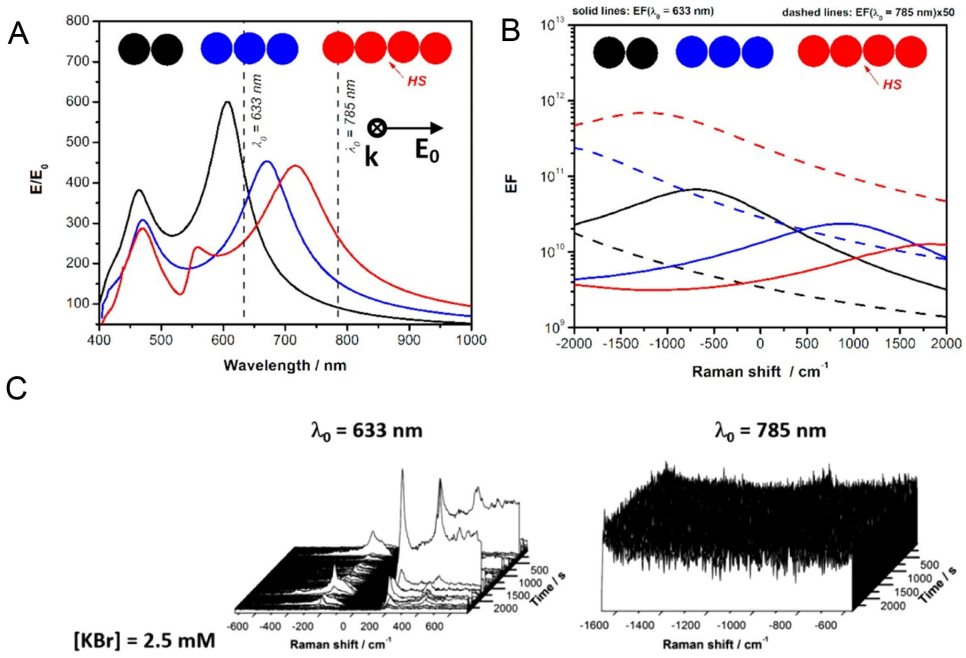

Figure 1.14. A) Generalized Mie theory simulations for the local field enhancement (E/E_0) at the junctions between nanoparticles. The colors in the plots represent different aggregation states of 25 nm radius Ag nanospheres as indicated in the schematic. B) Simulated SERS EF profiles as a function of the Raman shift for molecules located in the nanoparticle junctions. Solid lines indicate excitation at 633 nm and dashed lines indicate 785 nm. C) SERS fluctuations of crystal violet aggregated with 2.5 mM KBr at 633 nm excitation (left) and 785 nm excitation (right). Strong fluctuations are observed at 633 nm excitation. SERS signal is not observed at 785 nm excitation. Adapted with permission from reference [119]. Copyright 2016 American Chemical Society.

785 nm increased, while those at 633 nm decreased. Furthermore, the anti-Stokes signal at 633 nm excitation only extended out to -600 cm^{-1}, while at 785 nm the Raman shifts were visible out to -800 cm^{-1}. These experimental results are in good agreement the model presented in Figure 1.14, where, for larger aggregates, the plasmon resonance broadens. This work suggests that the local structure of nanoparticle aggregates can be probed with SMSERS because, as previously discussed, the SMSERS signal is strongly dependent on the local field properties of the nanostructure.

1.5.4. Pressure-Induced Blue Shift of Vibrational Modes

The ability to study single molecules under high pressure would deepen our understanding of the broadening and blue shifting of vibrational modes in Raman spectroscopy. Pressure-induced blue shifts of molecular vibrations can arise from anharmonic coupling between intramolecular vibrations and the environment. When molecules are present in disordered media such as Ag colloids under pressure, individual molecules will experience different anharmonic coupling to the environment resulting in varied pressure-induced blue shifts for the vibrational modes. Fu and coworkers investigated the effect of pressure on vibrational modes in SERS and SMSERS from 1-4 GPa.[121] For these studies, the SERS substrate consisted of aggregated Ag nanoparticles embedded in a polyvinyl alcohol matrix shown in Figure 1.15. The substrate was then placed in a diamond-anvil cell to accommodate the high pressures, which resulted in ∼25% compression of the sample at the highest pressure of 4 GPa. SM detection was verified using the R6G isotopologues. As shown in Figure 1.15A, the brightness of each pixel in the scan correlates to the integrated intensity of the ∼1650 cm^{-1} R6G mode (in-plane stretching of the xanthene moiety), which

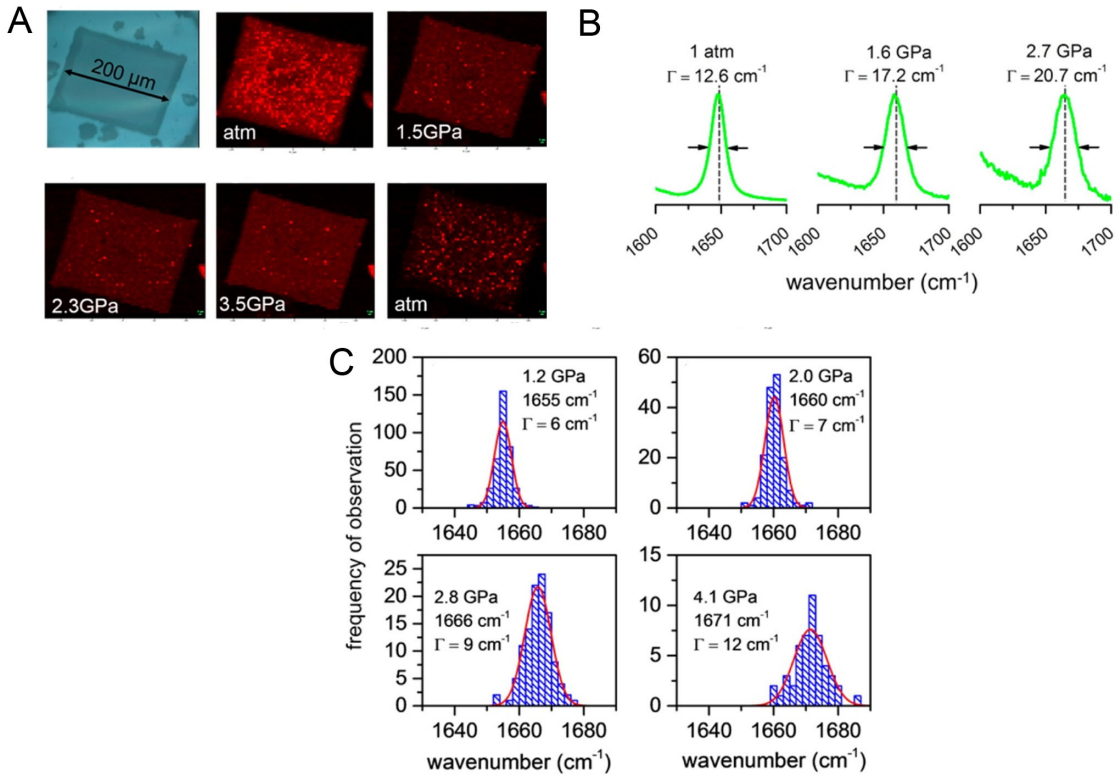

Figure 1.15. A) Photograph (top left) and Raman microscope images of the SERS substrate placed in a diamond-anvil cell. The pressures are indicated in each scan beginning and ending with atmospheric pressure. The brightness at each pixel corresponds to the integrated intensity of the ∼1650 cm^{-1} mode of R6G. B) Ensemble average of many SMSERS spectra of the R6G isotopologues, indicating the blue shift and peak broadening at higher pressures. C) Histograms of the peak location for the SMSERS events at different pressures. Adapted with permission from reference [121]. Copyright 2015 American Chemical Society.

shifts ∼5 cm^{-1} GPa^{-1}. An initial, rapid drop in SERS intensity at 1.5 GPa is believed to result from a pressure-induced destruction of numerous hot spots from compression of

the sample. With the surviving hot spots, the authors were able to observe the effect of pressure on the SERS spectra of R6G. They observed a broadening in linewidth and a blue shift in peak frequency for the ensemble averaged 1650 cm^{-1} mode shown in Figure 1.15B. Figure 1.15C shows the histogram of the ∼1650 cm^{-1} peak locations for the SMSERS spectra at different pressures. The magnitude of the blue shift varied between SM events, as expected, and became more pronounced as the environment was further compressed under pressure. The linewidth increase in the ensemble spectra of R6G results from the variability in blue shift from molecule-to-molecule. Each molecule is located in a different hot spot structure (i.e., environment) leading to differences in anharmonic coupling at each molecular site and, therefore, different blue shifts. Using insights from SMSERS, the pressure-dependent ensemble SERS measurements were explained by the anharmonic shifts of various molecule-environment interactions.

1.5.5. Excitation Wavelength Dependence of SMSERS

The excitation-wavelength dependence of SMSERS was characterized using a tunable optical parametric oscillator to finely tune the excitation wavelength across the molecular resonance of a single R6G molecule (i.e., ∼500-575 nm).[122] The Raman excitation profiles (REP) for ensemble R6G (black line) and a SM of R6G (black circles) on Ag are shown in Figure 1.16. The SM REP was obtained from the sum of all the observed Raman modes and was fit to a Lorentzian function (red), producing a FWHM of ∼400 cm^{-1}. As expected, the SM REP is narrower than the ensemble and was dominated by homogenous broadening. This study was the first example of a high density REP (i.e., finely tuned wavelength scan) across the molecular resonance of a SM. Collecting a distribution of

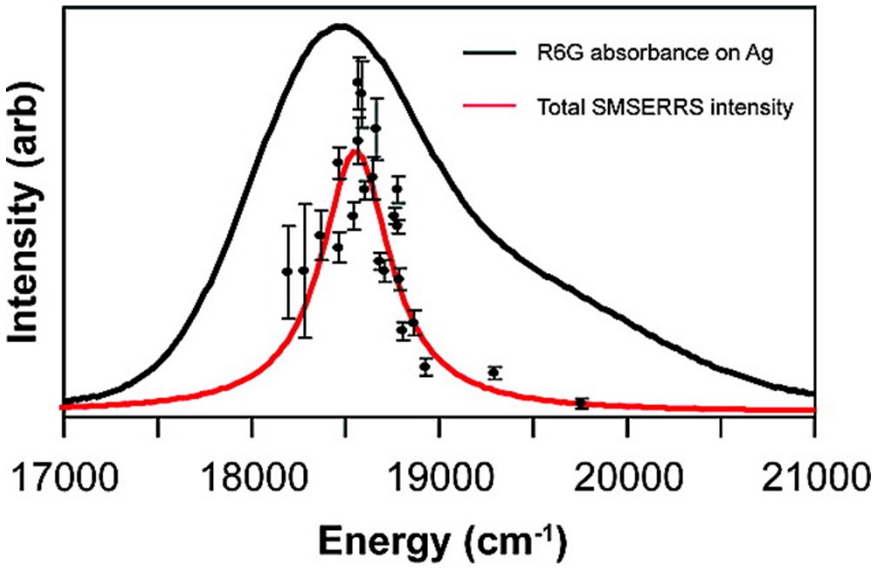

Figure 1.16. Overlay of the ensemble-averaged surface absorbance spectrum of R6G on Ag with the SMSERS REP on Ag nanoparticles. The single molecule data points (black circles) were obtained from the sum of all the observed Raman modes and were fit to a Lorentzian function (red). The error bars represent 1 standard deviation from the mean. The molecular absorption spectrum of R6G on Ag (black line) was fit by the sum of two Gaussian distributions. The SM REP is narrower than the ensemble-average analogue. Adapted with permission from reference [122]. Copyright 2008 American Chemical Society.

REPs with correlated nanoparticle structures could help improve our understanding of how local environments influence the energy, linewidth, and population distribution of SMs that cannot be observed with ensemble averaging.

1.6. Summary

Over the past two decades, SMSERS has become an established technique for characterizing molecular systems in nanoscale environments. It combines the inherent chemical selectivity of vibrational spectroscopy with plasmonically-enhanced signals to achieve SM sensitivity. Throughout this chapter, we have covered the current understanding of SMSERS including hot spots and EF distributions, the rational design of plasmonic substrates, the verification of SM detection, and signal fluctuations. The following four chapters of this dissertation will cover recent fundamental advances in SMSERS. Then, we will conclude with a review of recent applications and a discussion on future directions for SMSERS.

CHAPTER 2

A Critical Analysis of the Bianalyte vs. Isotopologue Proof

2.1. Introduction

Initial acceptance of SMSERS as a viable technique was impeded by the complexity of proving SM detection. Chapter 1 Section 1.3 covers the challenges and early strategies used for proving SM detection and the dilution procedures proposed for reliable SMSERS sample preparation. The current methodologies used for verifying SMSERS are the bianalyte[56,96,123] and isotopologue[19,40,121,124] approaches. Both approaches involve dosing a SERS-active substrate with an equimolar mixture of two analytes. The bianalyte approach uses two different analyte molecules, whereas the isotopologue approach uses an analyte and an isotopically-labeled version of that analyte. The key advantage of isotopologues is that the two analytes will have identical surface binding chemistries, overall Raman cross sections, and extinction coefficients for molecular electronic resonance. To verify SMSERS, events with the individual analytes should be preferentially observed over events with both analytes.*

A combined Poisson and binomial distribution (Equation 1.2) was proposed for the isotopologue method to model the number of molecules of Isotopologue 1 and Isotopologue 2 detected per spectrum.[40] The probability of SM detection is represented by the Poisson distribution, and the probability that the observed event will correspond to either

*This Chapter is reproduced with permission from reference [57]. Copyright 2016 American Chemical Society.

Isotopologue 1 or Isotopologue 2 is represented by a binomial distribution (assuming a 50:50 probability of either Isotopologue 1 or 2 as the identity of a given molecule). From this model, Dieringer et al. proposed a theoretical SM level threshold at $\alpha = 1$ (i.e., a mean of 1 molecule per nanoparticle aggregate).[40] This threshold requires that at least 76% of the spectra must indicate the character of a single isotopologue over a combination of both isotopologues to prove SM sensitivity.

The above analysis is problematic for bianalyte pairs because they will have different binding affinities and Raman cross sections. As a consequence, the isotopologue method is preferred, but it is subject to practical limitations such as cost and synthetic complexity. Moreover, the isotopologues must have a significant, observable spectral peak shift to allow accurate identification of the two isotopologues. Under these limitations, the bianalyte approach can be experimentally unavoidable, meaning it is critical that we elucidate the necessary experimental considerations to convincingly demonstrate SM sensitivity with the bianalyte method.

To probe the limitations of the bianalyte approach for SMSERS, we undertake the first multi-analyte SMSERS experiment. We dosed Ag colloids with two pairs of isotopologues: Rhodamine 6G (R6G-d_0, R6G-d_4) and crystal violet (CV-d_0, CV-d_{12}). The bianalyte pair (R6G and CV) can be directly compared, while simultaneously proving SMSERS using their corresponding isotopologues as an internal standard. From these results and a detailed discussion of a joint Poisson-binomial model under conditions of unequal analyte detection, we outline the considerations necessary for accurate implementation of SMSERS proofs. Furthermore, we demonstrate that multi-analyte studies

at the SM level are a viable approach for future investigations, such as monitoring SM chemical reactions.

2.2. Experimental Methods

2.2.1. SMSERS Sample Preparation

Table 2.1. Solution concentrations for R6G and CV in the bianalyte and multi-analyte studies.

Data Set	R6G-d_0 (M)	R6G-d_4 (M)	CV-d_0 (M)	CV-d_{12} (M)	Total (M)
A	$1x10^{-7}$	-	$1x10^{-7}$	-	$2x10^{-7}$
B	$1x10^{-8}$	-	$1x10^{-8}$	-	$2x10^{-8}$
C	$5x10^{-8}$	$5x10^{-8}$	$5x10^{-8}$	$5x10^{-8}$	$2x10^{-7}$
D	$5x10^{-9}$	$5x10^{-9}$	$5x10^{-9}$	$5x10^{-9}$	$2x10^{-8}$
E	$1x10^{-9}$	$1x10^{-9}$	$1x10^{-9}$	$1x10^{-9}$	$4x10^{-9}$
F	$1x10^{-10}$	$1x10^{-10}$	$4x10^{-9}$	$4x10^{-9}$	$8.2x10^{-9}$

The borohydride-reduced Ag colloids were synthesized following a previously reported procedure with slight modification.[56] All glassware was cleaned with aqua regia (3:1 HCl/HNO_3) and dried in an oven. Millipore water (80 mL, 18.2 MΩ·cm) was added to a 250 mL beaker cooled with an ice bath. Under constant stirring conditions, 18 mg of $AgNO_3$ (Sigma) and 8 mg of KCl (Sigma) were dissolved in the Millipore water. This solution turned pale blue and was stirred on ice for ∼10 min. Meanwhile, 6 mg of $NaBH_4$ (Sigma) was dissolved in an additional 20 mL of ice-cooled Millipore water. The $NaBH_4$ solution was poured directly into the first solution at the end of the 10 min. Upon this addition, the solution transited from yellow to dark brown to opaque light green within ∼2 min. The colloidal solution was stirred for an additional 1 min before removal from the

ice bath. Finally, the solution was allowed to warm to room temperature, while stirring, for 30 min. The colloids were stored in a brown glass bottle in a nitrogen box and used within one week.

After synthesis, the colloids were concentrated by centrifugation for the SMSERS experiments. In a centrifuge tube, 1 mL of as-prepared colloids was centrifuged for 5 min at 5000 rcf, followed by removal of the supernatant. This process was repeated 4 more times (i.e., total 5 mL of colloids into 1 sample), and the colloids were dispersed to a final volume of 100 μL ($\sim$50 fold increase in concentration) with Millipore water by vortexing for 30 sec. In accordance with the dilution procedure described previously, to avoid surface coverage nonuniformity, we did not employ large dilution factors.[89] Instead, we added 50 μL of the dilute dye mixtures to the concentrated colloids and vortexed for 1 min to thoroughly mix. The concentrations of the multi-analyte and bianalyte dye mixtures varied for each dataset (Table 2.1). These dyes included Rhodamine 6G (R6G-d_0, Sigma), crystal violet (CV-d_0, Sigma), and their isotopologues (R6G-d_4 and CV-d_{12}, custom synthesis as previously described).[19,40] The colloid/dye mixtures were allowed to incubate in a N_2 environment for 2 hours. Glass coverslips (25 mm, #1.5) were piranha cleaned (3:1 H_2SO_4 /30% H_2O_2) and base treated (5:1:1 H_2O /NH_4OH /30% H_2O_2), and then dropcast with 10 μL of the colloid/dye mixture and dried with a N_2 gun. This step was repeated twice (total drop volume of 20 μL) to ensure adequate nanoparticle coverage for scanning.

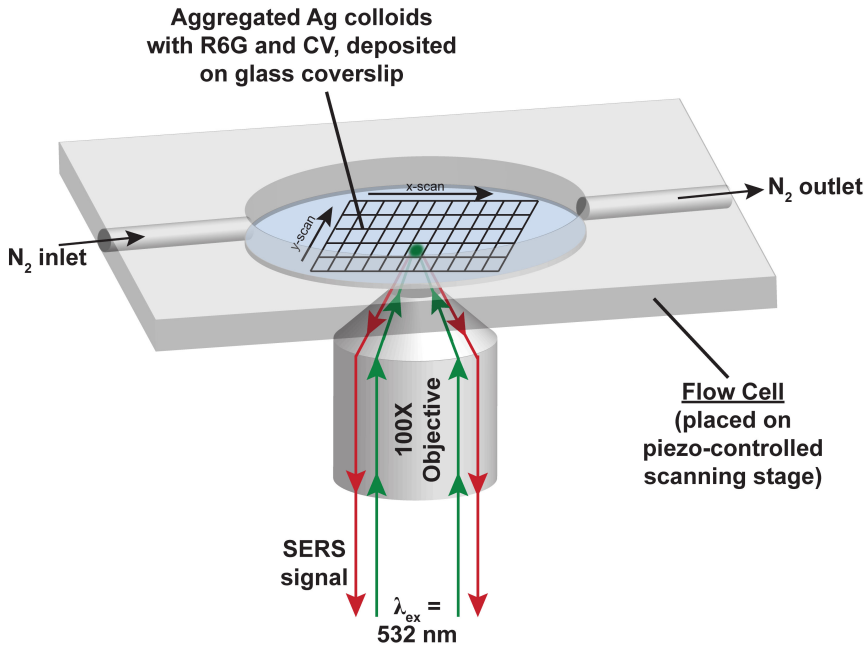

Figure 2.1. Schematic of data collection. The Ag colloid/dye mixture was dropcast on glass coverslips. Then, the coverslips were placed in a flowcell for immersion in a N_2 atmosphere. The substrates were scanned in the x- and y- direction with a 2 μm step size using a 100$\times$ oil immersion objective and 532 nm excitation. A spectrum was collected at each "pixel" of the scan for 1-5 sec with an incident power of 6-7 μW.

2.2.2. Instrumentation and Scans

The SMSERS substrates were mounted in a custom-built flow cell under a positive pressure of N_2 for the entire duration of data collection to minimize photodegradation. The SMSERS signal was collected in a backscattering geometry on an inverted microscope (Nikon TE300) with a 100$\times$ oil immersion objective (Nikon, NA = 1). The excitation wavelength was 532 nm (Spectra-Physics, Millenia X) with a spot size of $\sim$1 μm^2. A

long-pass filter was used to filter the Rayleigh scattering (Semrock, LP03-532RS-25). The collected signal was dispersed with a 1200 grooves/mm grating and detected with a liquid N_2-cooled CCD (Action 300i, Spec-10 400B).

The SMSERS substrates were scanned with a piezo-controlled stage (E-710 Digital PZT) with a step size of 2 μm in the x- and y-directions. The step size was chosen to be larger than the laser spot size ($\sim$1 μm^2) to limit exposure of the molecules to the laser during long scans. At each step of the scan, a spectrum was collected for 1-5 seconds with an incident power of 6-7 μW. Only events that were clearly distinguishable as R6G-d_0, R6G-d_4, CV-d_0, CV-d_{12}, or a combination thereof were counted. Spectra with spurious peaks which were attributed to R6G or CV photodecomposition products or carbonaceous species were not counted.[92,95] It should be noted that many of the spectra in the scans were blank. This is the result of the low concentrations used and the typically small percentage of SMSERS-active nanoparticles.[22] As a result, multiple scans were run to build each dataset. A schematic of the experimental set-up is provided in Figure 2.1.

2.3. Results and Discussion

2.3.1. Bianalyte and Multi-Analyte SMSERS

We pursued multi-analyte studies to investigate the limitations of the bianalyte method for SMSERS. Figure 2.2 shows example SMSERS spectra of R6G, CV, and their corresponding isotopologues collected from Ag colloids incubated with a dilute mixture of all four analytes. R6G-d_0 has a strong, isotopically sensitive mode at 614 cm^{-1}, which upon deuteration of the phenyl moiety (R6G-d_4) shifts to 600 cm^{-1}.[40] A histogram tabulating

the peak frequencies for the 600 cm^{-1} region mode of R6G and additional spectra are provided in the Figure 2.3. The peak frequency distributions show minimal overlap. The 5 spectra with peak frequencies between 605-606 cm^{-1} are shown in Figure 2.3B. The 1340 cm^{-1} mode of R6G-d_4 was used as a secondary verification of the isotopologues. This data highlights the benefit of having multiple Raman modes for distinguishing isotopologue identity.

As discussed in previous literature,[19] upon deuteration of CV-d_0 to CV-d_{12}, many subtle changes in peak frequencies occur. The most prominent feature is the shift of the 1620 cm^{-1} band in CV-d_0 to 1607 cm^{-1} in CV-d_{12}. While this mode can be used for differentiating the CV isotopologues, it can be obscured by R6G modes in the same spectral region. A convenient point of contrast between CV and R6G are the 630 to 750 cm^{-1} and 780 to 900 cm^{-1} regions, in which R6G is featureless. In these regions, CV-d_0 has bands at 720 cm^{-1} and 800 cm^{-1}, and CV-d_{12} has bands at 700 cm^{-1} and 840 cm^{-1}. Throughout the rest of this study, the bands between 600-800 cm^{-1} and 1600-1630 cm^{-1} were used to differentiate the SMSERS spectra for the various analytes. Example multi-analyte spectra showing instances of 3 or 4 analytes are shown in Figure 2.4.

Datasets A and B (Figure 2.5) correspond to two bianalyte experiments completed with equimolar mixtures of R6G-d_0 and CV-d_0. In Dataset B, order of magnitude lower concentrations were used compared to those in Dataset A (see Table 2.1). The CV/R6G column in the bianalyte histograms accounts for any instances in which both R6G-d_0 and CV-d_0 were detected in the SERS spectrum. In Dataset A, 76% of the spectra showed individual analyte character of either R6G or CV, but not both. In Dataset B, 95% of the spectra showed individual analyte character.

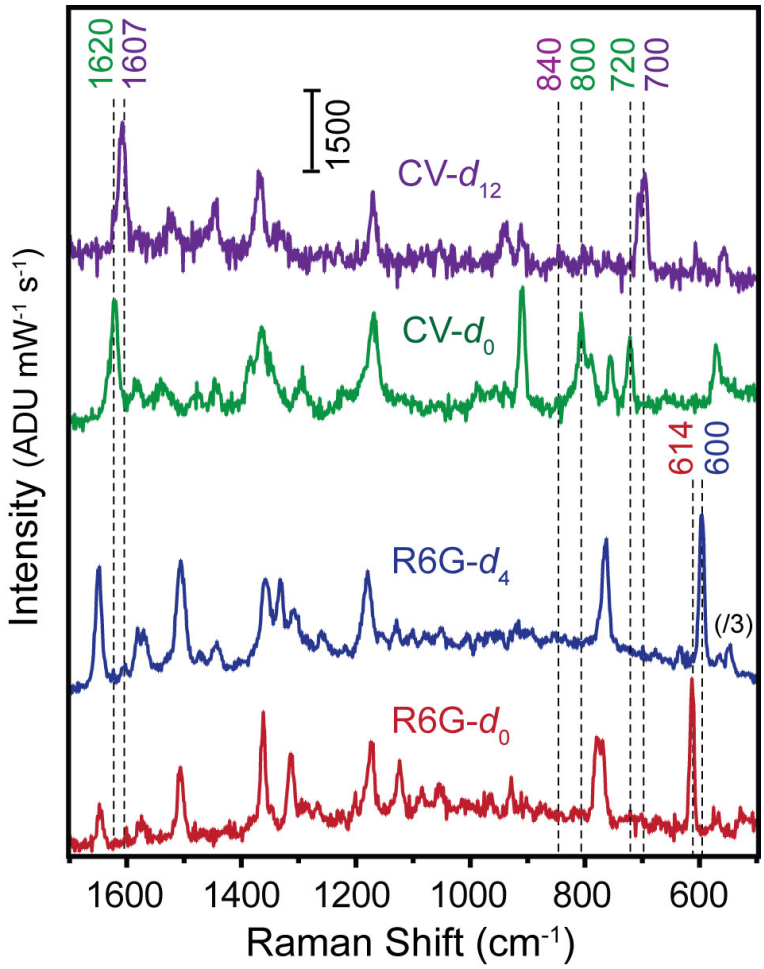

Figure 2.2. Example SMSERS spectra of R6G-d_0, R6G-d_4, CV-d_0, and CV-d_{12} collected from Ag colloids dosed in a dilute mixture of all 4 analytes. Only the character of each individual analyte is observed. Characteristic modes used for the identification of each analyte are indicated.

Recall from Equation 1.2 that to satisfy a theoretical SM level threshold at $\alpha = 1$, or on average one molecule per spectrum, at least 76% of the spectra must indicate individual analyte character. On first glance, Datasets A and B satisfy this threshold, suggesting SM level coverage in both cases. However, we found that the counts for R6G were an order

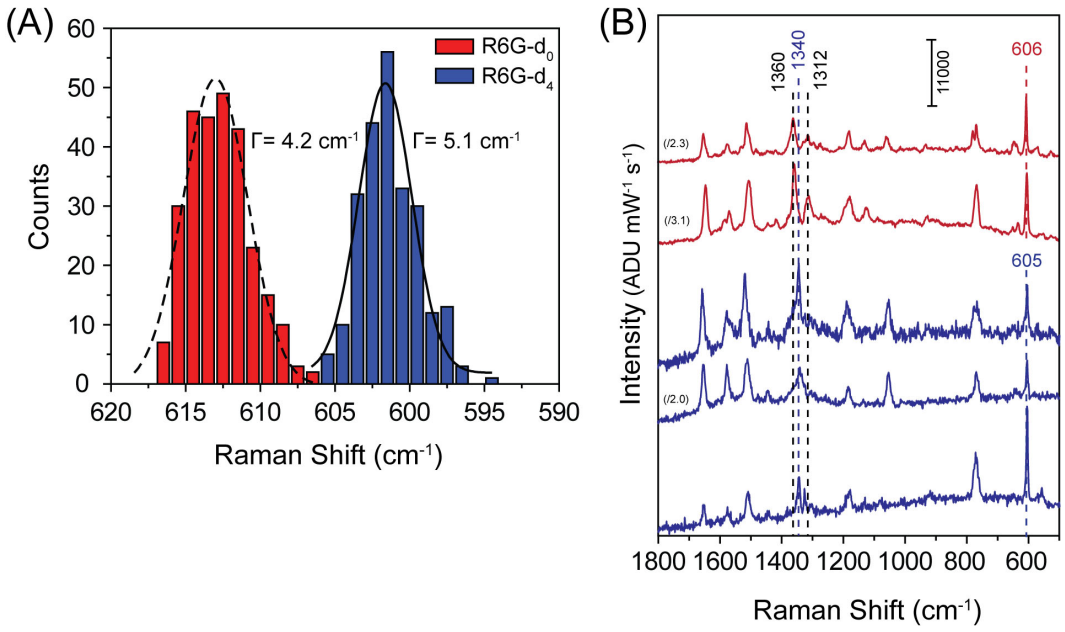

Figure 2.3. A) Histogram of tabulated peak frequencies for R6G-d_0 and R6G-d_4 illustrating the degree of spectral wandering observed amongst 477 SMSERS events. The centers (and FWHMs) of the Gaussian fits are at 613.0 cm^{-1} (4.2 cm^{-1}) and 601.6 cm^{-1} (5.1 cm^{-1}), respectively. The distributions show minimal overlap. The 5 spectra with peak frequencies between 605-606 cm^{-1} are shown in B. The 1340 cm^{-1} mode of R6G-d_4 was used as a secondary verification of the isotopologues.

of magnitude higher than those of CV for both Datasets A and B (∼14 and ∼11 times, respectively). The observation of this trend over hundreds of counts suggests that the detection probabilities of CV and R6G are significantly different. The large discrepancy in counts between R6G and CV is attributed to differences in their adsorption affinities and resonance Raman cross sections. Different binding affinities will result in unequal molecular coverage on the SERS substrate, favoring the detection of the analyte with the

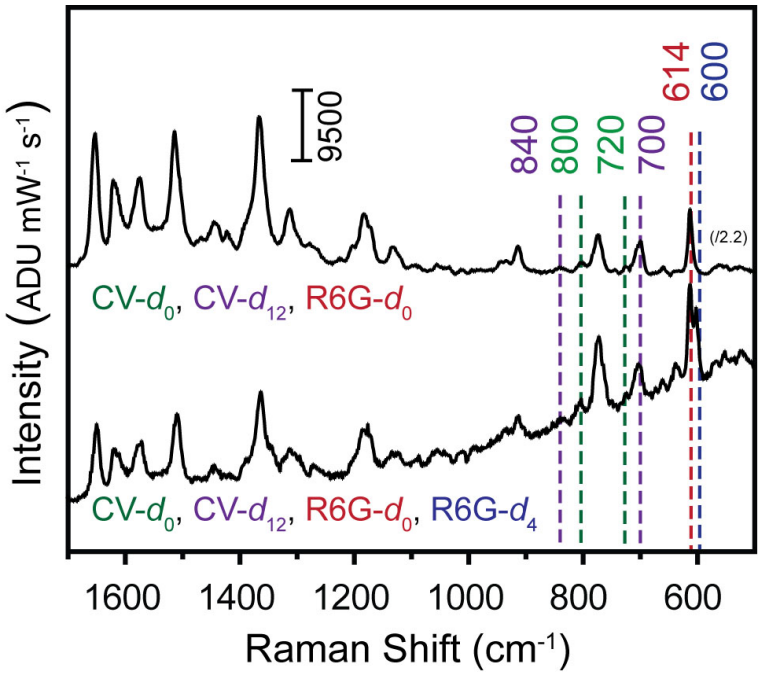

Figure 2.4. Example multi-analyte spectra collected. The top spectrum indicates the presence of 3 analytes (CV-d_0, CV-d_{12}, R6G-d_0) and the bottom spectrum indicates the presence of all 4 analytes.

stronger affinity. Clearly, the assumption in Equation 1.2 of a 50:50 detection probability for CV and R6G is not valid. Therefore, Datasets A and B may not actually satisfy the theoretical threshold for SM detection. This will be addressed in a subsequent section, but first, to experimentally verify whether or not these datasets are at the SM level, we conducted analogous multi-analyte experiments.

Datasets C and D provided in Figure 2.5 correspond to multi-analyte experiments conducted under identical conditions to those for Datasets A and B, respectively. For the multi-analyte studies, the Ag colloids were dosed with equimolar dye mixtures of all four analytes. The individual concentrations of R6G-d_0 and R6G-d_4 (or CV-d_0 and CV-d_{12}) in Dataset C sum to the total concentration of R6G-d_0 (CV-d_0) dosed onto

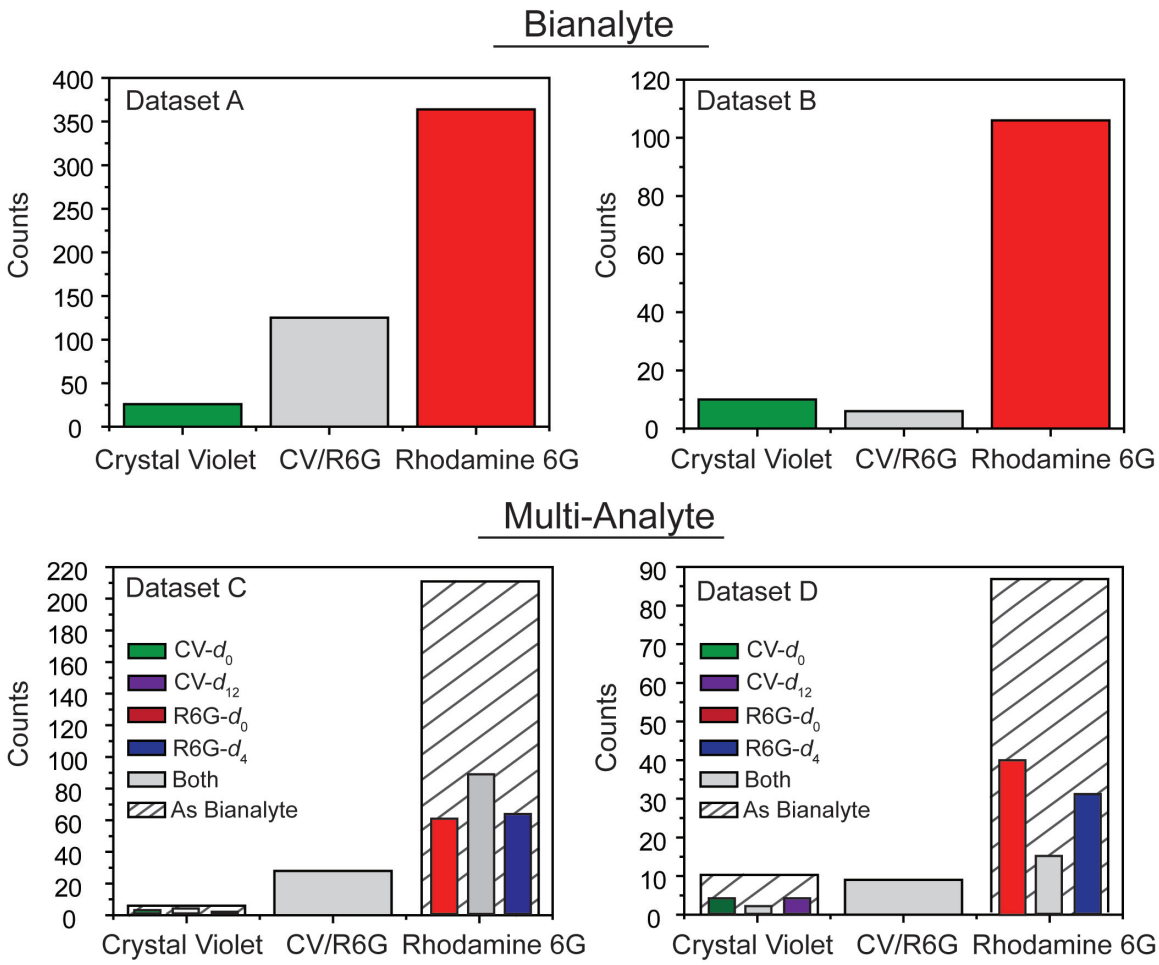

Figure 2.5. Histograms of counts for bianalyte SERS experiments conducted with CV-d_0 and R6G-d_0 in Dataset A at 1x10^{-7} equimolar concentration and Dataset B at 1x10^{-8} equimolar concentration. Datasets C and D are analogous multi-analyte experiments to Datasets A and B, respectively, conducted at an identical overall concentration but with the concentrations divided between the isotopologue pairs: CV-d_0, CV-d_{12}, R6G-d_0, and R6G-d_4. The columns filled with slashed lines are the sum of the individual events within the column, displaying the multi-analyte datasets as though they were a bianalyte experiment for direct comparison.

the nanoparticles in Dataset A. This dosing scheme was repeated for Datasets D and B at their order of magnitude lower concentrations. By following identical procedures for sample preparation and maintaining the same overall concentration, we are able to compare the purely bianalyte experiments with their analogous multi-analyte experiments. The multi-analyte studies allow us to distinguish, for an individual analyte's SERS events in the bianalyte approach (i.e., R6G or CV), between counts that have individual or both isotopologue character. As expected, if we sum all of the R6G-d_0/d_4 events and all of the CV-d_0/d_{12} events in the multi-analyte experiments, R6G is still preferentially observed by an order of magnitude over CV. For the multi-analyte histograms, the CV/R6G column accounts for all possible combinations of a R6G isotopologue with a CV isotopologue, including instances of 3 or 4 analytes.

Upon examination of the isotopologue distributions in Dataset C, we found that spectra containing either both R6G-d_0/d_4 or both CV-d_0/d_{12} were observed more frequently than their respective individual isotopologue spectra. Despite 76% of the spectra in Dataset A showing individual analyte character, the isotopologue internal standard in Dataset C demonstrates that these two analogous experiments were actually at the few-molecule level. In Dataset D, in which the concentrations were lowered by an order of magnitude, we found that individual R6G-d_0 and R6G-d_4 spectra were observed preferentially over the combination of both isotopologues. The same held true for the CV isotopologues. Thus, the circumstantial evidence of SMSERS for Dataset B was shown, via isotopologue internal standards, to be correct. It should be noted that while the individual isotopologue spectra for CV were preferentially observed over the presence of both

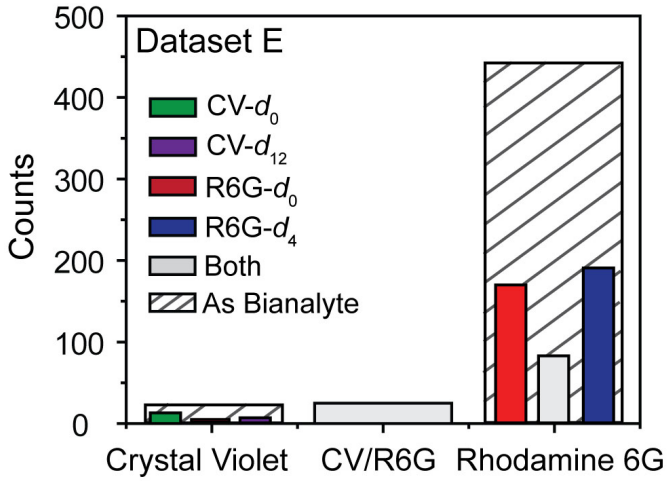

Figure 2.6. Histogram of counts for a multi-analyte experiment conducted with 1×10^{-9} equimolar concentration of R6G-d_0, R6G-d_4, CV-d_0, and CV-d_{12}. The observed counts for R6G were an order of magnitude higher than that for CV. This verifies that the trends in bianalyte behavior were reproducible across multiple concentrations.

isotopologues, the overall counts for CV were low. For a more rigorous demonstration of SMSERS, more counts are needed.

In summary, we experimentally verified that the largely different detection probabilities of R6G and CV can misleadingly imply SM detection, when it is not actually achieved. To provide further evidence that the trends we observed were reproducible, we completed a third multi-analyte experiment (Figure 2.6), at an additional order of magnitude lower concentration compared with Dataset D. Following the same trend, the observed number of counts for R6G were an order of magnitude higher than that for CV and SM detection was verified based on the isotopologues. This demonstrates that the trends in bianalyte behavior were reproducible across a 2 order of magnitude range of

equimolar concentrations ($1x10^{-7}$ to $1x10^{-9}$ M). In the following sections, the influence of Raman cross sections will be addressed, and the appropriate interpretation of bianalyte proofs will be examined.

2.3.2. Signal Intensity Variance

The detection probabilities for each analyte are controlled by their Raman cross sections, binding affinities, and solution concentrations. Here, we consider the importance of the Raman cross section for the bianalyte approach. The enhancement factor for Ag colloids, the most commonly utilized substrate for SMSERS, varies from hot spot to hot spot.[22,116,125] Also, the hot spot enhancement has been demonstrated to follow a long-tail distribution.[54,56] From a detection standpoint, this means that there is an effective region of the hot spot which can provide sufficient enhancement for the molecule to be detected above the noise. Therefore, the higher the analyte's cross section, the larger this effective region, and the more available sites the analyte has to be detected.

The Raman cross section of R6G at $3.26x10^{-24}$ cm^2 $molecule^{-1}$ sr^{-1} is an order of magnitude greater than that of CV at $2.85x10^{-24}$ cm^2 $molecule^{-1}$ sr^{-1} for the 614 cm^{-1} and 1620 cm^{-1} modes, respectively.[18,126] We predicted that this fairly large difference in cross sections would lead to unequal signal variances between R6G and CV events, with R6G having the larger variability in SERS intensities. Using the multi-analyte datasets found to be at the SM level (Datasets D, E, and F (Figures 2.5, 2.6, 2.11)), we examined the relative intensities for the 1600 cm^{-1} region modes of CV-d_0 and CV-d_{12}, and the 600 cm^{-1} region modes of R6G-d_0 and R6G-d_4. All spectra were normalized for excitation

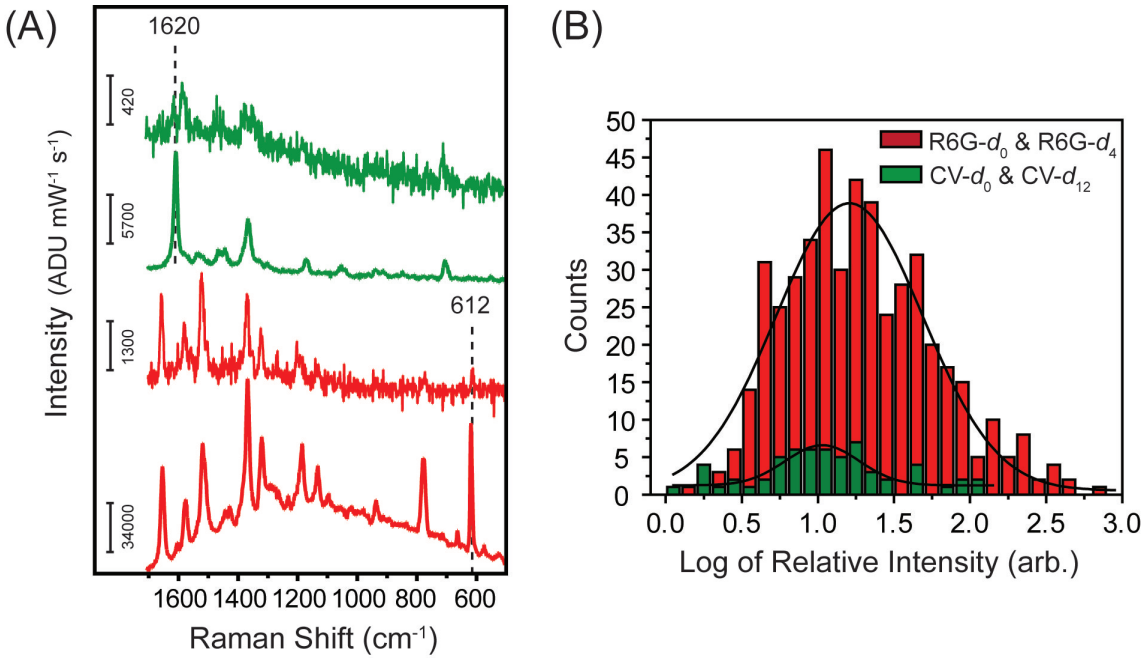

Figure 2.7. A) Example SMSERS spectra of R6G (red) and CV (green) highlighting the large intensity variations observed between different SM events. B) A histogram of the relative peak intensities, plotted on a logarithmic scale, for the 1600 cm^{-1} region mode of CV-d_0/d_{12} and the 600 cm^{-1} region mode of R6G-d_0/d_4. The variances for the CV and R6G intensities were found to be unequal with a p <0.001 (F-test).

power and acquisition time. Figure 2.7A provides example spectra for both R6G and CV, highlighting the large variability in signal intensity observed.

In Figure 2.7B, the histogram of the relative intensities is plotted on a logarithmic scale. We found that the relative intensities spanned almost 3 orders of magnitude for R6G and just over 2 orders of magnitude for CV. As predicted, from the fits of the histograms, we found that the variances for R6G and CV were unequal with a p <0.001 (F-test). The unequal variances highlight the importance of considering the Raman scattering cross

section along with binding affinities when using the bianalyte approach. Even if the molecules are present at equal coverage, the molecule with the weaker cross section may not be equivalently detectable above the noise, leading to different detection probabilities. As a consequence, it is preferential to choose bianalyte partners with cross sections within an order of magnitude of each other. It should be noted that while steps were taken to limit photodegradation, we cannot eliminate the possibility of differences in photostability between R6G and CV, which can contribute to the unequal variances in signal intensity.

2.3.3. Joint Poisson-Binomial Model

As discussed previously regarding the bianalyte approach, the detection probabilities of the two analytes will not be equivalent in most cases. To better understand the implications of this on the interpretation of bianalyte proofs, we generalized the proposed joint Poisson-binomial probability in Equation 1.2 to the bianalyte method:

$$P(\alpha, n_1, n_2, \beta) = \frac{e^{-\alpha}}{n_1! n_2!}[\alpha\beta]^{n_1}[\alpha(1-\beta)]^{(n_1+n_2)} \tag{2.1}$$

where α is the average number of molecules per scan pixel (each pixel corresponds to one spectrum), and n_1 and n_2 are the number of Analyte 1 and Analyte 2 molecules detected in the SERS spectrum, respectively. P is the probability that n_1 Analyte 1 and n_2 Analyte 2 molecules at α-coverage will be detected for a given spectrum. The probability that a given molecule detected in the spectrum corresponds to Analyte 1 is designated with an empirical variable β (value between 0 and 1; $\beta = 0.5$ for the isotopologue method which has a 50:50 ratio). The value of β is a function of the binding affinities, concentrations of Analytes 1 and 2, and Raman cross sections. While it remains a challenge to develop a

rigorous expression combining all of these factors, we can still examine how the value of β impacts the bianalyte method's validity in the context of this model.

We propose using the percentage of SERS spectra with individual analyte character to characterize whether or not SM levels have been achieved for a bianalyte experiment. As visualized in Figure 2.10A, this criterion is defined as the sum of the individual Analyte 1 and Analyte 2 counts, divided over the total spectral counts (Analyte 1 + Analyte 2 + both). For this criterion, spectra containing zero molecules are excluded. As can be expected, as the percentage of individual character increases, there is a higher probability of SM detection. For the remainder of this discussion, all calculated parameters from Equation 2.1 were computed using MATLAB for up to 10 of either Analyte 1 or Analyte 2 molecules contributing to the event. Beyond 10 molecules per spectrum and α <4, the probability calculated from Equation 2.1 is negligible.

Figure 2.8B depicts the calculated percentage of SERS spectra with individual character from Equation 2.1, plotted as a function of various α and β values. Figures 2.8C-D show the associated contours plotted as functions of α and β, respectively. In Figure 2.8C, it is evident that as the overall coverage of molecules increases (i.e., as α increases), the percentage of SERS spectra with individual character decreases (i.e., less likely to achieve SM detection). However, as the probability of detecting Analyte 1 deviates from 50% (i.e., when $\beta \neq 0.5$) and α is held constant, the percentage of SERS spectra with individual character increases (Figure 2.8D). Essentially, the higher probability of detecting Analyte 1 (or 2) leads to a greater number of individual Analyte 1 (or 2) counts, resulting in a "skewed" increase in the percentage of SERS spectra with individual character. With respect to interpreting the bianalyte experiments, this means that when the

binding affinities and Raman cross sections differ significantly between the two analytes (and the analytes are dosed at equimolar concentrations), a larger percentage of SERS spectra with individual character is required to demonstrate SM levels.

As mentioned earlier during the experimental discussion, a proposed definition for the theoretical SM level threshold is the point at which $\alpha = 1$. This corresponds to, on average, one analyte being detected per scan pixel and is visualized in Figures 2.8C-D with dashed lines. When the probability of detecting Analyte 1 is 50% ($\beta = 0.5$), at least 76% of the SERS spectra must exhibit individual character in order to reach SM levels. On first glance, both bianalyte Datasets A and B satisfied this requirement. However, as mentioned before, the discrepancy in counts between R6G and CV indicates that the probabilities of detecting CV and R6G (i.e., β) have shifted far from 50%. Assuming a $\beta = 0.1$, close to the ratio of counts between CV and R6G in our datasets, 91% of the SERS spectra must exhibit individual character in order to reach SM levels. This theoretical threshold fits well with the experimental results presented earlier: Dataset A (76% individual character) was not at SM level based on the isotopologue internal standard, whereas Dataset B (95% individual character) was at the SM level.

In order to explicitly evaluate whether or not the theoretical SM level threshold is met, an approach to estimate the values of α and β for an experiment is desired. The probabilities of detecting Analytes 1 and 2 should be related to the relative number of counts in the individual Analyte 1 versus 2 columns of the histogram. However, there are 4 variables that must be evaluated simultaneously: the relative number of individual Analyte 1 versus Analyte 2 counts, the total number of counts with both analytes, α, and β.

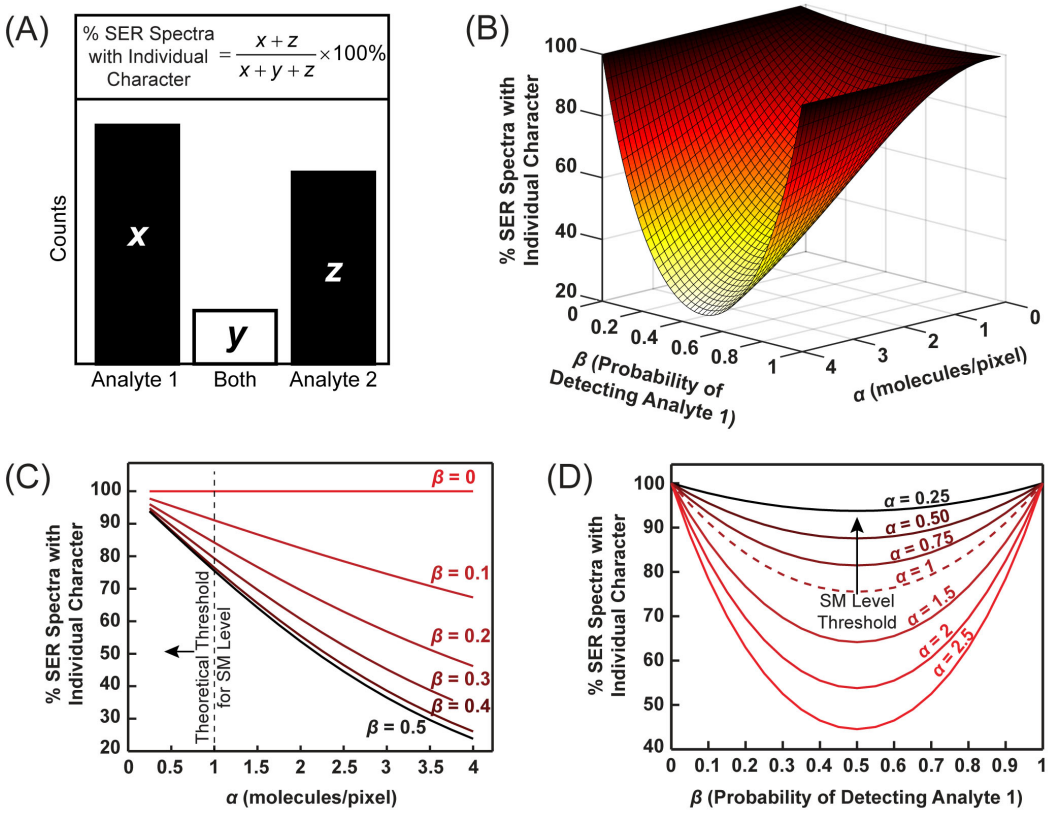

Figure 2.8. A) Schematic demonstrating how the percentage of SERS spectra with individual analyte character is defined with respect to the experimentally obtained histograms. B) Theoretically calculated percentage of SERS spectra with individual character from Equation 2.1, plotted as a function of the average number of molecules per scan pixel (α) and the probability that Analyte 1 will be detected (β). Note that the probability that Analyte 2 will be detected corresponds to (1-β). All calculations were done with MATLAB for up to 10 of either Analyte 1 or 2 molecules. C) Contours selected from B, plotted against α. D) Contours selected from B, plotted against β.

Here, it is worth noting that utilizing the relative intensities of Analyte 1 and Analyte 2 from an average spectrum of all events to estimate β (as opposed to the relative number of Analyte 1 versus 2 counts) is unreliable. First, consider the large variability in the intensities observed between SM events (3 orders of magnitude for R6G and 2 orders of magnitude for CV) as shown in Figure 2.7. Next, consider that in order to compare the joint Poisson-binomial model to the experimental data, the experimentally observed counts for each analyte must be used (the model is based on counting statistics). As discussed above, the signal intensity will clearly have zero correlation to the number of analyte counts—a certain number of analyte molecules will not necessarily correspond to an integer-multiplied signal intensity.[54] Furthermore, the average spectrum will be dominated by R6G due to the larger cross section and roughly 10× higher number of counts than CV. This obscures the presence of CV in the average spectrum despite the number of CV counts. This can be seen in the average spectrum of the SM events from Datasets D (Figure 2.9) where the CV-d_0 and CV-d_{12} peaks are barely distinguisable above the noise. In the situation that the signal intensity is directly proportional to the number of molecules, then the relative signal intensities could be used as a proxy for counts. This would require uniform enhancement factors for all molecules to remove the large signal variability, and knowledge of the Raman scattering cross sections for each of the analyte's peaks in order to correct for the cross sectional differences between analytes. In the instance of R6G and CV, however, this is not viable.

Figure 2.10 displays a pictorial method to determine α and β, given the percentages of SERS spectra with individual Analyte 1 and individual Analyte 2 character. Inevitably, values of α and β must be calculated from the model defined by Equation 2.1. This was

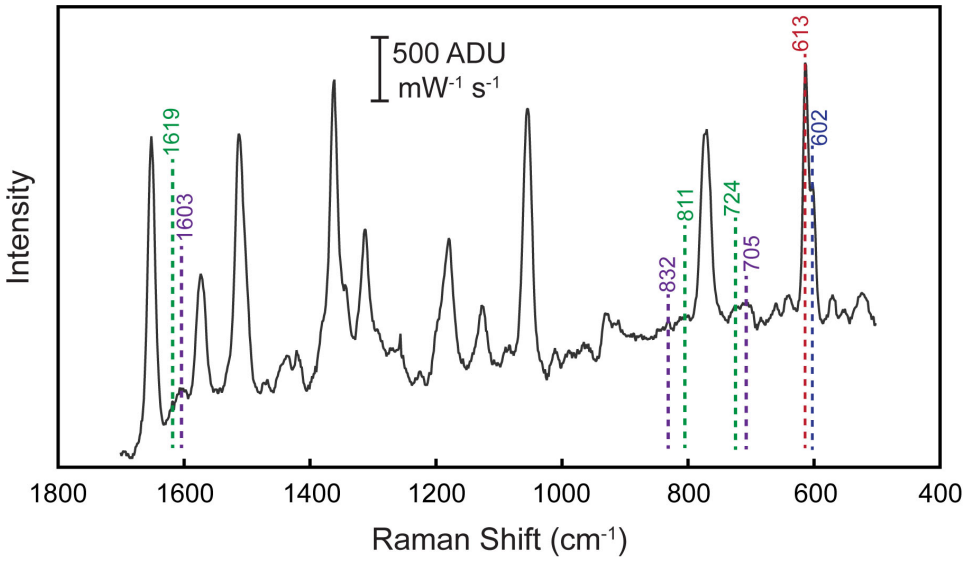

Figure 2.9. The average spectrum of all SM events from Dataset D (Figure 2.5). The average spectrum is dominated by R6G due to the larger cross section and roughly 10× higher number of counts than CV. This obscures the presence of CV despite the number of CV counts. The CV-d_0 (green) and CV-d_{12} (purple) peaks indicated on the spectrum are barely distinguishable above the noise.

accomplished by computing individual Analyte 1 and Analyte 2 percentages for a variety of α and β, and locating the point at which the experimental individual Analyte 1 and 2 percentages, α, and β values simultaneously match. The calculated values for Datasets A ($\alpha = 2.06$, $\beta = 0.15$) and B ($\alpha = 0.52$, $\beta = 0.10$) align well with the experimental conclusions. The 5% difference in β-values for the two datasets is primarily a result of insufficient counts (thousands are needed for a more exact value). This highlights the preference to work in terms of "β-regimes"—those close to $\beta = 0.5$ (from 0.35 to 0.65), and those far from $\beta = 0.5$ (0 to 0.35 and 0.65 to 1). The β-regime close to $\beta = 0.5$ is

defined from 0.35 to 0.65 because in this range, the percentage of individual character spectra required for SM levels ($\alpha = 1$) only fluctuates by ~1%. Outside of this range, the SM level threshold changes drastically for different β values (see Figure 2.8D). Given the higher thresholds that must be met at β-regimes far from 0.5, it is experimentally preferable to employ one of the following strategies: 1) use isotopologues, 2) adjust analyte concentrations to enter a β-regime close to 0.5, or 3) select bianalyte partners with nearly identical molecular properties.

It is critical to emphasize that the model summarized by Equation 2.1 corresponds to the ideal case, and that it is challenging to exactly match the experimental results to the model without thousands of data points. Dieringer et al. discussed earlier that this model does not account for the fact that the SERS enhancement factor is non-uniform across the substrate surface, lowering the probability of finding both analytes in a hot spot.[40] In addition, the model assumes no spatial correlations between analyte-surface binding events (i.e., no dimerization or preferential clustering of analyte molecules). If the analytes preferentially cluster, this can increase the probability of detecting multiple same-analyte molecules clustered in a hot spot. This clustering effect can be experimentally minimized by selecting analytes that exhibit minimal dimerization at low concentrations, and by following the dilution procedures described by Darby et al.[89]

2.3.4. SMSERS with Unequal Analyte Concentrations

As addressed in the previous section, the ideal condition for a SMSERS proof is with equal detection probabilities of both analytes. One approach to account for differences

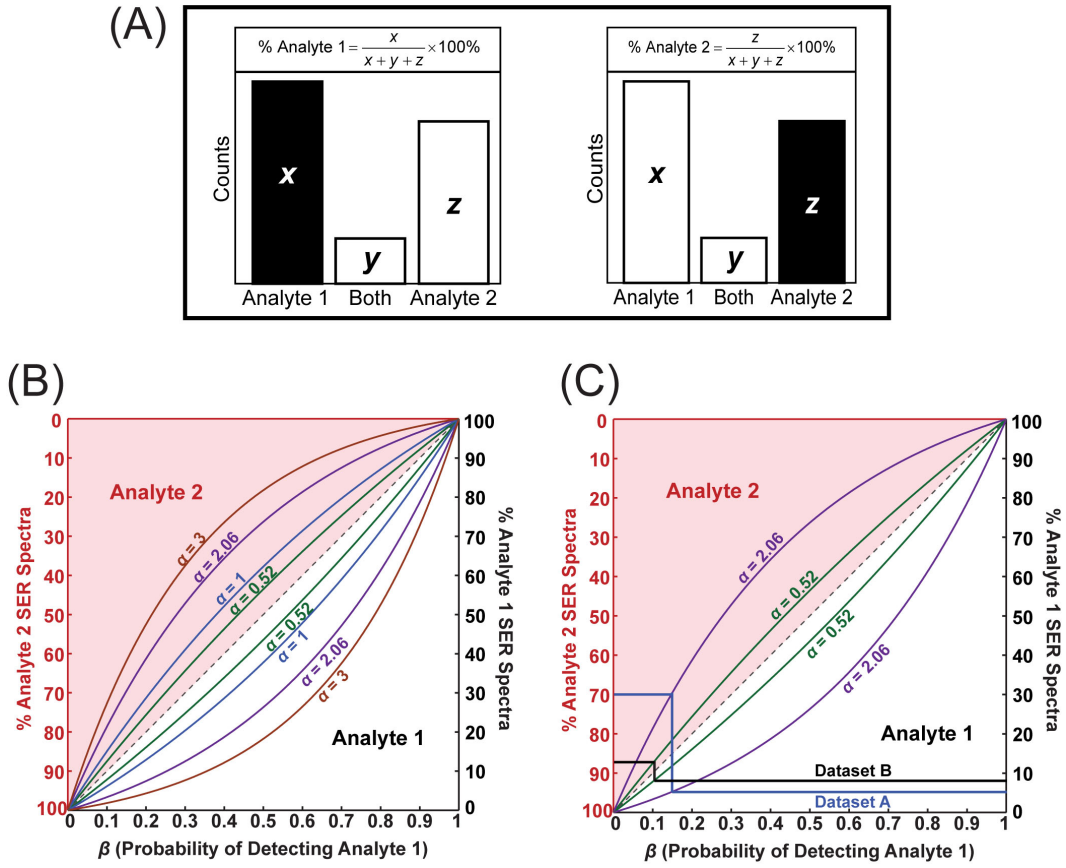

Figure 2.10. A) The percentages of individual Analyte 1 and Analyte 2 SERS spectra. The number of counts corresponding to both analyte character will be parametrically dependent upon the percentages of individual Analyte 1 and Analyte 2 SERS spectra. B) Visual demonstration of estimating the values of α and β. The α-contours on the bottom right half of the plot (white region) correspond to the percentage of Analyte 1 SERS spectra plotted against β, and the α-contours on the top left half of the plot (red region) correspond to the percentage of Analyte 2 SERS spectra plotted against β. C) The α and β values for Dataset A (blue line) and Dataset B (black line) were calculated and displayed on the plot.

in detection probability is to adjust the concentrations of the two analytes. We experimentally observed in all previously discussed datasets that R6G is preferentially detected over CV by roughly an order of magnitude. Based on this information, we determined that to achieve comparable counts for R6G and CV, the CV concentration needed to be at least a factor of 10 higher than the R6G concentration. The next step was to ensure that the CV and R6G concentrations were set at or below the coverage threshold required for SM levels. CV was demonstrated in our experiments to be in the few-molecule regime at $1x10^{-7}$ M (Datasets A and C). Therefore, we set the CV concentration well below this threshold at $4x10^{-9}$ M and lowered the R6G concentration further to $1x10^{-10}$ M. The histogram collected with this dilute mixture of all 4 analytes is shown in Figure 2.11A as Dataset F. The R6G counts are only 1.2 times higher than CV, instead of an order of magnitude. With a β-regime close to 0.5 and 94% individual character observed for the bianalyte interpretation, Dataset F is at the SM level. The isotopologue internal standards provide further evidence to support this conclusion. In Figure 2.11B, we provide a 100 μm x 82 μm reconstructed scan map displaying the locations and identities of the molecule(s) detected. Each pixel of the map is 2 μm x 2 μm, as described in the experimental section. From this map, it is clear that the various molecules are spread out and randomly dispersed across the surface. Thus, we were able to demonstrate that by altering the concentration ratios of the bianalyte molecules, we achieved SMSERS and equivalent counts of R6G and CV.

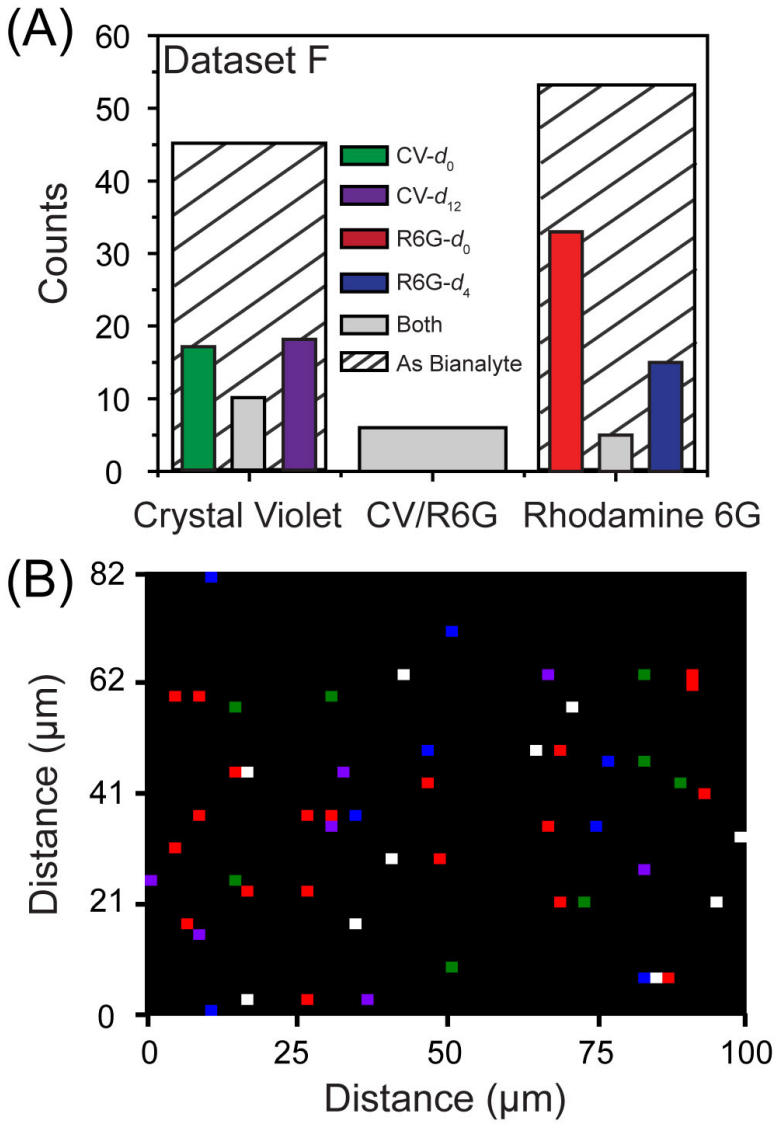

Figure 2.11. A) Histogram of counts for a multi-analyte experiment conducted with Ag colloids dosed with a 40 times higher CV concentration compared to the R6G concentration ($4x10^{-9}$ M and $1x10^{-10}$ M, respectively). B) 100 μm x 82 μm reconstructed scan map showing the locations of the molecules for one scan of Dataset F. A spectrum was collected at each 2 μm x 2 μm pixel of the map. The molecular identity is indicated by the color in A. The R6G counts are only 1.2 times higher than CV.

2.3.5. Thresholds for Verifying SMSERS

Another important consideration often overlooked is that the bianalyte and isotopologue proofs generally constitute "single analyte" and "single isotopologue" proofs. When at SM level coverage, it is possible that a single analyte spectrum may actually correspond to 2, 3, 4, or more molecules of the same analyte. This issue can be visualized in Figure 2.12. The percentage of single molecule events is defined as the fraction of individual Analyte 1 or 2 spectra that actually correspond to single molecules. In Figure 2.12B, the calculated (from Equation 2.1) percentage of single molecule events is plotted for various values of α and β. According to the model, for $\alpha = 1$ and $\beta = 0.5$, only 77% of the individual Analyte 1 or 2 counts correspond to actual SM events. The remaining counts correspond to events with 2 or more molecules. Thus, for the earlier defined $\alpha = 1$ SM threshold, while most of the individual counts correspond to single molecules, there remains a significant probability that an individual analyte spectrum corresponds to multiple molecules of the same analyte. Furthermore, when the probability of detecting Analytes 1 and 2 shift away from a 50:50 ratio, the analyte with a higher probability of detection has a lower percentage of actual SM events.

While we are currently unable to experimentally verify if a single analyte spectrum corresponds to 2 or more molecules, the multi-analyte experiments allowed us to resolve instances of 3 or 4 molecules in a single spectrum. At the few-molecule level (Dataset C), the occurrence of spectra indicating the presence of 3 or 4 analytes was 7% and 3%, respectively. Example spectra are provided in Figure 2.4. Moving to SM level coverage (Datasets D, E, and F), we found no instances of spectra with character from all 4 analytes, but 1% of the spectra still showed character of 3 analytes. It should be noted, due to

the discrepancy in counts between R6G and CV, these results likely underestimate the number of events with three or more molecules. These results demonstrate that SERS events with 2 or more molecules can contribute measurably to the total counts.

(A)

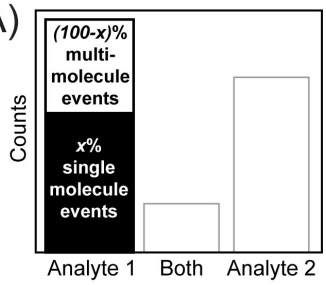

(B)

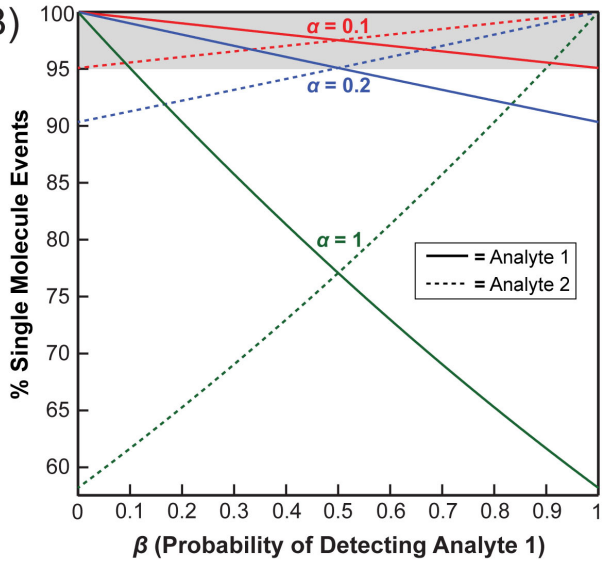

(C)

Defined SM Level Threshold	α	β-Regime	% SER Spectra with Individual Character
On average 1 molecule per spectrum	1	0 to 0.35	91.1%
	1	0.35 to 0.65	76.0%
	1	0.65 to 1	91.1%
95% of individual analyte SER spectra correspond to single molecules	0.10	0 to 0.35	99.0%
	0.16	0.35 to 0.65	96.2%
	0.10	0.65 to 1	99.0%

Figure 2.12. A) The x% of the individual Analyte 1 counts in the histogram corresponding to single molecule events. B) Theoretically calculated percentage of single molecule events, plotted as a function of β for different values of α. For on average one molecule per pixel, 77% of the individual analyte counts in the β-regime close to 0.5 correspond to single molecules. To achieve at least 95% confidence that an individual analyte spectrum corresponds to a single molecule (grey shaded region in B), $\alpha = 0.16$ or lower is desired depending on the β-regime. C) Table defining percentage of SERS spectra with individual character required to meet the defined theoretical thresholds for SM detection.

The non-negligible probability of simultaneously observing 2 or more same-analyte molecules highlights the importance of defining more rigorous thresholds for SM detection. A way to define this rigorous threshold is the point at which we have 95% confidence that an individual analyte's SERS spectrum corresponds to a single molecule. By calculation from Equation 2.1, for any β-value, at least 95% single molecule events for both analytes will be achieved at $\alpha = 0.10$ or less (i.e., at least 99% SERS spectra with individual character). In the β-regime close to $\beta = 0.5$, 95% single molecule events for both analytes is reached at $\alpha = 0.16$ (i.e., 96% SERS spectra with individual character). In practice, the SM threshold set at $\alpha = 1$ may be sufficient, such as when proving that a SERS substrate is capable of SM sensitivity. The second, more rigorous, threshold is best geared towards experiments which require demonstration that a single molecule is indeed being monitored. The two defined SM thresholds are summarized for each β-regime in Figure 2.12C.

2.3.6. Considerations for the Bianalyte Approach

Ideally, isotopologues will be used to prove SM detection for future SMSERS investigations. Isotopologues do not suffer from the limitations of bianalyte partners. When this is not a viable strategy, however, optimal bianalyte partners should be selected. The analytes should have clear spectral differences for unambiguous identification of the individual analytes and their mixtures. Next, the chosen bianalyte partners should have comparable Raman scattering cross sections (same order of magnitude) because even under the condition of equivalent molecular coverage, significantly unequal cross sections will lead to different detection probabilities. Another important consideration is that the selected analytes are reasonably photostable.[55] If one bianalyte partner degrades more

readily, the distribution of SERS events could be potentially skewed in favor of the more stable analyte.

Despite careful selection of the bianalyte partners, significant differences in binding chemistries may remain. To efficiently correct for differences in molecular coverage, the relative adsorption affinities of the two analytes to the SERS substrate should be known or estimated. Then, if the analytes have similar Raman cross sections, the molecular coverage can be easily corrected by adjusting the analyte concentrations. The proper strategy for adjusting the concentrations must be assessed on a case-by-case basis because the molecular properties are dependent upon the bianalyte pair selected. For example, whether the molecules bind kinetically or thermodynamically can influence the procedures necessary for sample preparation (e.g., length of incubation). Once these considerations have been made, a concentration for each analyte can be selected. During sample preparation, it is also very important to follow the dilution procedures described by Darby et al., to avoid non-uniformity in nanoparticle coverage in colloidal solutions.[89] Due to the large number of variables in SMSERS investigations, the experimental details for sample preparation and data collection should always be clearly stated, as these procedures can drastically influence result interpretation.

After completing a bianalyte SERS experiment with a reasonable number of counts, the resulting histogram should be analyzed to determine whether or not the desired threshold for SM detection has been met. This requires estimating the values of α and β for the dataset. For α, there are two defined thresholds for SM detection: 1) when there is on average one molecule per spectrum, and 2) when 95% of an individual analyte's SERS spectra correspond to single molecules (Figure 2.12). For β, a value close to 0.5 is highly

desirable because as the detection probabilities deviate significantly from 0.5, a higher percentage of individual analyte spectra is required to prove SM detection. It should be noted, as the analyte concentrations are lowered to achieve a more rigorous threshold, the probability of locating a SM in a hot spot is also lower. Therefore, the proper threshold for SM detection should be considered on a case-by-case basis. It is critical to find a balance between selecting the most rigorous threshold while still being able to collect a reasonable number of counts. After considering all the above information, if the desired threshold for SM detection has not been met, it may be necessary to further adjust the concentrations. We believe that through careful consideration of the factors stated above, accurate SMSERS can be achieved with bianalyte pairs.

2.4. Conclusion

The data presented above supports five main conclusions. First, we present a new strategy for SMSERS experiments using multiple analytes. This is an essential step towards future experiments in which chemical reactions are measured at the single molecule level and accompanied by rigorous statistical proof. For instance, consider an experiment where isotopologue internal standards for two analytes are used to verify SMSERS, while simultaneously monitoring the chemistry between those analytes. Second, we quantitatively demonstrate the extent to which differences in surface binding affinities and Raman cross sections between analytes can bias the bianalyte approach for proving single molecule detection. Third, a joint Poisson-binomial model is developed to show why the bianalyte approach is compromised and discuss how to avoid these problems. Fourth, a more rigorous threshold for defining SMSERS is presented. The multi-analyte studies

illustrate that spectra with 2 or more molecules contribute non-negligibly to the spectral counts, even when at single molecule coverage. Fifth and finally, we show it is possible in SMSERS to correct for differences in analyte surface binding affinities and Raman cross sections by simply adjusting the concentration ratio between analytes, which has not been previously demonstrated. To our knowledge, we provide the first thorough guidelines for reliably proving SMSERS in future experiments. We believe appropriate implementation of these proofs will greatly advance the field of SMSERS.

CHAPTER 3

SMSERS without Nanogaps

3.1. Introduction

The most commonly utilized nanoparticle substrates for SMSERS are randomly-aggregated colloidal suspensions (e.g., Lee and Meisel Ag Colloids).[19,40,62,96,112,113,122] Even though the SM capability of colloidal suspensions has been well-demonstrated, they are highly polydisperse in nanoparticle size and geometry, as can be visualized in Figure 3.1. Additionally, the salt-induced aggregation of these nanoparticles typically leads to a broad distribution of aggregate sizes, number of members, and interparticle spacings with only a fraction (<1%) of the aggregated nanoparticles being SMSERS-active.[22*]

As the field of SMSERS moves forward, utilizing more reproducible SERS-substrates will allow for the systematic improvement of our fundamental understanding of SERS mechanisms. In addition, it will provide more reliable means of interpreting chemistry at the single molecule level. SERS-substrate improvements have focused heavily on nano-engineering and self-assembly to control the aggregation of nanoparticles and synthesize aggregates with well-defined nanoparticle gaps.[67,71–74,82,127–130] Several of these attempts explored the use of nanoparticle dimers, which in principle provide a consistent and controllable EF.[71,73,127–129] Other avenues of nanoparticle fabrication, however, remain underutilized. One notable exception is an optical nanoantenna chip shown to be capable

*This Chapter is reproduced with permission from reference [52]. Copyright 2013 American Chemical Society.

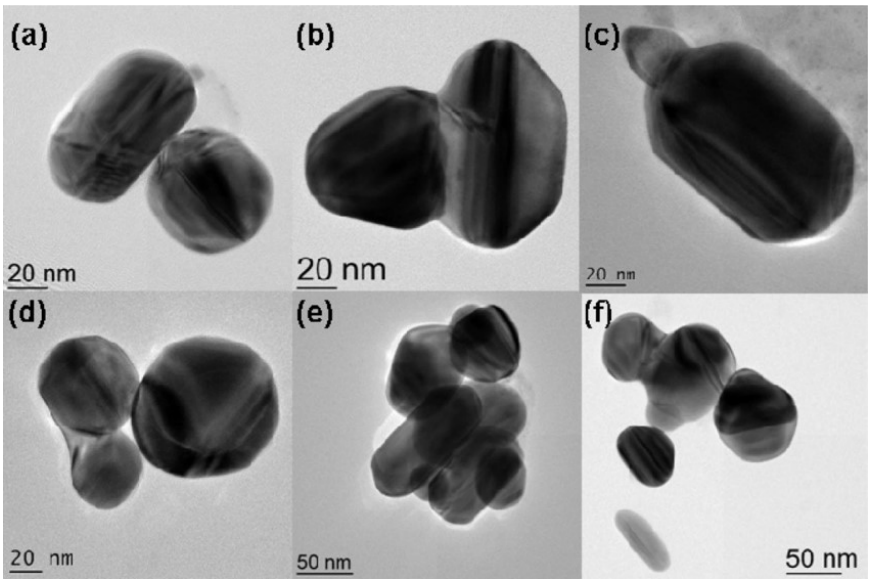

Figure 3.1. HRTEM images of SMSERS-active Ag Colloids aggregated with ∼10 mM NaCl. Adapted with permission from reference [22]. Copyright 2008 American Chemical Society.

of SMSERS by Wang and coworkers.[68] The nanoantenna chip provided excellent control over hot spot position and has reported EFs of up to $\sim 10^{13}$ due to the combination of an optimized local EM field enhancement (10^{11}) and antenna directionality (10^{2}).[67,68] The nanoantenna fabrication, however, is complicated and costly. The multi-step, top-down fabrication requires electron beam lithography and alignment with nanoscale precision.

A well characterized approach for fabricating reproducible SERS-active nanoparticles is nanosphere lithography (NSL).[46,48–51,69,70,131] NSL is a high-throughput technique that creates large arrays of triangular nanoparticles which are inherently similar in shape and size. The nanofabrication of NSL nanoparticles is straightforward and simple, involving three main steps (Figure 3.2): 1) self-assembly of polystyrene (PS) spheres into a close-packed monolayer on a cleaned and base treated glass surface, 2) thermal deposition of

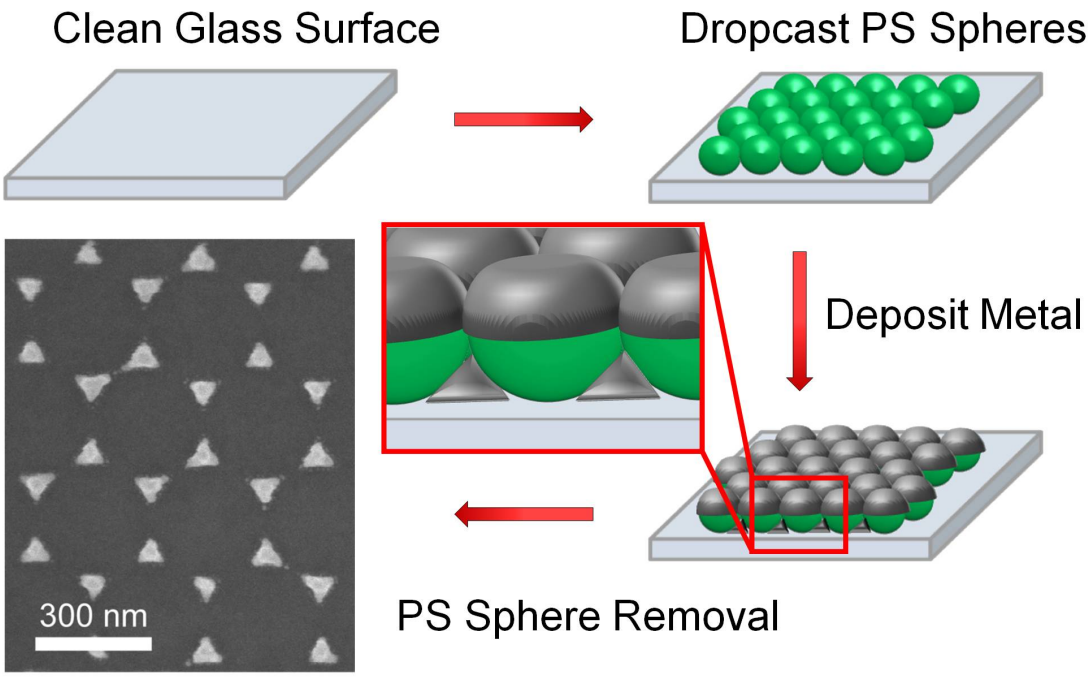

Figure 3.2. The fabrication of nanoparticles by nanosphere lithography involves 3 steps: 1) self-assembly of PS spheres into a monolayer on a clean and base treated glass surface, 2) thermal deposition of metal, and 3) removal of PS spheres via tape stripping and sonication in ethanol. Triangular nanoparticles are formed in the interstitial sites of the hexagonally-packed sphere monolayer.

metal, and 3) removal of PS spheres via tape stripping and sonication in ethanol. By altering the PS sphere size and thickness of the metal deposited, the size and aspect ratio of the resulting nanoparticles can be varied, allowing systematic control of the substrate LSPR. In addition, these nanoparticles have been shown previously to be capable of supporting EFs of $\sim 10^8$, but are more typically on the order of $\sim 10^7$ in the spectral window used in this experiment.[46] In 2010, a single spectrum of R6G was collected from

NSL-derived nanoparticles suggesting SM capability.[131] At the time, however, it was not conclusively proven. In this study, we characterized the NSL-derived nanoparticles by SEM to confirm their geometry and interparticle spacing. Then, we used the isotopologue approach to conclusively prove SM sensitivity for the individual nanoparticles.

3.2. Experimental Methods

3.2.1. Preparation of NSL-derived Nanopyramids

The NSL-derived nanopyramids were prepared on pretreated glass coverslips (25 mm, #1.5) using piranha etch (3:1 H_2SO_4 /30% H_2O_2) followed by base treatment (5:1:1 H_20 /NH_4OH /30% H_20_2) with sonication for 1 hour to render the surface clean and hydrophilic, respectively.[48] After pretreatment, 4-6 μL of 4% wt 290 nm PS spheres (Thermo Fisher) were dropcast onto the glass coverslips. The substrates were allowed to dry in ambient conditions to form large areas of hexagonally close-packed monolayers on the surface of the glass. Using a thermal evaporator (Kurt J. Lesker PVD 75), a 45 nm film of Ag was deposited on the substrates at 1 Å/s and at pressure of $\sim 10^{-7}$ Torr. The spheres were removed from the glass surface via tape stripping and ethanol sonication for $\sim$5 sec, leaving behind a uniform array of nanopyramids. Before SMSERS measurements were performed, equal molar amounts of R6G-d_0 and R6G-d_4 were dissolved in Millipore (18.2 MΩ·cm) for a final concentration of 1 x 10^{-8} M. Then, 20 μL was spun coat onto the substrate at 1000 rpm for 1 min followed by an additional 2000 rpm for 2 min to ensure complete evaporation of the solution. All samples were used within one day of preparation.

3.2.2. Instrumentation

The SERS measurements were collected on an inverted microscope (Nikon TE300) with an oil immersion objective (Nikon, 100×, NA = 0.5-1.3) with the NA set at 1.0. The signal was collected in a backscattering geometry after which the Rayleigh scattering is filtered with a long-pass filter (Semrock, LP03-532RS-25). The collected signal was analyzed with a 1200 grooves/mm grating and LN_2-cooled CCD (Action 300i, Spec-10 400B). The excitation wavelength was 532 nm (Spectra-Physics, Millenia X) with a power range of 115-205 μW measured at the sample and a spot size of approximately 1 μm^2. All samples were placed in a custom-built flow cell and immersed in a dry N_2 atmosphere. The surfaces of the substrates were scanned using a piezo stage (E-710 Digital PZT) with a step size of 2 μm in the x- and y- directions. The spectra were collected for 1 sec.

3.2.3. SEM Images

SEM imaging was performed on a LEO Gemini 1525 microscope operating at 3 kV. Samples were observed at normal incidence. Cross section imaging was done by mounting the sample on a 90 degree sample holder.

3.3. Results and Discussion

3.3.1. Characterization of Nanopyramids

For the NSL-prepared nanoparticles in this study, the LSPR lambda max (λ_{max}) was approximately 546 nm which was red-shifted from the excitation source of 532 nm to provide optimal enhancement of the incident and Raman scattered photons, while also remaining close to the absorption maximum (λ_{max} = 527 nm) of the R6G isotopologues

used to prove SM sensitivity.[46] The LSPR spectrum of a NSL substrate and the absorption of R6G are shown Figure 3.3.

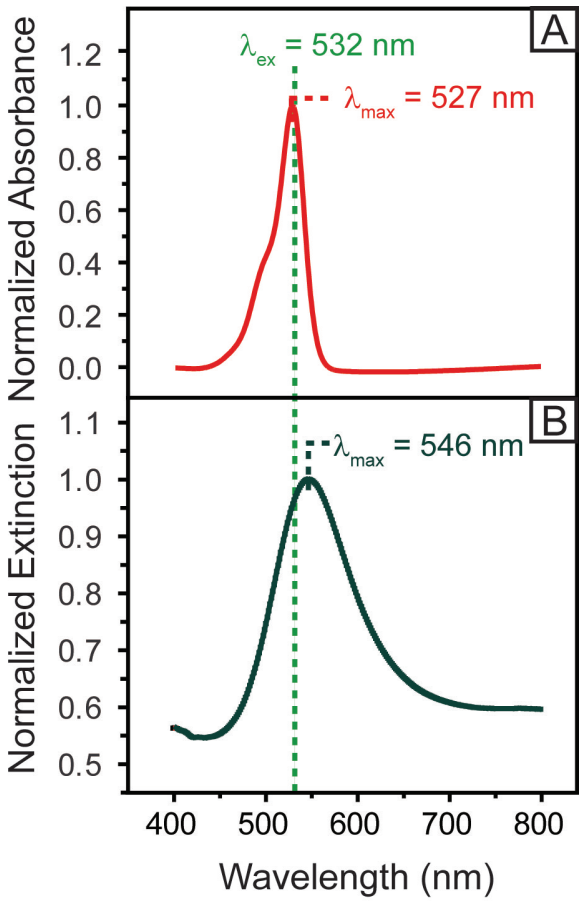

Figure 3.3. A) Absorption spectrum of R6G with a λ_{max} = 527 nm. B) LSPR spectrum of NSL-derived nanoparticles prepared by nanosphere lithography with 290 nm PS spheres and 45 nm Ag deposited with a λ_{max} = 546 nm. The excitation line used for the SMSERS experiment is indicated at 532 nm.

Figure 3.4 presents the structural characterization of NSL-derived nanoparticles fabricated on a silicon substrate by SEM. Based on geometric calculations for a hexagonally

close-packed monolayer of spheres, the relationship between PS sphere diameter (D) and inter-particle distances (d_{ip}) for NSL-derived nanoparticles is expressed as follows:[48]

$$d_{ip} = \frac{1}{\sqrt{3}} D \tag{3.1}$$

Based on Equation 3.1 for a D = 290 nm the d_{ip} = 167 nm. As determined between 50 triangular nanoparticles in the SEM images, the experimental d_{ip} = 168 ± 7 nm is in close agreement with the expected results. In the top-down view (Figure 3.4), the triangular shape of the nanoparticles and their tip-to-tip orientation is clearly observed. While some variation in the sharpness of the tips is seen, there is a large gap between the nanoparticles isolating them from strong electromagnetic coupling.[48,69,70] As indicated previously by DDA simulations on similarly shaped nanoparticles, the enhanced EM fields are concentrated at the tips of individual triangular nanoparticles with EFs as high as 10^8.[69,70] Figure 3.4B shows a cross-sectional view of the nanoparticles with a height of 42 ± 7 nm, determined from 34 nanoparticles, consistent with the amount of Ag deposited. To our knowledge, this is the first cross-section of NSL-derived nanoparticles. Based on a previous NSL paper, the speculated geometry of the Ag nanoparticles was a truncated tetrahedron.[50] Figure 3.4B confirms this geometry provided an accurate description of the fabricated nanoparticles with the observation of non-parallel sides and truncated top. For simplicity, we refer to the shape of the nanoparticles as nanopyramids.

Figure 3.4C shows a histogram tabulating 470 tip-to-tip distances (d_{tt}) of NSL-derived nanopyramids with an average d_{tt} of 83 ± 20 nm. Departure from ideal packing, leading to minor deviation of d_{tt} is believed to result from small variations in the PS sphere size. The predominance of the relatively large distances observed, however, between nanoparticles

indicates that the SM sensitivity is likely the result of individual nanopyramids where the highest enhancement has been shown with DDA calculations to occur at the tips.[69,70] Additionally, it is possible that surface roughness on the individual nanopyramids may contribute to SM sensitivity.

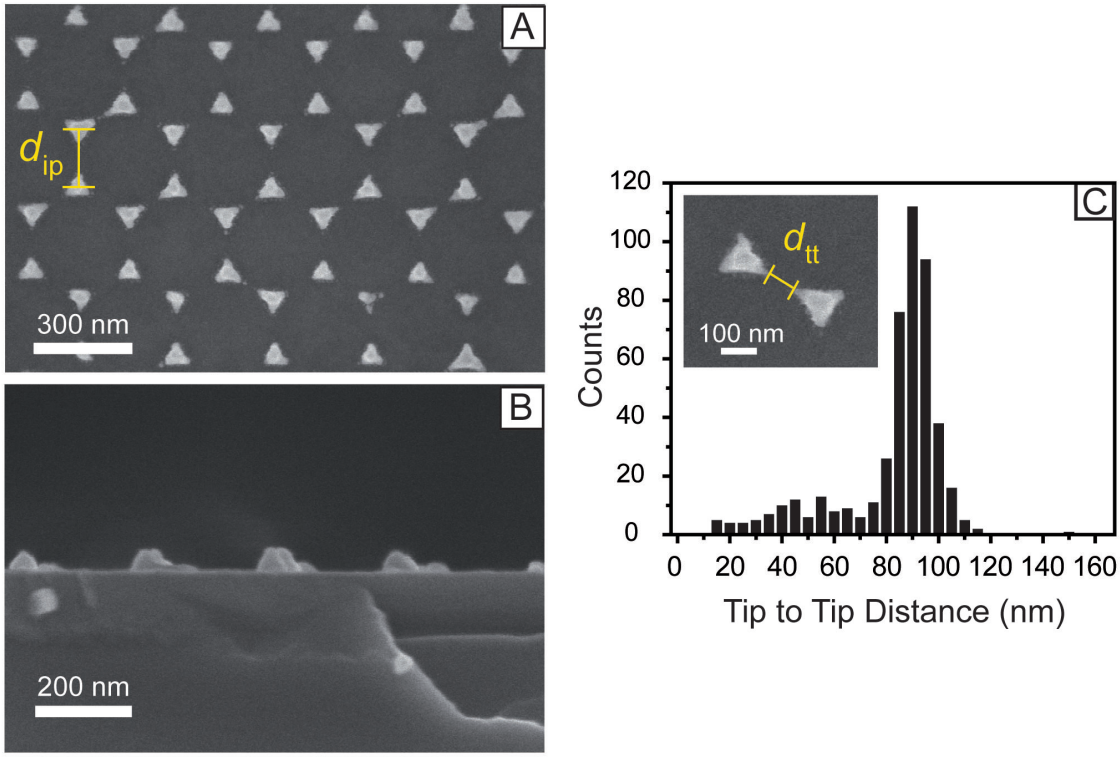

Figure 3.4. SEM images of Ag nanopyramids fabricated on a silicon substrate with 290 nm PS spheres and 45 nm Ag film in A) top-down view and B) cross-sectional view. The d_{ip} as indicated in A was measured between 50 nanopyramids (168 ± 7 nm). Nanopyramid height was determined from the cross-section of 34 nanoparticles (42 ± 7 nm) in B. C) Histogram tabulating 470 d_{tt} as indicated in C from the SEM images with an average distance of 83 ± 20 nm.

3.3.2. SMSERS on Nanopyramids

The isotopologue method was used to prove SM detection with the NSL-derived nanopyramids.[40,57] Specifically in this experiment, 20 μL of 1x10^{-8} M solution containing equal molar amounts R6G-d_0 and R6G-d_4 was applied to the substrates via spin coating. Assuming the entirety of the 20 μL aliquot is evenly dispersed on a 25 mm coverslip, the corresponding surface coverage would be 244 molecules/μm^2. The majority of the substrate surface, however, is glass with a nanoparticle surface coverage of only 7.2%.[48] Taking into account this surface coverage and that a typical 1 μm^2 area has $\sim$32 nanopyramids, as determined from the SEM images, there is $<$1 molecule per nanoparticle.

The substrates were scanned with a 2 μm step size in the x- and y-directions to limit sample degradation while collecting the SMSERS signal. The peak of interest for distinguishing the identity of R6G-d_0 is 610 cm^{-1} which differs from the 601 cm^{-1} and 638 cm^{-1} peaks of R6G-d_4.[40] The identification of predominately only one isotopologue in a spectrum versus the identification of both when at equal molar concentrations on the substrate surface was used to prove SM detection based on a Poisson-binomial distribution as described previously.[40,57] Figure 3.5A shows representative spectra of R6G-d_0 and R6G-d_4 collected from the NSL substrates indicated by the presence of the 610 cm^{-1} peak in the red spectrum and the 601 cm^{-1} and 638 cm^{-1} peaks in the blue spectrum, respectively. In both cases the peaks of the other isotopologue were not present indicating SM character. Molecules residing on the glass surface between nanoparticles contributed to a fluorescence background as seen in Figure 3.5B. The identification of SMSERS signal in the presence of fluorescence demonstrates the incredible level of enhancement produced by the NSL-derived nanopyramids.

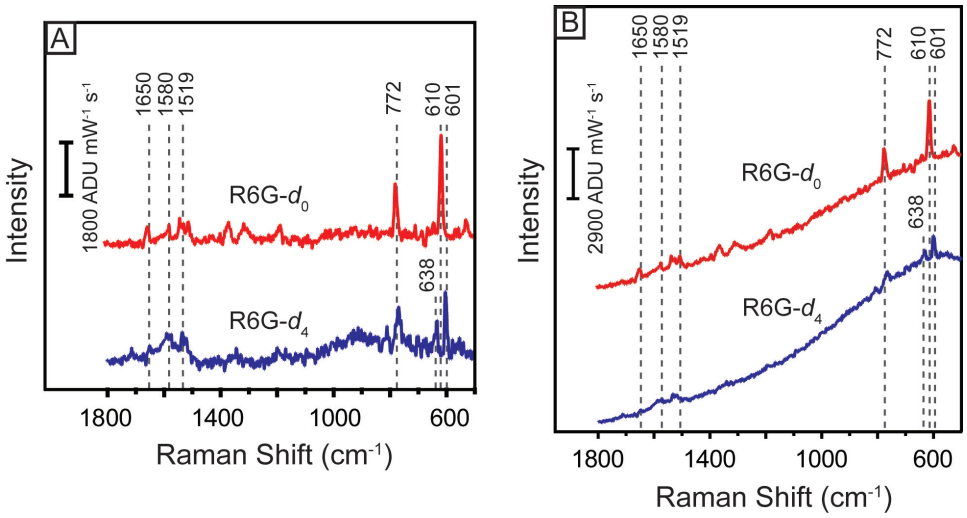

Figure 3.5. A) Representative SM spectra of R6G-d_0 and R6G-d_4 collected from NSL-derived nanopyramids. The blue spectrum indicates the presence of R6G-d_4 by the observance of the 601 cm^{-1} and 638 cm^{-1} peaks. The red spectrum indicates the presence of R6G-d_0 by the observance of the 610 cm^{-1} peak. Spectra were collected with λ_{ex} = 532 nm, t_{aq} = 1 sec, and P_{ex} = 205 μW and were background corrected for fluorescence due to molecules located on the glass surface between nanopyramids. B) The spectra from A showing fluorescence background.

The spectra can be categorized into three types: only R6G-d_0, only R6G-d_4, or both R6G-d_0 and R6G-d_4. Representative spectra of the three possible events are included in Figure 3.6 showing only the low-frequency region. These spectra were also background corrected for fluorescence. The red spectrum shows only the presence of R6G-d_0 (610 cm^{-1}), the blue spectrum shows only R6G-d_4 (601 cm^{-1} and 638 cm^{-1}), and the green

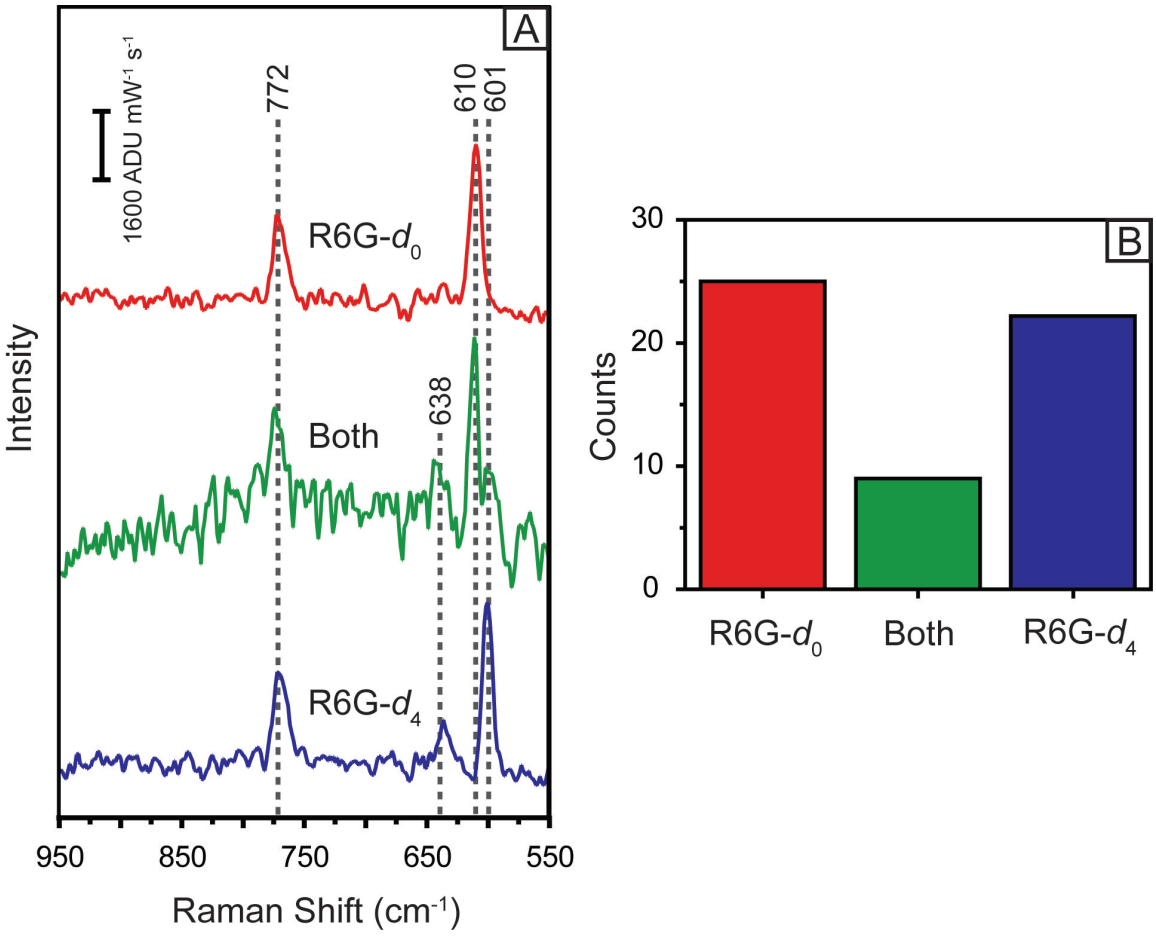

Figure 3.6. A) Magnification of the low-frequency region of the three possible events which are 1) R6G-d_0, 2) R6G-d_4, or 3) both R6G-d_0 and R6G-d_4 collected from NSL-derived nanopyramids with $\lambda_{ex} = 532$ nm, $t_{aq} = 1$ sec, and $P_{ex} = 205$ μW. The spectra were background corrected for fluorescence due to molecules located on the glass surface between nanopyramids. B) Histogram displaying the occurrence of each event as determined by the 600 cm^{-1} region. Preferential observation of only one isotopologue versus both indicated SM detection.

spectrum shows both R6G-d_0 and R6G-d_4 as indicated by the presence of all the characteristic peaks (610 cm^{-1}, 601 cm^{-1}, and 638 cm^{-1}). All three types of events share the 772 cm^{-1} peak which remains unaltered by deuteration of R6G.

The number of instances of each event as identified by the 600 cm^{-1} region is tabulated in Figure 3.6B. The total number of events was 56 with 47 demonstrating the presence of only R6G-d_0 or R6G-d_4, but not both. The mixed events were 9 of the total 56. The ratio of R6G-d_0-only: both: R6G-d_4-only is 25:9:22 which simplifies to 2.8:1:2.4. Based on the joint Poisson-binomial model discussed in Chapter 2 with $\beta = 0.5$ (i.e., 50:50 probability of detecting either R6G-d_0 or R6G-d_4) and an $\alpha = 1$ (i.e., on average 1 molecule detected per spectrum) the probabilities are 2.5:1:2.5, which is in close agreement with the results.[40,57] Molecules residing on the glass surface between the nanoparticles or on regions of the nanoparticles with insufficient enhancement for SM detection are not accounted for in the Poisson-binomial model and may lead to deviation from ideal statistics. However, the preferential occurrence of events with primarily individual isotopologue character proves the observation of SMSERS with NSL-derived nanopyramids.

The results presented in this Chapter indicate that SMSERS of R6G was from individual Ag nanopyramids. Previous electrodynamic calculations on NSL-derived nanostructures indicate that the highest EM fields, capable of supporting SM detection, occur at the nanoparticle tips.[69,70] Furthermore, unlike traditional aggregated colloidal suspensions with <2 nm nanogaps, the average measured d_{tt} in our system was 83 $\pm$ 20 nm. While defects are observed for a few nanopyramids, like the deformed particle in the lower right corner of Figure 3.4A, the occurrence of these defects is low compared to the number of SM events. Ultimately, the previous simulations and lack of nm-scale gaps

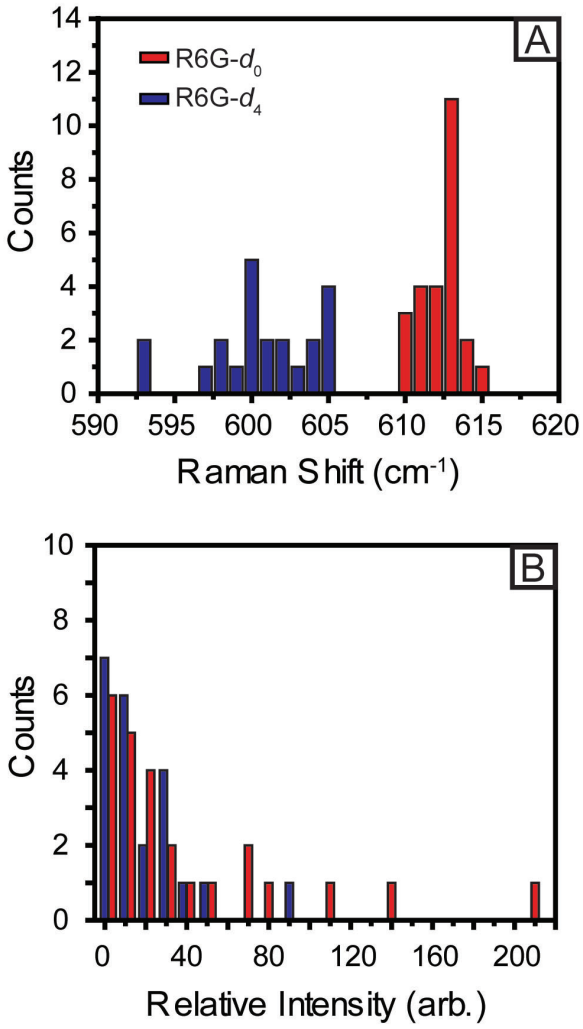

Figure 3.7. A) Histogram of the low-frequency peak location for events indicating SM character of R6G-d_0 and R6G-d_4, illustrating the degree of spectral wandering observed for different sites. B) Histogram of the characteristic peak intensities from events indicating SM character of R6G-d_0 and R6G-d_4, illustrating the large degree of intensity variation seen between different sites of up to 2 orders of magnitude. R6G-d_0 (red data), and R6G-d_4 (blue data).

corroborates that the SMSERS signal originates from SMs located at the nanopyramide tips. Our experiment alone, however, does not rule out the possibility of other sites or provide conclusive proof of the specific locations of the SMs on the nanopyramids.

Figure 3.7A is a histogram tabulating the peak frequencies for individual SM events of R6G-d_0 (red) and R6G-d_4 (blue). No frequency shifts were observed for the 772 cm^{-1} peak indicating the shifts in the 600 cm^{-1} region resulted from the presence of one isotopologue or the other. Additionally, Figure 3.7B shows the dramatic intensity fluctuations observed for the SM events of R6G-d_0 and R6G-d_4, spanning 2 orders of magnitude. The large intensity fluctuations are consistent with diverse molecular location around the nanoparticle tip, which has a large curvature compared to the molecule size. Tip rounding likely plays a large role in the intensity distribution of Figure 3.7B as well.

3.4. Conclusion

NSL-derived nanopyramids achieve SMSERS without nanogaps, as demonstrated by the results presented in this Chapter. Due to the large tip-to-tip interparticle distances and through earlier electrodynamic calculations,[69,70] it is proposed that the SMSERS events arise at single nanopyramid tips. We also show the first cross-sectional SEM image of nanopyramid arrays prepared via NSL verifying their geometry as a truncated tetrahedron. NSL substrates are universally available due to their simple fabrication process, large useable array area, and reproducibility. Furthermore, their tunable LSPR makes them versatile for different excitation wavelengths and amenable to the resonance Raman conditions of various analytes of interest.

CHAPTER 4

Evaluating Single Molecule Stokes and Anti-Stokes SERS for Nanoscale Thermometry

4.1. Introduction

In the field of plasmonics, local heating is an important consideration for many diverse applications ranging from optoelectronics to biomedical technology.[132–134] In many instances local heating is beneficial, such as for heat-mediated catalysis[135] or device nanofabrication.[136] In other cases, heating may cause unwelcomed physical or chemical changes (e.g., analyte degradation). Various methodologies have been developed to measure local temperatures ranging from scanning thermal microscopy[137] to fluorescent nanoprobes.[138] For example, Gao and Bando developed a nanoscopic analogue to the conventional mercury thermometer via a gallium-filled carbon nanotube,[139] Millen et al. exploited the non-equilibrium Brownian dynamics of a nanosphere to extract local temperatures,[140] and Mecklenburg et al. extracted nanoscale temperatures by mapping density gradients in aluminum wires using scanning transmission electron microscopy and electron energy loss spectroscopy.[141] Unfortunately, these methods perturb the temperature of the nanoscale system under study, require particular environments (e.g., high vacuum), and/or cannot achieve spatial resolution on the order of 1 nm.*

*This Chapter is reproduced with permission from reference [116]. Copyright 2015 American Chemical Society.

Raman spectroscopy allows for temperature measurements because the anti-Stokes and Stokes intensities are proportional to the populations of their respective initial vibrational states, which are described by the Boltzmann distribution. Therefore, SERS, particularly with SM sensitivity, has the potential to act as a nanoscale temperature probe. Implementation of this method, however, requires elucidation of the complex contributions to the ratio (ρ) of the anti-Stokes (aS) to Stokes (S) SERS intensity (I). The contributions to ρ are governed by Equation 1:[142]

$$\rho = \frac{I_{aS}}{I_S} = A \left[\frac{\tau \sigma'_S I_L}{h\nu_L} + e^{-\frac{hv_m}{k_B T}} \right] \tag{4.1}$$

for a Raman mode of shift frequency ν_{m}, where τ represents the vibrational excited state lifetime, σ' denotes the Raman cross section (see below), T is the local temperature, and a subscript L signifies the laser excitation. The first and second terms in the bracket describe vibrational pumping and thermal population, respectively. The asymmetry factor, A, is given by:

$$A = \frac{\eta_{aS}}{\eta_S} \cdot \frac{\sigma'_{aS}}{\sigma'_S} \cdot \left| \frac{E_L E_{aS}}{E_L E_S} \right|^2 \tag{4.2}$$

where η is defined as the wavelength-dependent detection efficiency of unpolarized light,[143] and E represents the local, wavelength-dependent electric field strength. For photon counting systems (e.g., charge-coupled devices), the nonresonant Raman cross section is described by:[144,145]

$$\sigma' = \sigma^0_m \nu_L (\nu_L \pm \nu_m)^3 \tag{4.3}$$

for both the anti-Stokes and Stokes transitions. σ^0 is then the wavelength-independent Raman cross section. In the case of a resonant analyte, asymmetry in the resonance Raman cross section must be taken into account.[146]

The complexity of factors contributing to ρ has led to controversy in the field, with many debating the extent of contributions from vibrational pumping and thermal population upon laser excitation.[117,142,147–150] Even the existence of vibrational pumping in SERS has undergone intense scrutiny. Reports have suggested that the anomalously high measured ρ values may arise solely from resonance effects unevenly enhancing the Stokes and anti-Stokes bands.[148,149] Tackling the complexity of ρ has involved finding ways to isolate the various contributing factors. Maher et al., for example, used temperature scans to separate the contributions of resonance effects from heating and pumping in ρ.[150] Other studies by Etchegoin and coworkers used SMSERS to probe the contributions of vibrational pumping and heating.[117,118,151] Conclusive proof of anti-Stokes SMSERS, however, has not yet been provided. Furthermore in these studies, the authors observed large variations in ρ and demonstrated that multiple factors, including electromagnetic and thermal mechanisms, contribute to the variance.

Building off this existing work, we utilize SERS at the single-aggregate and single molecule limits in the context of recent advances in our lab to assess the feasibility of SERS as a nanoscale temperature probe. R6G is an ideal analyte because of its extensive characterization in the literature. First, we conclusively verify SM sensitivity in anti-Stokes SERS of R6G on aggregated Ag nanoparticles. Subsequently, we provide a detailed analysis of the distribution of ρ across many events in SMSERS and in high-coverage, single-aggregate SERS. This analysis includes a detailed discussion of the factors contributing

to ρ along with accompanying electrodynamics simulations. Lastly, we outline the circumstances required for accurate temperature measurements using SERS. Overall, the results of this study can be used as a model for future temperature measurements in plasmonic nanocavities via SERS.

4.2. Experimental and Theoretical Methods

4.2.1. Ag Nanoparticle Synthesis

All glassware was cleaned with aqua regia (3:1 HCl/HNO_3) and dried in an oven prior to the nanoparticle synthesis. Following the procedure developed by Lee and Meisel,[152] 90 mg of silver nitrate ($AgNO_3$) was dissolved in 500 mL of Milipore water (18.2 MΩ·cm) in a 1 L volumetric flask. While rapidly stirring, the solution was brought to a vigorous boil. Then 10 mL of 1% sodium citrate was added. The solution boiled for 30 min during which its color transitioned from transparent yellow to brown to opaque gray-green. The solution was allowed to cool to room temperature before storage in a brown glass bottle. The chemically synthesized nanoparticles were used within 1 week of their preparation.

4.2.2. Sample Preparation

The SMSERS samples were prepared by adding 100 μL of a mixture of 5×10^{-10} M R6G-d_0 and R6G-d_4 each (total dye concentration 1×10^{-9} M) to 1 mL of the synthesized Ag nanoparticle solution while stirring. Then 1 mL of 40 mM NaCl was added to aggregate the nanoparticles. The solution was allowed to aggregate for 1 day prior to dropcasting but can remain SMSERS-active up to 4 days after aggregation. On base-treated (5:1:1 H_2O /NH_4OH /30% H_2O_2) glass coverslips (25 mm, #1.5), 100 μL of the aggregated

nanoparticle solution was dropcast and dried under a flow of N_2. This step was repeated once (total dropcast volume 200 μL) to ensure adequate nanoparticle coverage.

High adsorbate coverage samples were prepared by adding 50 μL of 1×10^{-6} M R6G-d_0 to 1 mL of Ag nanoparticles. At high dye coverage, a smaller volume (500 μL) of 20 mM NaCl was used for aggregation to prevent the nanoparticles from precipitating out of solution. The nanoparticles aggregated for 1 day prior to dropcasting. To allow for the collection of SERS signal from individual aggregates, only 20 μL of the aggregated nanoparticle solution was dropcast on the coverslip and dried with N_2. This step was repeated once for a total volume of 40 μL. These samples will be refereed to as single-aggregate SERS (SASERS).

4.2.3. SERS Instrumentation

To limit photodegradation, both the SMSERS and SASERS substrates were placed in a custom-built flow cell under a positive pressure of N_2 for a minimum of 2 hours prior to irradiation. The SERS measurements were collected on an inverted microscope (Nikon Eclipse Ti2000-U) with a 100× oil immersion objective with the numerical aperture (NA) set to 0.9 (Nikon, NA = 0.5-1.3). 532 nm excitation (Spectra-Physics, Millenia XV) irradiated the sample at a grazing incidence angle of 30 degrees with a spot size of approximately 0.25 mm^2.

During alignment, a long-pass filter (Semrock, LP03-532RS-25) was placed in the microscope to filter out the excitation and Rayleigh scattered light to allow visual observation of the Raman scattering through the microscope eyepieces. After visually locating and centering a SERS-active particle on the entrance slit of the spectrograph (Princeton

Instruments Acton SpectraPro 2300i), the signal was dispersed by a 1200 grooves/mm grating and detected by a LN_2-cooled CCD (Princeton Instruments Spec-10:400BR). The long pass filter was removed from the microscope, and three angle-tuned volumetric Bragg grating notch filters in series (BragGrate, OptiGrate Corp.) placed in the collection path attenuated reflected and Rayleigh scattered laser light, making possible simultaneous collection of Stokes and anti-Stokes SER scattering without saturating the detector at λ_{ex}.

The microscope was set up in a confocal geometry, with a 200 μm pinhole positioned at the output of the microscope to isolate the aggregate of interest on the CCD. A broadband depolarizer was placed in the collection path to remove bias from varying polarizations of scattered light from the different aggregates. The SMSERS spectra were collected with 59 mW (P_{ex} = 24 W/cm^2) for an acquisition time (t_{aq}) of 2 sec with up to 60 accumulations depending on particle lifetime. The SASERS spectra were collected under identical conditions for t_{aq} = 2 sec with 15 accumulations.

For the power dependence studies, a single SERS-active aggregate was exposed to 11 excitation powers across a range of 2-178 mW for t_{aq} = 2 sec with 15 accumulations at each power. For the dark-field scattering correlated studies, the microscope was equipped with a dry dark-field condenser (Nikon, NA = 0.8-0.95). Immediately after collecting SERS, the 100× objective NA was set to 0.7, and a 150 grooves/mm grating dispersed the dark-field scattering onto the CCD for collection.

4.2.4. Theoretical Approach

Simulations have been performed using the finite-difference time-domain (FDTD Lumerical Solutions, 8.11.318) method to calculate the far field (scattering cross section) and

near field (enhancement factor) properties of the Ag nanoparticle aggregates. The Ag dielectric function from Palik[153] was used for the nanoparticles and a refractive index of 1 was used for the background medium. The simulation region is delimited by perfectly matched layer absorbing boundaries on all axes. The geometric parameters used for the Ag trimer were extracted from an experimental TEM image from reference [22], which depicts aggregates prepared using the same approach utilized in this report. The spherical nanoparticles of the trimer were 100 and 50 nm in diameter, respectively. The elliptical Ag particle was 40 nm (long axis) and 33.3 nm (short axes) in diameter. The small structural details and numerical convergence of the results require a spatial meshgrid of 1 nm on the particles and 0.25 nm in each gap between two adjacent nanoparticles. A 2D frequency-domain field monitor was located at z = 25 nm to record data from the simulation. Plane-wave irradiation was incident normal to the field monitor with polarization 45 degrees rotated counterclockwise from vertical. Additionally, a power monitor was added in the simulation region to calculate the scattering cross section of the aggregate. Far field scattering cross section and near field enhancement distribution $|E/E_0|$ were calculated at wavelengths ranging from 400 to 675 nm.

4.3. Results and Discussion

4.3.1. Verification of Anti-Stokes SMSERS Detection

We have rigorously verified detection of single molecules via anti-Stokes SERS using the isotopologue method.[40] This approach is a refinement of the bianalyte method,[96] as it removes the uncertainty caused by differing adsorption behavior and Raman cross sections. Ag nanoparticle aggregates dosed with equimolar amounts of R6G-d_0 and R6G-d_4 were

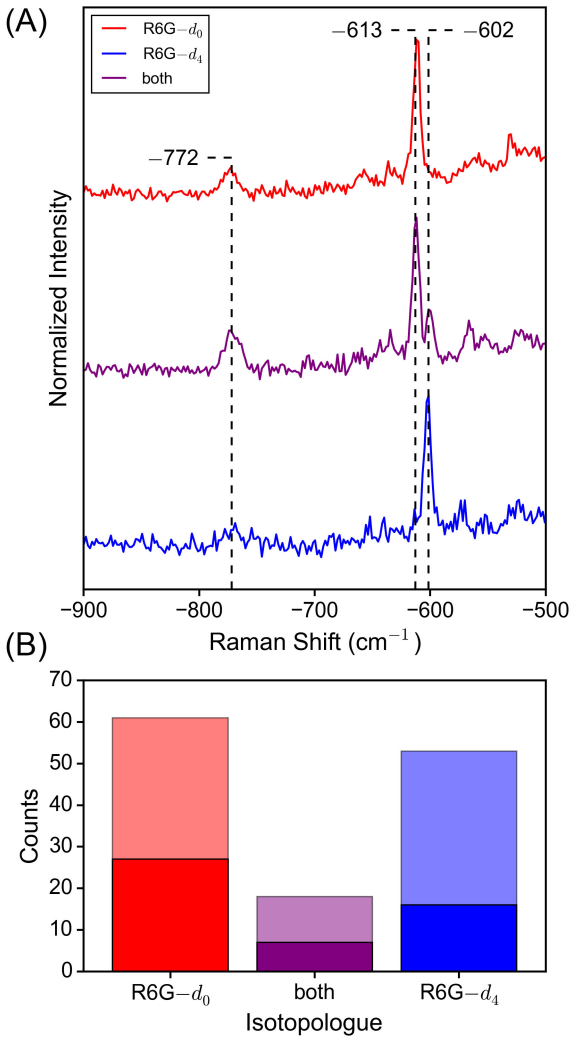

Figure 4.1. A) Anti-Stokes SMSERS spectra exhibiting one or both isotopologues of R6G. R6G has an isotopically sensitive phenyl band at 613 cm^{-1} (R6G-d_0) that shifts to 602 cm^{-1} (R6G-d_4) upon deuteration. B) Histogram of SM events as distinguished by the isotopically sensitive mode, where faded bars represent total events and vibrant bars represent anti-Stokes events.

interrogated using SERS on both sides of the laser line simultaneously (λ_{ex} = 532 nm). R6G has a sharp, strong, and isotopically sensitive phenyl band at ca. 613 cm^{-1} that shifts to ca. 602 cm^{-1} upon deuteration of its phenyl moiety. This band was observed in both Stokes and anti-Stokes SMSERS. Representative anti-Stokes SERS spectra showing the character of one or both isotopologues collected at SM coverage can be visualized in Figure 4.1A. In the spectral window observed, the isotopically sensitive mode and the 772 cm^{-1} mode are visible.

The histogram of SM events is depicted in Figure 4.1B. It separates the events displaying single isotopologue character from those displaying character of both isotopologues. Of the 132 total events, 114 display character of only one isotopologue. As a consequence of the wide distribution in SERS intensity across SM events (Figure 4.2), anti-Stokes scattering from many of the aggregates was too weak to be measured. Of the resulting 50 spectra displaying appreciable R6G anti-Stokes SMSER signal intensity, 43 events exhibit character from only one isotopologue.

Our histogram closely resembles previous reports of SM detection.[19,40,52,154] Importantly, the events represent a Poisson-binomial distribution of R6G-d_0 and -d_4 coverage, in which the probability of observing n_1 R6G-d_0 molecules and n_2 R6G-d_4 molecules in a single event is given by Equation 2.1. Assuming $\beta = 0.5$ for the isotopologues, $\alpha = 0.564$, meaning less than one probed molecule per nanoparticle aggregate. The calculated R6G-d_0:both:R6G-d_4 probability of 3.07:1:3.07 closely matches our observed anti-Stokes SMSERS counts (3.86:1:2.29). This model considers up to five copies of each isotopologue contributing to the SER signal in each event, which represents 99.99% of the expected

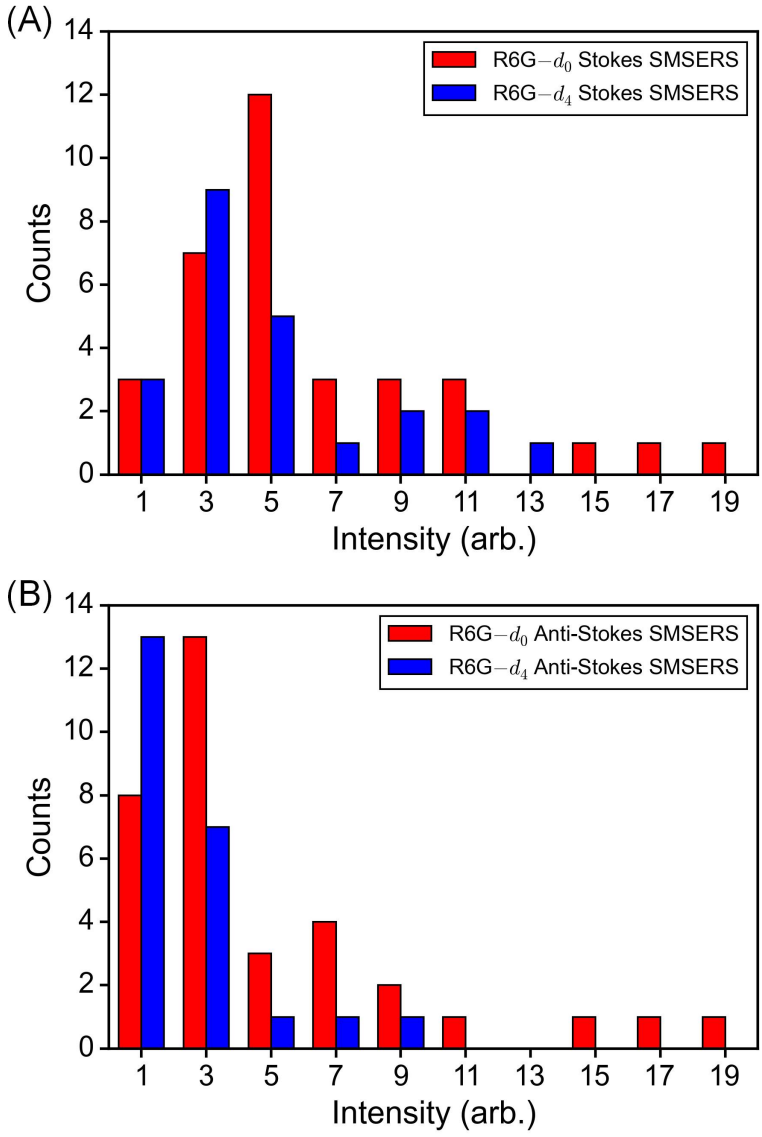

Figure 4.2. The intensity distributions for the A) Stokes and B) anti-Stokes SMSERS events. The intensities vary by over an order of magnitude for the SM events.

events at this value of α. Following this model, 87% of the anti-Stokes events (equivalently, 37 spectra) displaying single isotopologue character are expected to be true SM

events. Our observations provide the first thorough statistical analysis of single molecule sensitivity in spontaneous anti-Stokes SERS.

4.3.2. Distribution of ρ in SMSERS and SASERS

All spectra were individually fit with Gaussians, and their integrated intensities were utilized to calculate ρ. We presume that Gaussian lineshapes were observed instead of the expected Lorentzian lineshapes because the bands are narrower than our instrumental response and therefore suffer from artificial broadening. To quantify the extent to which the anti-Stokes and Stokes intensities are correlated, we calculated their statistical correlation. The statistical correlation, χ, between two variables a and b is given by:

$$\chi(a,b) = \frac{cov_{ab}}{\sqrt{cov_{aa}}\sqrt{cov_{bb}}} \tag{4.4}$$

where cov_{ab} denotes the covariance between a and b across all spectra n and is defined as:

$$cov_{ab} = \sum_{i=1}^{n}[I_{a,i} - \bar{I}_a][I_{b,i} - \bar{I}_b] \tag{4.5}$$

Computed χ values lie within the range [-1,1], where $\chi = 1$ denotes perfectly correlated variables, $\chi =$ -1 denotes perfectly anti-correlated variables, and $\chi = 0$ denotes variables that are not correlated. Values in between indicate partial correlation or partial anti-correlation. If we apply this analysis to the integrated anti-Stokes and Stokes intensities plotted in Figure 4.3A, we find $\chi_{SM} = 0.42$ for SMSERS and $\chi_{SA}= 0.37$ for SASERS. Consistent with the notion that a stronger EM near field will produce a stronger overall SER signal (both Stokes and anti-Stokes), this value is positive. The values, however, are far from perfectly correlated. Interestingly, we find a large variance in ρ across more than

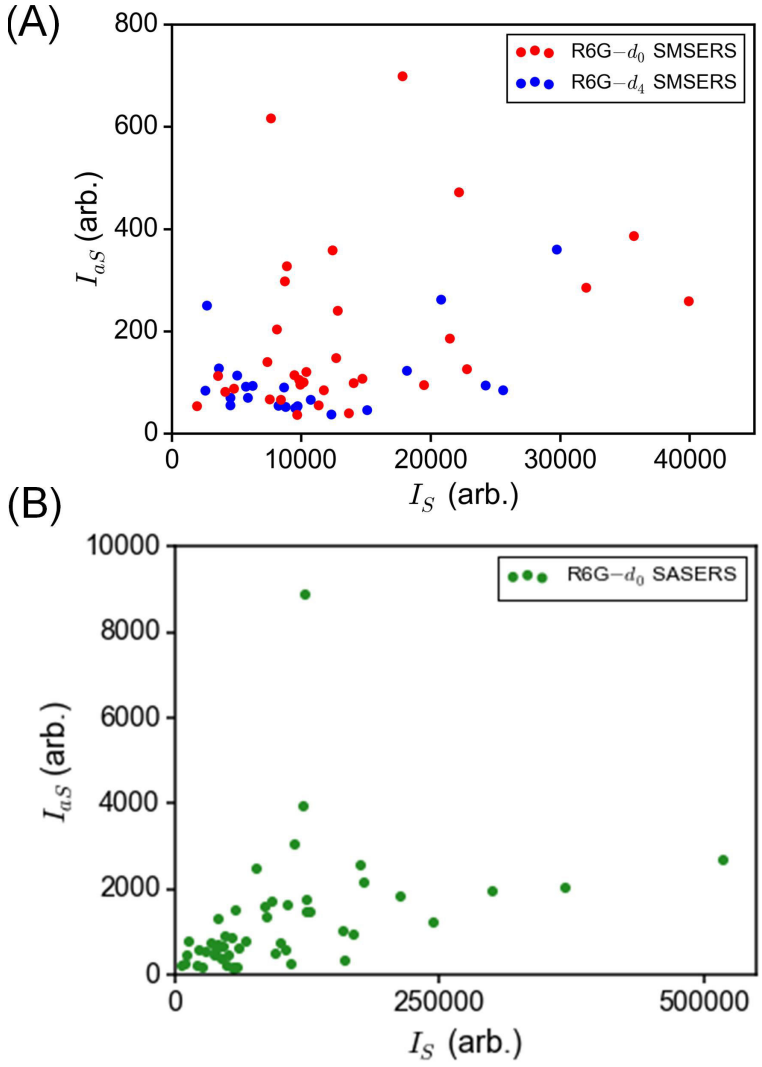

Figure 4.3. Statistical correlations between Stokes (S) and anti-Stokes (aS) intensities for A) SMSERS (χ_{SM}= 0.42) and B) high-coverage SASERS (χ_{SA}= 0.37). Both SMSERS and SASERS are partially correlated.

1.5 orders of magnitude, wherein the largest value observed in a SM event is 46 times the smallest. This variance is consistent with the imperfect correlation found between the integrated anti-Stokes and Stokes intensities. Example SM spectra depicting the large

variance in ρ are plotted in Figure 4.4A. The distribution of ρ calculated from the SM events is depicted in gray in Figure 4.4B.

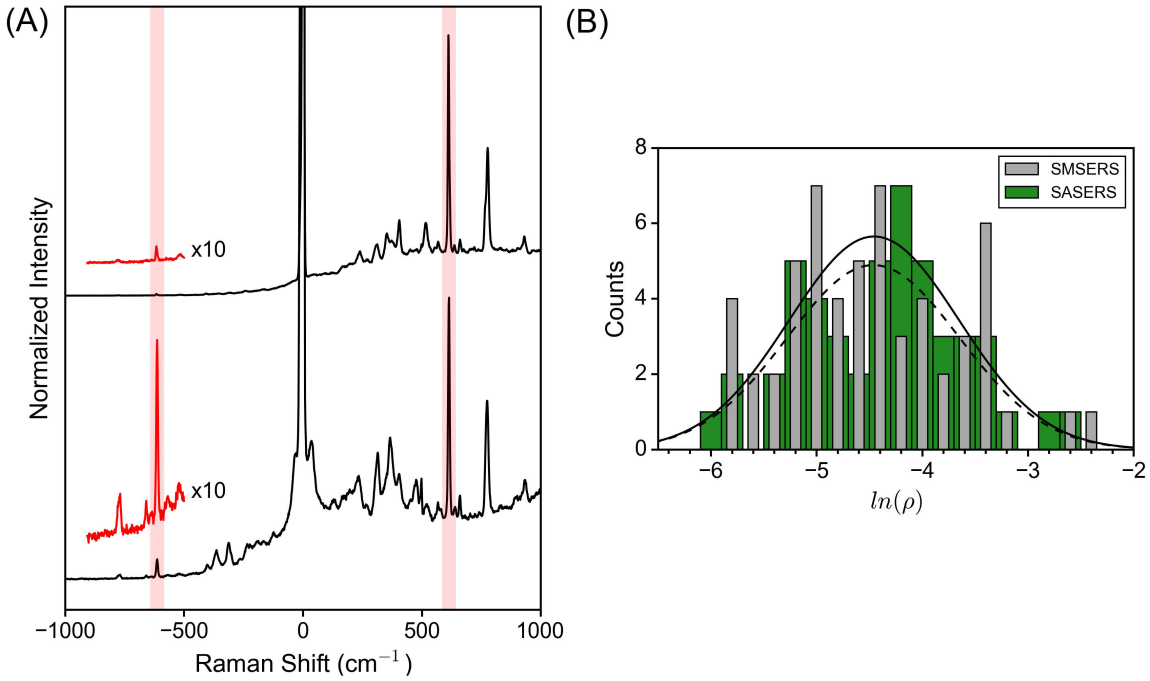

Figure 4.4. A) Stokes and anti-Stokes SMSERS of R6G on different Ag nanoparticle aggregates highlighting the variation in the anti-Stokes to Stokes ratio, ρ, for the 613 cm^{-1} mode (highlighted). Each spectrum is normalized to the intensity of the Stokes SERS peak. B) Distribution of ρ observed in SMSERS (Gray, Gaussian fit represented by a solid black line) and SASERS (Green, Gaussian fit represented by a dashed black line). Fits to both distributions are centered at -4.46 ln(ρ) units. The variance of ρ was more than 1.5 orders of magnitude for both SM and SASERS. Calculated standard deviations were 0.80 and 0.82 ln(ρ) units, respectively.

Since we expect the Stokes and anti-Stokes molecular cross sections to remain relatively constant among the molecules measured, the remaining factors that may cause variance in ρ from aggregate to aggregate are relative intensity fluctuations due to changes in excited state geometry,[155] EF variations between anti-Stokes and Stokes transitions, local heating, and vibrational pumping into the v=1 state. Reports suggesting evidence of vibrational pumping are typically conducted at significantly higher power densities than were used in the current study. For example, Maher et al. systematically varied the temperature of R6G on aggregated Ag nanoparticle aggregates from 10-300 K and measured ρ using 676 nm laser excitation with a power density of 1.6×10^4 W/cm^2 (nearly three orders of magnitude higher than our power density).[142] At this high laser intensity, the thermal population was observed to dictate ρ for the 613 cm^{-1} mode unless the sample temperature was below 100 K. As the vibrational pumping process scales linearly with excitation intensity (Equation 4.1), we will no longer involve this mechanism in further discussion.

When excited on molecular resonance, non-thermal vibrational state populations can also arise from absorption followed by relaxation into various vibrational levels in the electronic ground state. However, excited vibrational states are rapidly quenched in close proximity to a metal surface. Jensen and Schatz found that density functional theory simulations of R6G resonance Raman scattering accurately describe experimental data when calculated using the short-time approximation, which assumes that excited state lifetimes are short compared to the vibrational periods (55 fs for the 610 cm^{-1} mode of R6G).[37] With such short lifetimes, non-thermal excited state populations are negligible. Accordingly, a previous Stokes and anti-Stokes SERS investigation of R6G conducted on resonance at a power density $\sim$4 orders of magnitude higher than the current study

concluded that the vibrational states of R6G were in thermal equilibrium.[150] We now systematically analyze the contributions to ρ of the remaining three factors.

4.3.3. Fluctuations in Excited State Geometry

We previously determined that large relative intensity fluctuations are observed in plasmonically enhanced SM spectroscopy, in this case TERS, resulting from excited state geometry changes modifying the Franck-Condon overlap and thus the probabilities for individual transitions.[155] We expect similar phenomena to occur in SMSERS, the current analysis of which will be discussed in Chapter 5. Along the lines of this model, the overlap between the wave functions of particular vibrational states will not vary equivalently, so the anti-Stokes and Stokes SMSERS intensities of the same band may vary unevenly due to the same mechanism.

To assess whether or not this effect is contributing to the observed distribution of ρ we collected SERS of 50 individual aggregates coated in R6G-d_0 at high coverage. At these conditions, we expect such fluctuations to manifest to a lesser degree compared to SM events. The distribution of ρ is plotted in Figure 4.4B for SASERS (green). There is no discernible narrowing in the distribution upon increasing molecular coverage. We observe strong evidence of multi-molecule signals in SASERS, such as $\sim$10$\times$ higher signal intensity and increased signal stability and lifetime. Considering that excited state fluctuations are expected to be a SM phenomenon,[155] we conclude that varying excited state geometry is not the predominant mechanism responsible for the broad distribution. We must note that there is no guarantee that the signal from a high-coverage aggregate is ensemble averaged, as the signal may be primarily originating from an individual molecule residing

in a very strong EM hot spot. As such, SM phenomena may not be completely overcome in these measurements.

4.3.4. EF Wavelength Dependence

We now consider the wavelength dependence of enhancement, which appears to be a significant contributor to ρ. Referring back to Equation 4.1, ρ is expected to vary with the square of the ratio of the field strength at the anti-Stokes scattered photon wavelength ($\sim$515 nm) to that at the Stokes scattered photon wavelength ($\sim$550 nm):

$$\rho \propto \left| \frac{E_{aS}}{E_S} \right|^2 \tag{4.6}$$

One may suggest utilizing a correlated dark-field scattering (DFS) and SERS approach to account for the near field wavelength dependence associated with each aggregate under study. However, previous results indicate that the scattering spectrum measured in the far field is not an accurate measure of the wavelength dependence of the near field.[23,156] This disconnect arises from optically inaccessible plasmon resonances (i.e., dark modes) that are excited through coupling with other modes and contribute to the near field. An example correlated DFS and SASERS result is displayed in Figure 4.5A-B. Furthermore, a subset of correlated DFS and SASERS measurements confirm that a linear relationship between ρ and $(I_{DFS,aS}/I_{DFS,S})^2$ is not observed (Figure 4.5). Accordingly, the EF wavelength dependence cannot be accounted for spectroscopically.

Along these lines, we employed 3D FDTD simulations to model the scattering and EF from Ag nanoparticle aggregates. We utilized geometries based on transmission electron micrographs of aggregates previously observed to be present in the current nanoparticle

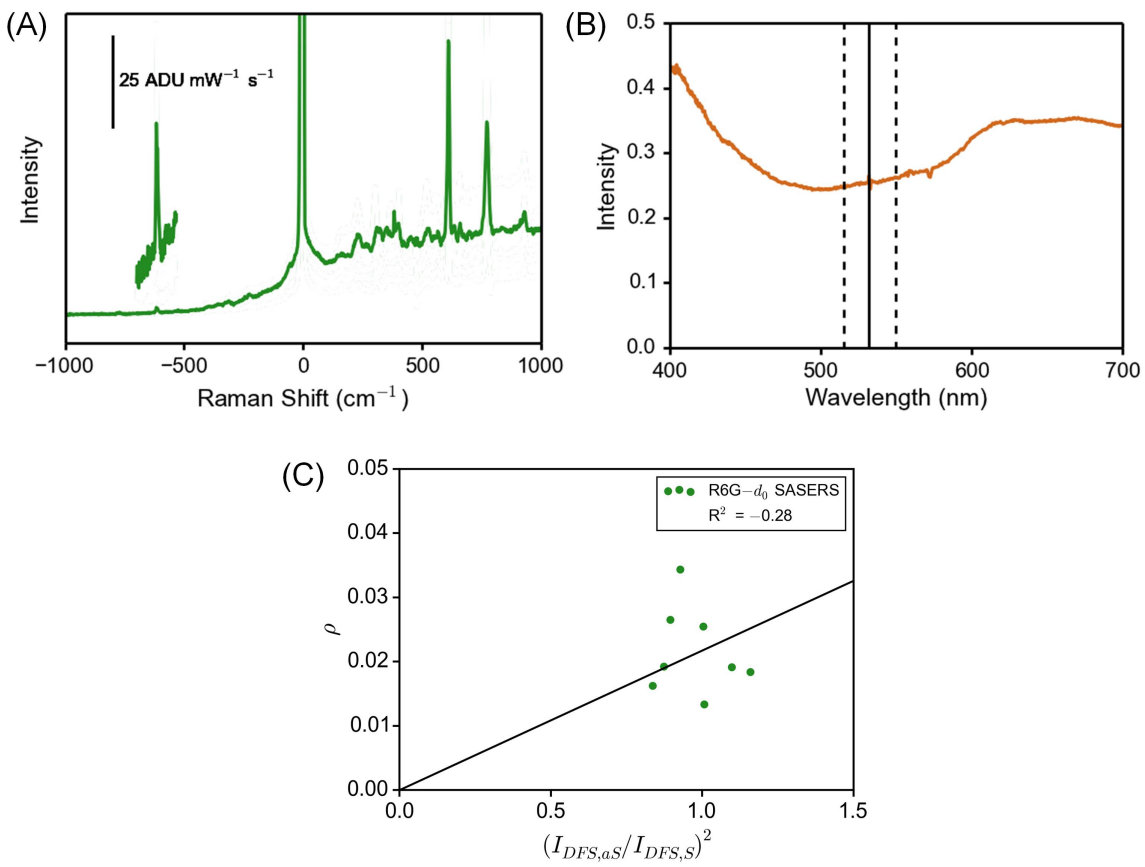

Figure 4.5. Example A) SASERS and B) dark-field scattering collected from the same individual aggregate. C) No obvious relationship is observed between dark-field scattering and ρ in correlated studies of individual Ag nanoparticle aggregates with high R6G coverage.

synthesis strategy.[22] Input geometries were approximated using simplified 3D shapes and modified slightly within the bounds of our synthesis to probe phenomena relevant to our study, including 1) EF differences between Stokes and anti-Stokes scattering at spatially resolved locations on the aggregate surface and 2) the relationship between nanoaggregate far field scattering and spatially resolved EF.

Enhancement in SERS is a product of the squares of the electric field intensities for both the incident (upward transition) and scattered (downward transition) fields. The square of the normalized field strength at the frequency of each transition, $|E/E_0|^2$, describes the enhancement of that process. The total EF can then be calculated using local electric field intensities in the following manner:

$$EF = \left|\frac{E_L}{E_0}\right|^2 \cdot \left|\frac{E_R}{E_0}\right|^2 \tag{4.7}$$

where the subscript L refers to the laser wavelength and the subscript R refers to the wavelength of the Raman scattered photon. The enhancement of the excitation process is identical for anti-Stokes and Stokes SERS (i.e., the first squared term in Equation 4.7 is a constant for a given location), but the enhancement of the emission process will depend on the field strength at the wavelength of the scattered photons.

We highlight a fused Ag nanoparticle trimer, whose geometry closely resembles an aggregate imaged in reference [22] (Figure 4.6). The results of FDTD calculations suggest that the highest intensity EM fields are located near one particular nanoparticle junction. Extracting the field distribution on one 2D slice through the aggregate allows us to compare the near field behavior on either side of this junction. Here, we only consider crevice sites large enough to fit a R6G molecule. Plotted in Figure 4.6C are the EFs calculated in the crevice sites on either side of the nanoparticle junction as a function of the scattered photon wavelength. At location 1, the anti-Stokes transition is preferentially enhanced by a factor of 1.9 compared to the Stokes transition. Alternatively, the Stokes transition is favored by a factor of 6.0 at location 2. From these plots we expect ρ to vary by as much

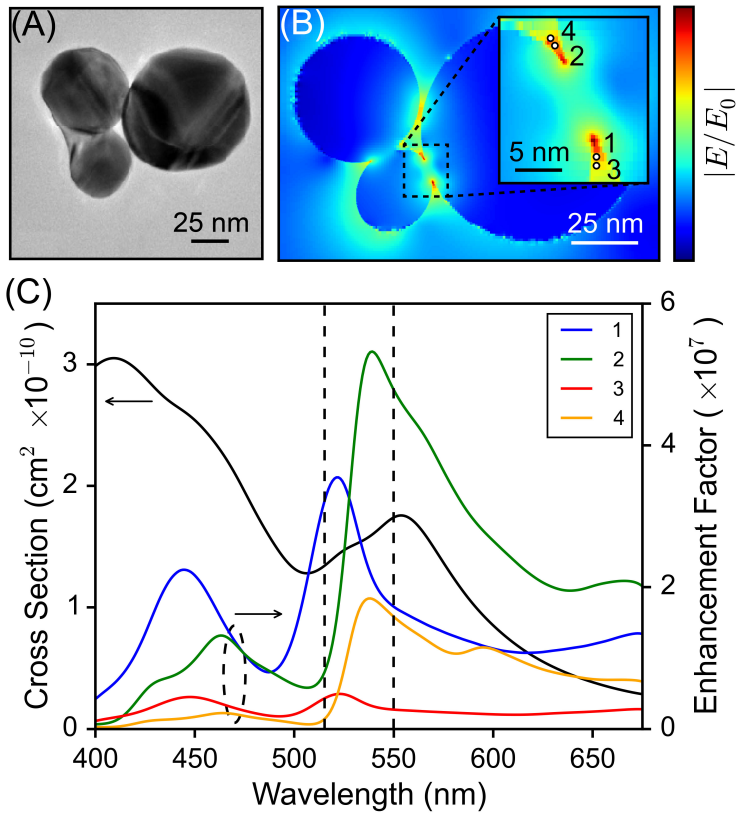

Figure 4.6. A) TEM image of a Ag nanoparticle trimer reproduced from reference [22]. B) FDTD simulated projection displayed in log scale of the field enhancement of a trimer with simplified and slightly modified geometry in the plane z = 25 nm (λ_{ex}= 532 nm). Locations 1 and 2 correspond to the indicated locations. Locations 3 and 4 are 1 nm from 1 and 2, respectively. C) EF (right axis), calculated using Equation 4.7, as a function of the scattered photon wavelength for locations 1–4. Also plotted is the calculated scattering cross section as a function of wavelength (left axis). Vertical dashed lines represent the wavelengths of anti-Stokes and Stokes scattering for the 612 cm^{-1} band of R6G excited at 532 nm.

as 11 within this single nanoparticle junction. A greater variance can be expected across a distribution of aggregate geometries.

To further probe the spatial extent to which the EF wavelength dependence can influence ρ, we also considered locations spaced 1 nm apart within the crevice sites. We find that a 1 nm translation of a molecule within a SERS hot spot will appreciably modulate ρ. Through diffusion from location 1 to location 3, the ratio of anti-Stokes to Stokes EF decreases from 1.9 to 1.6. Additionally, diffusion from location 2 to location 4 causes a decrease in the same ratio from 0.17 to 0.09. Considering all four locations, we expect ρ to vary by a factor as high as 21 for a single nanoparticle junction. It is clear that the nanoscale location of a probed molecule can greatly affect the value of ρ observed.

Figure 4.6C also depicts the simulated scattering spectrum of the same trimer plotted against wavelength. One can easily observe that the scattering spectrum is not representative of the near field at any of the reported locations on the aggregate surface. This can be rationalized by considering the nature of each property. First, the scattering spectrum considers the scattered field from the aggregate as a whole, whereas the near field is necessarily confined to the location at which it is probed. Second, only "bright" plasmonic modes (i.e., optically accessible modes) scatter efficiently to the far field. In contrast, both bright and dark modes, which are excited through plasmon coupling, contribute to near field enhancement.

The properties discussed above are not isolated to the specified case. Figure 4.7A-B show simulated nanoaggregates, specifically a dimer and a hexamer, along with calculated EF and ρ values for anti-Stokes and Stokes SMSER scattering at each considered molecular location. Calculated EF and ρ values at each location are tabulated in Table 4.1. An

equivalent disconnect between scattering and near field enhancement is observed, and we calculate EFs to be highly dependent on the wavelength of the scattered photon in all cases. From these results we conclude that ρ can be heavily influenced by EF differences in the near field, which contribute strongly to the broad observed distribution in ρ.

Table 4.1. Calculated EFs for the anti-Stokes and Stokes scattering and ρ from FDTD simulated dimer, trimer, and hexamer nanoparticle aggregates.

Aggregate	**Location**	**Calculated EF_{aS}**	**Calculated EF_S**	**ρ**
Dimer	1	9.2×10^7	3.9×10^7	2.4
	2	1.9×10^6	6.5×10^4	29
	3	2.5×10^7	1.2×10^7	2.1
	4	3.9×10^5	1.8×10^4	21
Trimer	1	3.2×10^7	1.7×10^4	1.9
	2	8.0×10^6	4.8×10^7	0.17
	3	4.3×10^6	2.7×10^6	1.6
	4	1.4×10^6	1.6×10^7	0.09
Hexamer	1	1.1×10^6	4.0×10^5	2.8
	2	1.5×10^6	8.9×10^5	1.6
	3	2.3×10^5	2.6×10^5	0.9
	4	2.5×10^5	9.2×10^4	2.7
	5	3.2×10^5	2.1×10^5	1.5
	6	6.5×10^4	5.2×10^4	1.3

4.3.5. Local Heating

We begin the discussion of local heating affecting the observed ratio with two assumptions: 1) molecules residing at stronger EM hot spots will give rise to the highest SERS signals, and 2) local heating is expected to occur to a greater extent at stronger hot spots. As

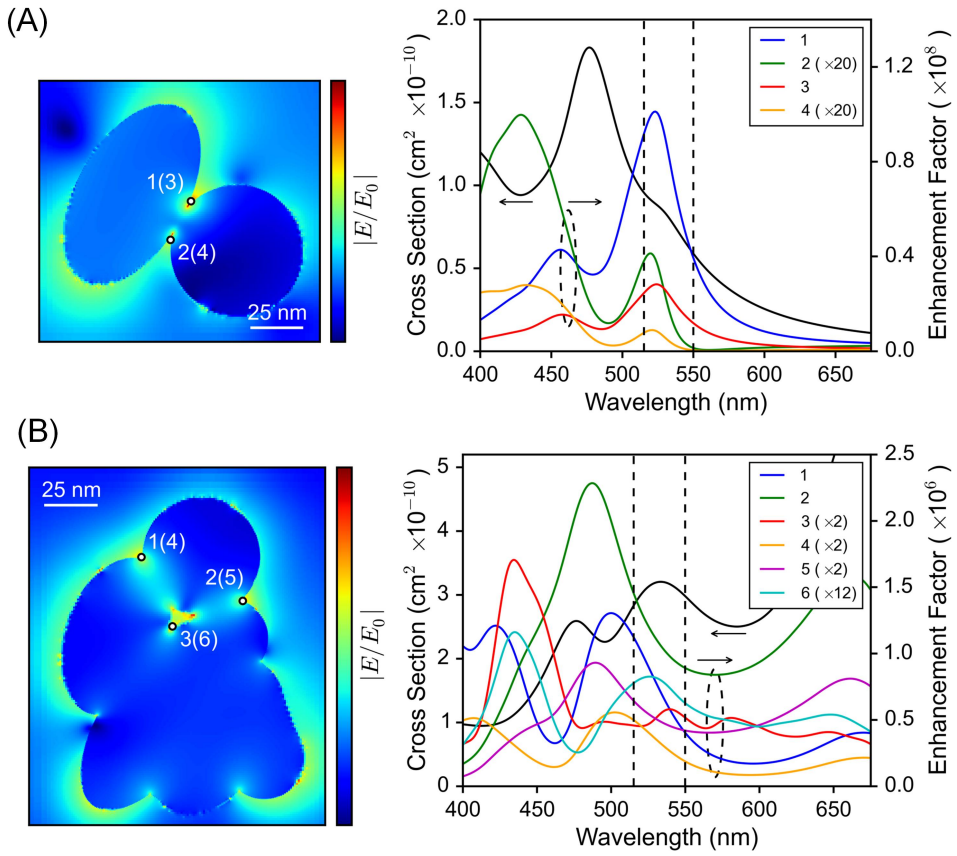

Figure 4.7. A) FDTD simulated projection of the field enhancement of a A) dimer and B) hexamer with simplified and slightly modified geometry in the plane z = 27.5 and z = 55, respectively (λ_{ex} = 532 nm). Enhancement factors, calculated using Equation 4.7, as a function of the scattered photon wavelength for locations 1-4 for the dimer and locations 1-6 hexamer are shown on the right. Locations indicated in the same crevice site are displaced 1 nm in the direction away from the nearest nanoparticle junction. Also plotted is the calculated scattering cross section as a function of wavelength. Vertical dashed lines represent the wavelengths of anti-Stokes and Stokes scattering for the 612 cm^{-1} band of R6G excited at 532 nm.

a result, greater heating should correlate with higher SERS intensity if local heating is appreciable. In order to test this theory, we need to define a measure to quantify SERS intensity. Using Stokes intensity (I_S), anti-Stokes intensity (I_{aS}), or their sum would bias the value toward the scattering intensity on one side of the laser line, so we instead define a reduced intensity, I_{red}, given by:

$$I_{red} = \frac{I_S I_{aS}}{I_S + I_{aS}} \tag{4.8}$$

A scatter plot relating ρ and I_{red} for SMSERS and SASERS events is depicted in Figure

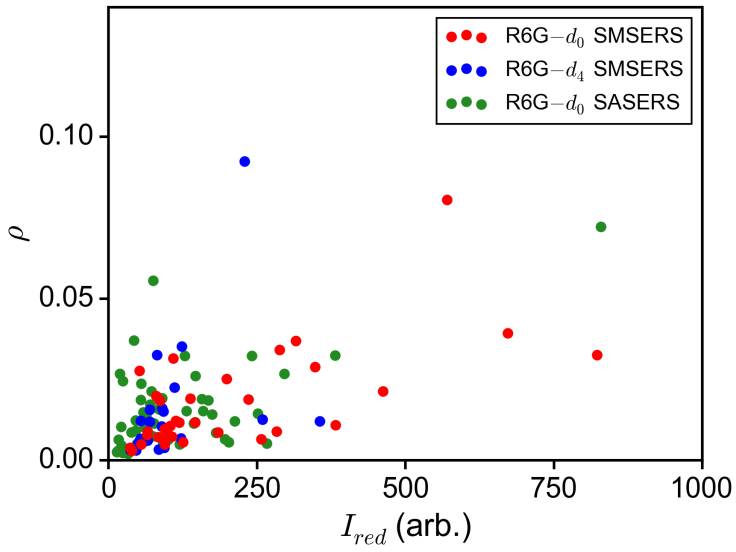

Figure 4.8. Scatter plot of ρ versus I_{red} (reduced intensity) for SMSERS (correlation, $\chi_{SM} = 0.52$) and SASERS (correlation, $\chi_{SA} = 0.59$).

4.8. A well-defined trend cannot be discerned, but their correlation as defined previously can be calculated. The statistical correlations between ρ and I_{red} for SMSERS and SASERS events are $\chi_{SM} = 0.52$ and $\chi_{SA} = 0.59$, respectively. Positive correlations suggest

that effects of heating are indeed observed. Should non-thermal vibrational state populations exist, we expect the associated increase in ρ to correlate with near field intensity and hence SER signal intensity, similar to local heating. However, since ρ is only partially correlated with I_{red}, significant contributions not related to vibrational state populations must be at play. This is expected, given the differences in near field enhancements between anti-Stokes and Stokes SERS.

With temperature playing a role, it is reasonable to expect a power dependence study to demonstrate a systematic increase in ρ with increasing laser power for individual aggregates. Along these lines, we swept the power across two orders of magnitude while collecting high-coverage SASERS and analyzed the resulting spectra (Figure 4.9). Interestingly, no systematic increase in ρ was evident. It can instead be observed to fluctuate upon modest variations in excitation power, and for one aggregate (Aggregate 1) it was observed to steadily decrease. We attribute these effects primarily to the mobility of R6G on Ag.[157] R6G diffusion across the surface of an aggregate results in each molecule experiencing a continually changing EM field, thereby modifying the observed anti-Stokes-to-Stokes ratio and the SERS reduced intensity. This claim is further supported by FDTD simulations (Figure 4.6 and Figure 4.7), which suggest that anti-Stokes and Stokes EFs vary appreciably at nearby locations inside a single hot spot, effectively modulating ρ and signal intensity if molecules were to diffuse even short distances. Local heating may increase diffusion from the hot spots, which could systematically increase or decrease ρ with increasing excitation power, depending on the geometry of the given aggregate.

This explanation is consistent with the irregular and unpredictable SERS reduced intensity (normalized to excitation power), as diffusion causes varying signal intensity over

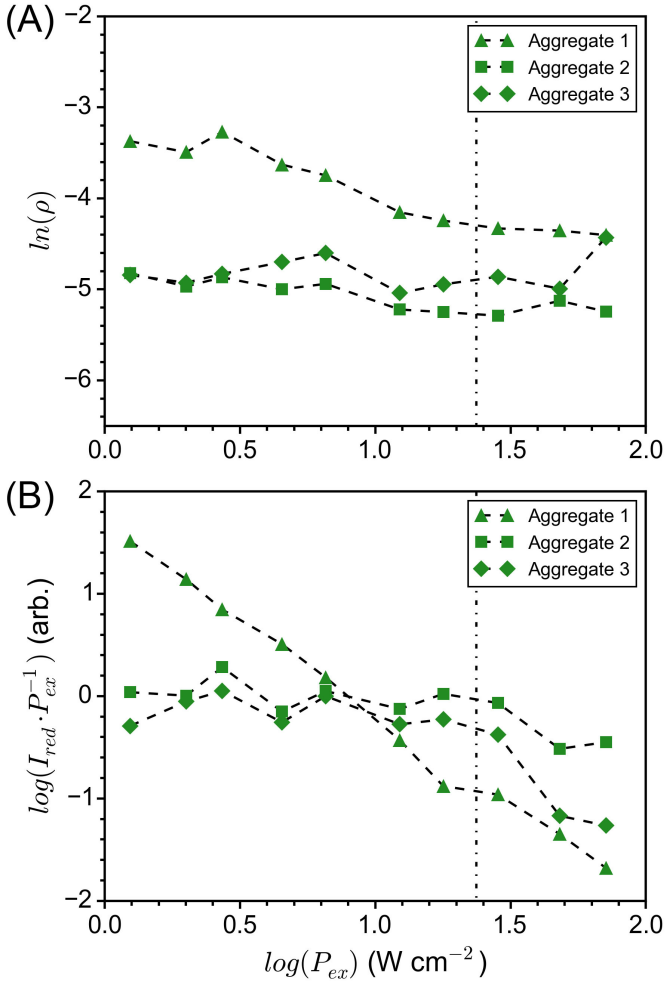

Figure 4.9. A) The power dependence for 3 individual high-coverage Ag nanopoarticle aggregates, which exhibit no systematic increase in ρ with increasing excitation power. B) Changes in ρ appear to coincide with decreases in I_{red} (reduced intensity) normalized to the excitation power used, consistent with surface diffusion away from the hot spots. The vertical dashed line indicates the power used for the other SERS spectra collected in this study.

time. The marked overall decreases in I_{red} and ρ observed for Aggregate 1 with increasing excitation power (Figure 4.9B) are consistent with the molecules diffusing away from highly enhancing regions and fits with our postulate that the molecules are experiencing a changing local EM field as they diffuse. Thermal desorption and reactive decay chemistry of photoexcited R6G are other potential mechanisms that could explain the decrease in signal intensity over time, but we believe they are less likely, considering the inert environment and laser powers used.

4.3.6. Outlook for Measuring Local Temperatures

When utilizing ρ to calculate local temperatures in plasmonic junctions, the above stated effects must be carefully considered. Fluctuations caused by small changes in the geometry of the excited state may be overcome in ensemble measurements, but the EF variations between anti-Stokes and Stokes scattering will not. Electrodynamics simulations using geometries obtained from electron micrographs may allow one to account for EF differences. Aggregated Ag nanoparticles are not ideal candidates for such measurements, as the positions of molecules contributing to the SER signal are not obvious for substrates with multiple, non-equivalent hot spots. More uniform plasmonic structures, such as those fabricated lithographically (see Chapter 3),[48,52,68] may better lend themselves to correlated studies. Furthermore, greater accuracy may be possible using TERS. The signal in TERS can emanate from a single hot spot (for a properly constructed tip), and the location of the molecules contributing to the signal can be known precisely through tip-enhanced Raman imaging.[158]

Once the EM field is characterized, an accurate local temperature may be quantifiable after correcting for other factors affecting ρ. Surface absorbance measurements[122] can approximate the resonance Raman cross sections at the Stokes and anti-Stokes emission wavelengths. However, one must address potential complications arising from non-equilibrium vibrational state populations arising from electronic excitation and subsequent relaxation. The local EM field may be computed as outlined above, with the caveat that the position(s) of molecule(s) contributing to the signal must be inferred. Utilizing chemisorbed or anchored molecules could eliminate variations caused by molecular diffusion and allow further deconvolution of contributing factors. In addition, the wavelength-dependent detection efficiency must be evaluated[143] with proper consideration of signal polarization in order to utilize ρ values obtained from collected spectra. Importantly, utilizing molecules with prominent modes at terahertz Raman shift frequencies (e.g., 50-500 cm^{-1}) will increase the accuracy of temperature determination, since the asymmetry factor (Equation 4.2) will approach unity as the difference between the Stokes and anti-Stokes scattering frequencies approaches zero.

4.4. Conclusion

We have demonstrated simultaneous Stokes and anti-Stokes SM detection with SERS using R6G on Ag nanoparticle aggregates. A small but positive correlation between anti-Stokes and Stokes signal intensity suggests that the two are related, but there is not a well-defined trend. Their ratio, ρ, was observed to vary by over 1.5 orders of magnitude in both SM and high-coverage SASERS events, likely caused by differences in EF between Stokes and anti-Stokes transitions convoluted with local temperature variations. Our results, as

well as those previously reported, suggest that the EM near field cannot be characterized using DFS. Positive correlations between ρ and reduced SER intensity suggest that local heating is observed, but the uncertainty in the EF wavelength dependence precludes a confident temperature calculation. 3D FDTD simulations of Ag nanoparticle aggregates demonstrate that EF is expected to vary significantly between anti-Stokes and Stokes transitions and that the wavelength dependence of enhancement is highly dependent on the location of the molecule. Additionally, we outline the considerations required to accurately quantify temperatures at the nanoscale. Accurate characterization of local temperatures would increase our understanding of plasmonic nanocavities and direct their implementation in various nanotechnologies.

CHAPTER 5

Relative Intensity Fluctuations in SMSERS

5.1. Introduction

The origin of signal fluctuations is of great interest to the SMSERS community. Signal fluctuations include blinking (on-off cycling of signal),[13,90,101–104,108,159] spectral wandering (the shift in frequency or position for a particular vibrational mode),[112,113] and relative intensity fluctuations between vibrational modes.[101,102,155,159] In Chapter 1 Section 1.5, we cover several studies dedicated to improving our fundamental understanding of the origin of blinking and spectral wandering, which have gathered the most attention.

Here, we focus on the relative intensity fluctuations that occur between the vibrational modes of a single molecule.[155,159] In crystal violet, for example, the low-frequency region of the spectra (<1100 cm^{-1}) was shown to fluctuate more dramatically than the high-frequency region of the spectra.[102] In R6G, it was observed that the 615 cm^{-1} and 774 cm^{-1} modes would blink in tandem, while the intensity of the remaining modes was maintained.[101] Lombardi et al., proposed that these rapid intensity fluctuations for only select modes is strongly correlated to vibronic coupling and that the steadier signals, which fade in and out gradually, are governed by Frank-Condon factors.[159]

Similarly Sonntag et al., investigated the large relative intensity fluctuations between individual modes in single molecule TERS (SMTERS) using TDDFT. To do this, the authors collected spectra continuously from a single tip location positioned above a Ag

film with SM level coverage of R6G. For some spectra, the lower wavenumber modes (e.g. 608 cm^{-1} and 771 cm^{-1}) were more intense, while in others, the higher wavenumber modes (e.g. 1362 cm^{-1} and 1651 cm^{-1}) were stronger. Molecular orientation effects on the relative intensities were neglected due to the independence of Raman tensor on rotation for resonant molecules. In addition, the authors observed no correlation in the intensity fluctuations between mode to mode, indicating the fluctuations occur independently. This further rules out orientation or adsorption geometry as the cause of the fluctuations. TDDFT calculations of the resonance Raman spectra of R6G revealed that the large relative intensity fluctuations could be reproduced by small changes in the excited-state properties of the molecule. Specifically, they were reproduced assuming small changes (<20%) in the excited-state bond lengths for the vibrational modes of picometers or less. Combining TDDFT and SM spectroscopies would allow the inversion of experimental data to obtain excited-state molecular properties, providing details on adsorbate-surface interactions normally hidden in ensemble measurements.

Sonntag et al., proposed that the relative intensity fluctuations should be generalizable to SMSERS. To verify this claim, we investigated SMSERS of R6G with 532 nm excitation, analogous to the SMTERS study. Next, we examined the influence of excitation wavelength on the signal fluctuations by comparing SMSERS for R6G with 532 nm and 561 nm excitation. Then, we examined the role of chemisorption and physisorption of the analyte to the nanoparticle surface by comparing the signal fluctuations for Rhodamine B Isothiocyanate (RBITC) with R6G at both wavelengths. For this investigation, we dosed aggregated Ag colloids with a dilute mixture R6G and BRITC, using the bianalyte

approach to verify SMSERS. Then, multiple time series (i.e., spectra versus time) for individual analytes were collected to observe the intensity fluctuations. The ability to answer questions about excited-state molecular properties will benefit future investigations into SM chemistry.

5.2. Experimental Methods

5.2.1. SMSERS Sample Preparation

The Ag colloids were synthesized using the procedure discussed in Section 4.2.1. The SMSERS samples were prepared by adding 1 mL of a mixture of 1×10^{-12} M R6G and RBITC each (total dye concentration 2×10^{-12} M) to 1 mL of the synthesized Ag colloid solution while stirring. Then, 1 mL of 20 mM NaCl was added to aggregate the nanoparticles and was vortexed for ∼20 seconds. The sample was covered from light and stored in the refrigerator to extend molecular lifetime. The Ag colloid/dye mixture was allowed to aggregate for a max of 1 day prior to dropcasting. All new solutions and samples were prepared after 2 days (1 day of aggregation and 1 day of data collection) as RBITC degraded overtime. On piranha cleaned (3:1 H_2SO_4 /30% H_2O_2) and base-treated (5:1:1 H_2O /NH_4OH /30% H_2O_2) glass coverslips (25 mm, #1.5), 100 μL of the aggregated Ag colloid/dye mixture was dropcast and dried under a flow of N_2.

5.2.2. Instrumentation and Time Series Data Collection

To limit photodegradation, the SMSERS samples were placed in a custom-built flow cell under a positive pressure of N_2 for the entire duration of data collection. The SMSERS signal was collected on an inverted microscope (Nikon TE300) with a 100× oil immersion

objective (Nikon, NA = 0.9). The excitation wavelengths, 532 nm (17 mW, Spectra-Physics, Millenia X) and 561 nm (38 mW, LASOS DPSSL Series), irradiated the sample at a grazing incidence angle of 30 degrees with a spot size of approximately 1 mm^2. A long-pass filter was used to filter out the excitation and Rayleigh scattered light ($\lambda_{ex} = 532$ nm: Semrock, LP03-532RS-25 and $\lambda_{ex} = 561$ nm: Semrock, LP02-561RU-25). During data collection, the long-pass filter was placed in the microscope to allow visual observation of the Raman scattering through the microscope eyepieces. The SERS-active nanoparticle aggregates were visually located and centered in the entrance slit of the spectrograph. Once a SERS-active nanoparticle aggregate was selected, spectra were collected every 3 seconds for 150 frames or until the molecule photobleached, creating a time series for each molecule. The collected signal was dispersed with a 1200 grooves/mm grating and detected with a liquid N_2-cooled CCD (Action 300i, Spec-10 400B).

5.3. Results and Discussion

5.3.1. Analytes and Excitation Wavelength

In SMTERS, the origin of the relative intensity fluctuations of vibrational modes is attributed to small variations in the excited-state properties of the molecule.[155] We expect the observation and origin of these signal fluctuations to be general to SMSERS. To verify this claim, we collected SMSERS of R6G and RBITC continuously over time to monitor the signal fluctuations. The molecular structures are provided in Figure 5.1A. Since R6G was investigated in the previous study, it provides a direct comparison between the intensity fluctuations observed via SMSERS and SMTERS. RBITC was chosen as the bianalyte partner because it strongly binds to the nanoparticle surface through a Ag-S bond via

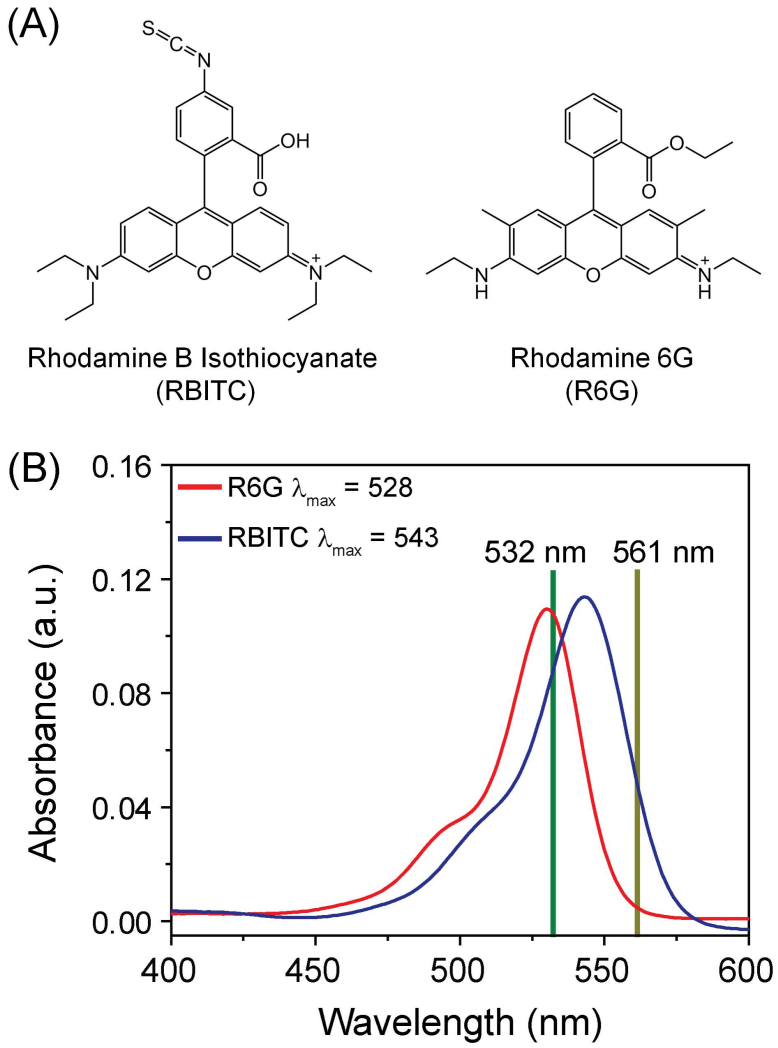

Figure 5.1. A) Molecular structure of R6G and RBITC. B) UV-Vis absorption spectra of R6G and RBITC with $\lambda_{max} = 528$ and 543 nm, respectively. The excitation wavelengths are indicated on the absorption spectrum at 532 nm and 561 nm.

the isothiocyanate functional group,[160,161] whereas R6G physisorbs to the nanoparticle surface. Thus, we are able to compare the fluctuation behavior of a weakly and strongly adsorbed resonant molecule. We further extend the previous study by examining the

role of excitation wavelength on the relative intensity fluctuations. Figure 5.1B shows the absorption spectra of R6G (red, λ_{max} = 528 nm) and RBITC (blue, λ_{max} = 543 nm) along with the indicated excitation wavelengths. 532 nm excitation is on resonance with R6G while 561 nm is red-shifted from the absorption. For RBITC, both excitation wavelengths overlapped with the electronic absorption. Since the intensity fluctuations have been demonstrated to result from changes in excited-state molecular properties of the molecule, we expect the fluctuations to be more dramatic for R6G at 532 nm excitation than at 561 nm excitation, and to occur at both wavelengths for RBITC. Excitation with 594 nm incident light (further off resonance) was also attempted, but the signal was too weak to observe intensity fluctuations. Future efforts will explore intensity fluctuations at 514 nm excitation to create a more complete picture. Finally, due to the inherent heterogeneity of SM events, we collected multiple time series at each wavelength to elucidate trends in the signal fluctuations across discrete molecules.

5.3.2. Verification of SMSERS

To verify SMSERS, we used the bianalyte approach with R6G and RBITC.[57,96] Figure 5.2A shows example SMSERS spectra of R6G and RBITC collected from aggregated Ag colloids. Multiple peaks were used to differentiate the spectra of both analytes. Specifically, the peaks for R6G at 615, 771, and 1314 cm^{-1} and for RBITC at 625, 730, and 1277 cm^{-1}.

Figure 5.2B provides the total individual counts of R6G and RBITC and events indicating the presence of both analytes. The counts collected with 532 nm excitation are indicated by the darker shading and 561 nm by the lighter shading. Based on the

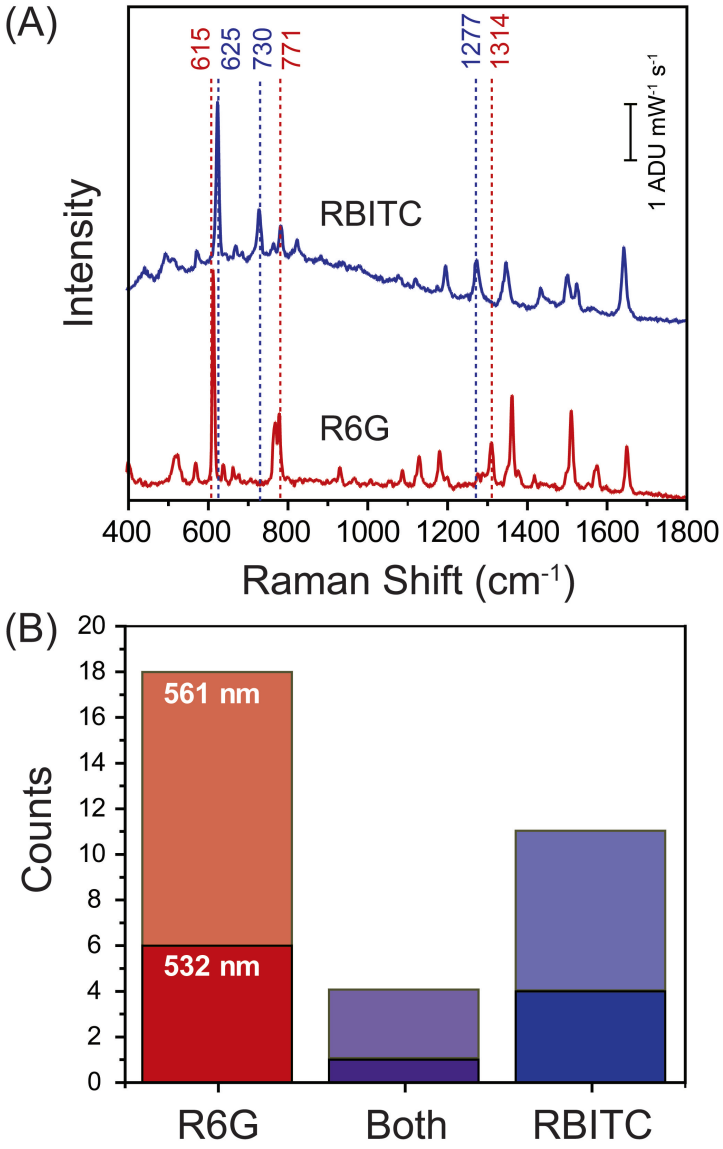

Figure 5.2. A) Example SMSERS spectra of R6G and RBITC collected from Ag colloids dosed with a mixture of $2x10^{-12}$ M R6G and RBITC. Multiple peaks were used to differentiate between R6G and RBITC as labeled on the spectra. B) Histogram of counts for the bianalyte experiments with R6G and RBITC. The darker shading indicates counts collected at 532 nm excitation and the lighter shading indicates counts collected at 561 nm.

verification of SMSERS with bianalyte partners covered in Chapter 2, we used a joint Poisson-binomial model (Equation 2.1) to determine our α (average number of molecules detected per spectrum), and β (probability of detecting analyte 1). β is not assumed to be 0.5 (i.e., having a 50/50 detection probability) because R6G and RBITC have different surface binding chemistries.[44,160,161] Verification was accomplished by calculating when α, β, and the experimental percentage of individual character for R6G (54.5%) and RBITC (33.3%) from the histogram simultaneously converge, as covered in Chapter 2 Section 2.3.3. For this histogram, we find a $\beta = 0.61$ and $\alpha = 0.51$, indicating on average less than 1 molecules detected per spectrum. While the overall counts are low at only 33, we believe SM level coverage is satisfactorily verified for the purpose of this investigation. For the remainder of this study, we only investigated the signal fluctuations from time series that indicated individual analyte character and did not photobleach immediately (i.e., within the first few frames). However, molecules that photobleached were still included in the overall counts for verifying SMSERS. In general, RBITC was less photostable than R6G, resulting in fewer full time series for analysis.

5.3.3. Signal Fluctuations

5.3.3.1. Rhodamine 6G at 532 nm Excitation. In the previous SMTERS study, it was noted for some spectra the low-wavenumber modes (e.g., 608 cm^{-1} and 771 cm^{-1}) were more intense, while in other spectra the high-wavenumber modes (e.g., 1362 cm^{-1} and 1651 cm^{-1}) had a stronger intensity. Notably, the ratio of the integrated peak intensities for the 608 cm^{-1} to 1651 cm^{-1} mode switched from 3:1 to 0.2:1.[155] For simplicity, we will refer to

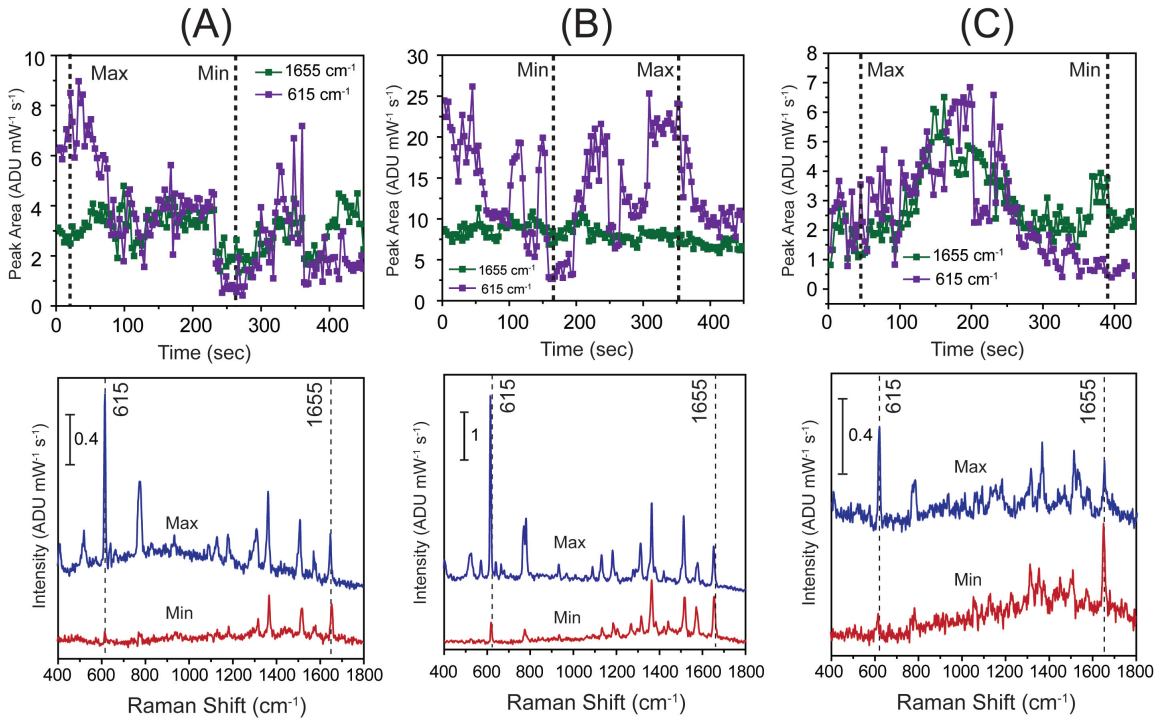

Figure 5.3. Three example time series showing intensity "flips" of the low- and high-wavenumber modes of R6G with λ_{ex} = 532 nm. Top) Raman peak area trajectories for the 615 and 1655 cm^{-1} vibrational modes. The peak area is shown versus time out to 150 frames or until the molecule photobleached. Spectra were collected with 3 sec acquisition (total possible time of 450 sec). Bottom) Spectra corresponding to the max and min peak area ratio (615:1655) for each time series. The location of the max and min spectra are indicated on their corresponding Raman trajectories. Only data points which had signal above the noise are shown.

this switch of the max intensity between the low- and high-wavenumber regions as "flips" in intensity.

As expected, we observed similar relative intensity fluctuations for R6G with SMSERS. Figure 5.3A-C shows 3 time series collected with 532 nm excitation. On the top are Raman peak area trajectories for the 615 cm^{-1} and 1655 cm^{-1} modes versus time. On the bottom are the spectra corresponding to the max and min 615:1655 ratio, highlighting the dramatic "flips" in intensity observed between the low- and high-wavenumber modes. Dashed lines indicated the location of the spectra corresponding to the max and min ratios on the Raman trajectories, which are A) 3:1 to 0.2:1, B) 3:1 to 0.3:1, and C) 3:1 to 0.1:1. All of these time series intensity ratios are in close agreement with the ratios observed with SMTERS (3:1 to 0.2:1) and have a large spread in the max to min ratio (Table 5.1). It is also worth noting that each time series has a unique behavior, showing the importance of studying multiple molecules to elucidate behavioral trends.

In Figure 5.3B, we observe the largest variance in signal intensity for the 615 cm^{-1} mode. As such, we investigated this time series in more detail as provided in Figure 5.4. Here, we plotted the Raman peak area trajectories for multiple modes (615, 1365, 1515, and 1655 cm^{-1}). It can be seen that the higher wavenumber modes (1365, 1515, and 1655 cm^{-1}) do not fluctuate in intensity as dramatically at the 615 cm^{-1} mode, highlighting the independent nature of these fluctuations. Additonally, we show the change in peak position from frame 1 (3 sec) in Figure 5.4B. The spectral wandering is consistent with previous reports (<5 cm^{-1}).[40,155] One possible explanation for the observed changes in peak intensity is that shifts in the peak frequency enhance or dampen the vibrational modes. Figure 5.4C show the change in Raman shift versus integrated peak area. As in SMTERS,[155] we observe no relationship between the spectral wandering and peak intensity.

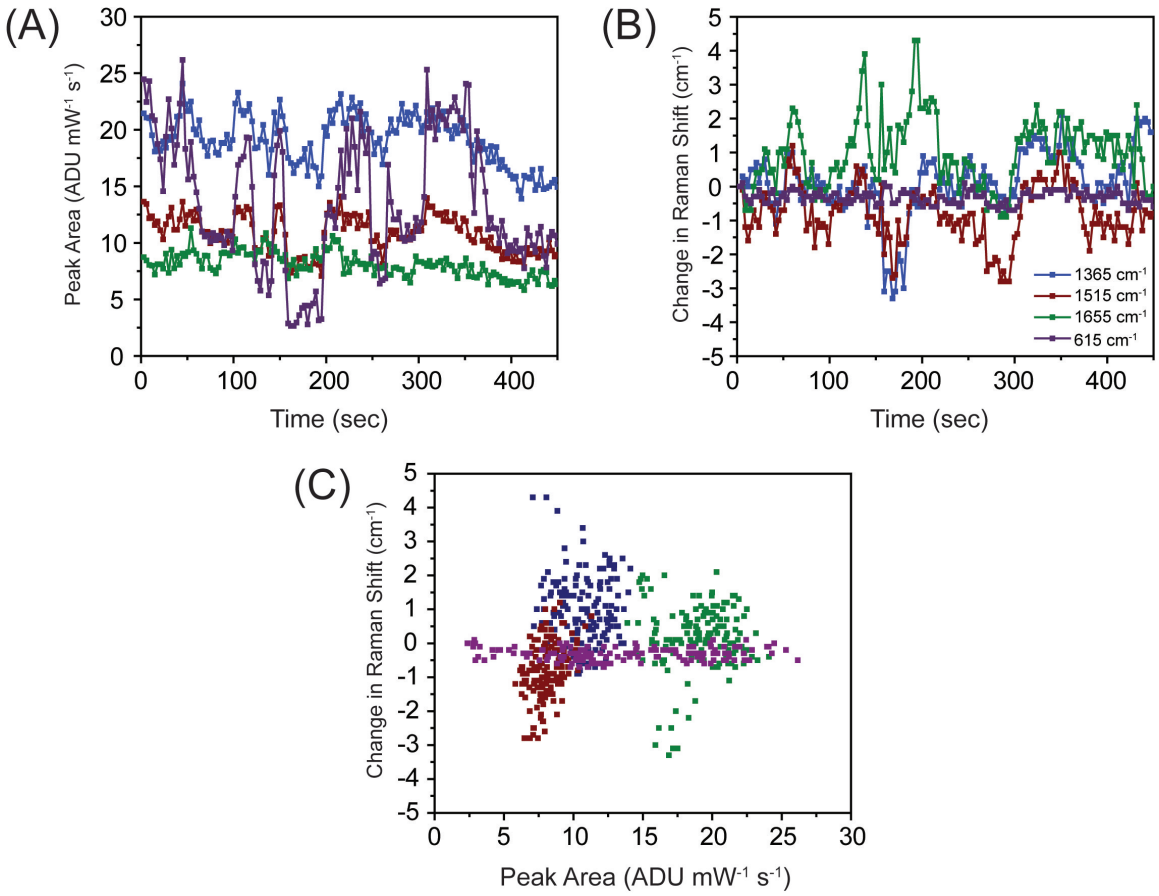

Figure 5.4. A) Time series for R6G at $\lambda_{ex} = 532$ nm with the largest variance in signal intensity for the 615 cm^{-1} vibrational mode (purple). Also shown are the Raman peak area trajectories for 1365 (blue), 1515 (red), and 1655 (green) cm^{-1} vibrational modes. The high-wavenumber modes (1365, 1515, and 1655 cm^{-1}) were not observed to fluctuate in intensity as dramatically at the 615 cm^{-1} mode. B) Change in peak center frequency from frame 1 (3 sec) for all 4 vibrational modes versus time. Spectral wandering was <5 cm^{-1}. C) Peak area versus change in peak frequency for all 4 vibrational modes. No relationship is observed.

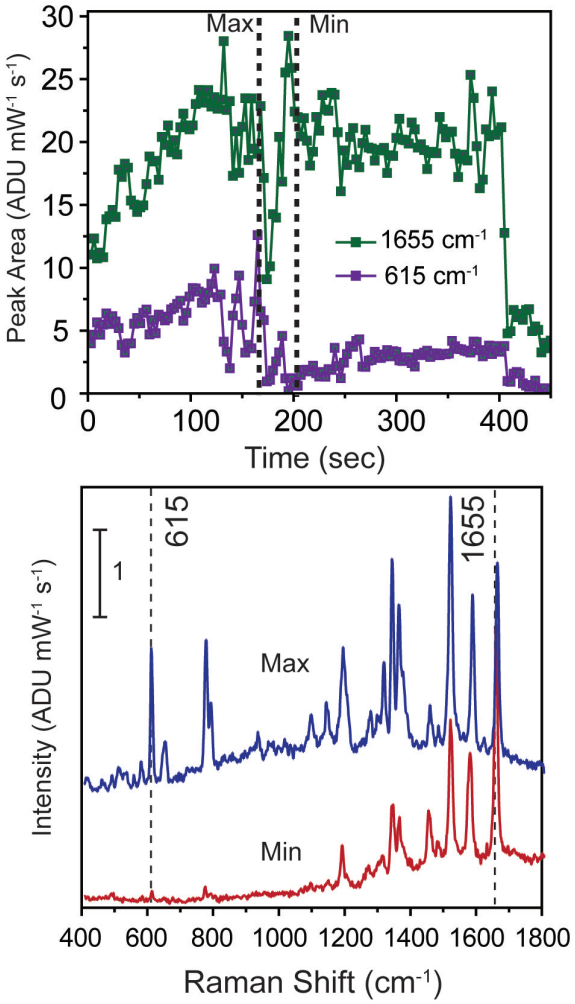

Figure 5.5. Example time series for R6G at $\lambda_{ex} = 532$ nm where the low- and high-wavenumber modes were not observed to "flip" in intensity. In addition, the high-wavenumber modes fluctuated more dramatically than the low-wavenumber modes, unlike in Figure 5.3.

In general, the 615 cm^{-1} vibrational mode for R6G fluctuates more dramatically than the 1655 cm^{-1}. One notable exception is shown in Figure 5.5. In this time series, the high-wavenumber region dominated in intensity and was observed to have a larger variance in signal intensity than the lower wavenumber region. The max and min 615:1655 ratios

are 0.7:1 to 0.03:1, observing a spread in the ratio of over an order of magnitude, even though, the intensities did not "flip". Future TDDFT simulations may help describe the molecular properties leading to this aberrant behavior.

In summary, the large relative intensity fluctuations observed in SMTERS are also observed in SMSERS for R6G at 532 nm excitation. The intensity ratios for the 615 and 1655 cm^{-1} vibrational modes (Table 5.1) are comparable between both SM techniques. In addition, we observed these trends across multiple, individual molecules of R6G.

5.3.3.2. Rhodamine 6G at 561 nm Excitation. Next, we investigated if the large relative intensity fluctuations are observed off resonance for R6G. Figure 5.6 shows the Raman peak area trajectories and spectra corresponding to the max and min 615:1655 ratio for 3 time series of R6G collected with 561 nm excitation (Table 5.2). Intensity "flips" between the high-wavenumber and low-wavenumber regions are not observed. In general, the signals are also steadier than at 532 nm excitation, as can be visualized in the spectra corresponding to the max and min peak ratios. At this wavelength, the spread in the max to min ratio are much smaller at $\leq$6, supporting our claim that the intensity fluctuations result from small changes in the excite-state properties of the molecule due to excitation on resonance.[155]

5.3.3.3. Rhodamine B Isothiocyanate at 532 and 561 nm. As discussed previously, R6G can diffuse across the nanoparticle surface. To experimentally investigate if diffusion plays a role in the signal fluctuations, we compared RBITC, which should strongly bind to the nanoparticle surface, with R6G. Figure 5.7A-C show example time series collected for RBITC at A) 532 and B-C) 561 nm excitation. In Figure 5.7A-B the spectra correspond to the max and min ratios (625:1655) of 5:1 to 0.1:1 and 3:1 to 0.3:1, respectively. These

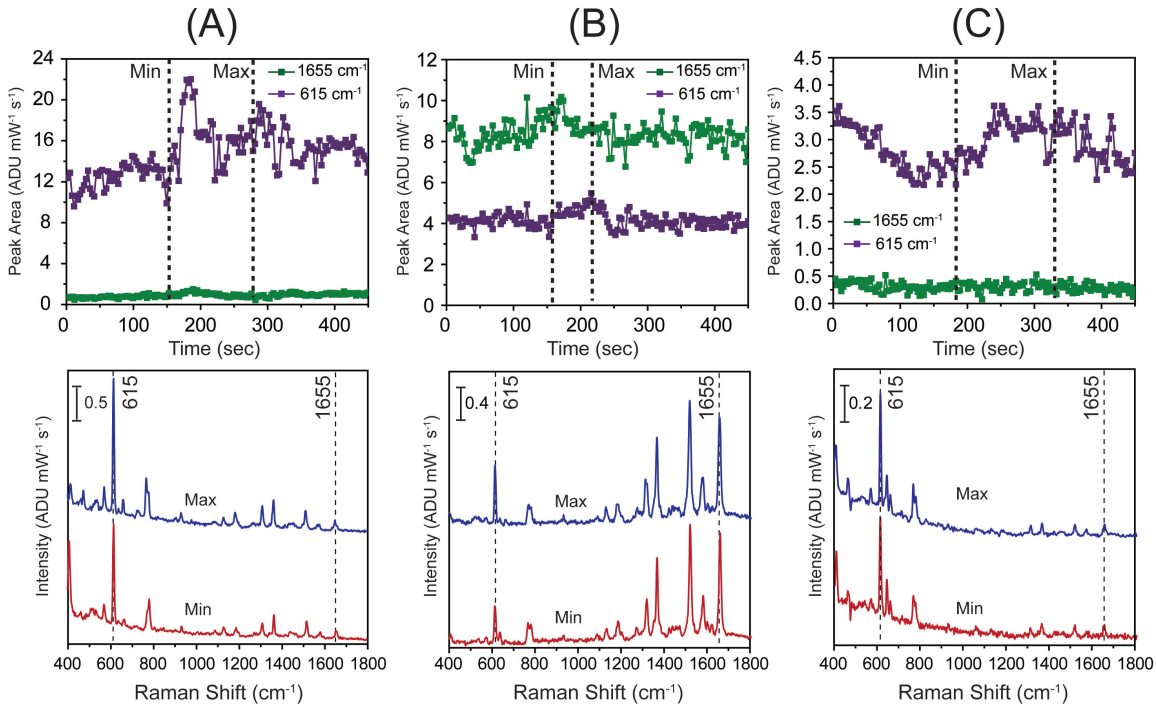

Figure 5.6. Three example time series for R6G with λ_{ex} = 561 nm where intensity "flips" of the low- and high-wavenumber modes were not observed. Top) Raman peak area trajectories for the 615 and 1655 cm^{-1} vibrational modes. The peak area is shown versus time out to 150 frames with 3 sec acquisition (total time 450 sec). Bottom) Spectra corresponding to the max and min peak area ratio (615:1655) for each time series. The location of the max and min spectra are indicated on their corresponding Raman trajectories. Only data points which had signal above the noise are shown.

ratios are in close agreement with R6G and show similar "flips" in intensity (Tables 5.1 and 5.2). As with the previous study,[155] we provide strong evidence that the large relative fluctuations are not the result of near field gradients due to molecular diffusion.

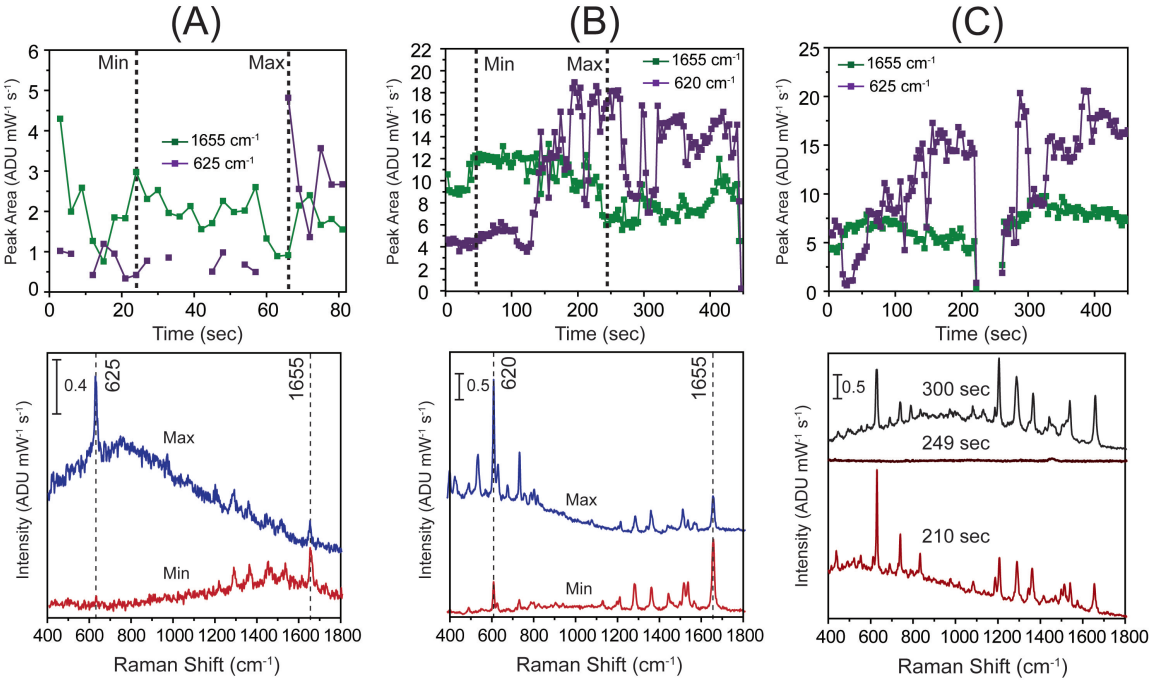

Figure 5.7. Three example time series for RBITC with A) $\lambda_{ex} = 532$ nm and B-C) $\lambda_{ex} = 561$ nm. Intensity "flips" of the low- and high-wavenumber modes were observed at both wavelengths. Top) Raman peak area trajectories for the 625 and 1655 cm^{-1} vibrational modes. The peak area is shown versus time out to 150 frames or until the molecule photobleached. Each frame had a 3 sec acquisition (total possible time 450 sec). Only data points which had signal above the noise are shown. A-B Bottom) Spectra corresponding to the max and min peak area ratio (625:1655) for each time series. The location of the max and min spectra are indicated on their corresponding Raman trajectories. C Bottom) Example spectra collected prior to, during, and after a blinking event for RBITC.

In addition, Figure 5.7C shows a SM event of RBITC where blinking was observed. At 225 sec the signal cycles off and at 261 sec the signal returns. Example spectra prior to, during, and after the blinking event are provided. Surface diffusion out of the hot spot is generally accepted as a mechanism for blinking.[90,94,106] This time series, however, suggests that surface diffusion is inadequate to fully explain the blinking behavior observed in SMSERS. An alternative explanation could be the molecule entering a metastable or non-emissive state.[110]

5.3.4. Observed Trends in Relative Intensity Fluctuations

Table 5.1. Peak area ratios of the 615/625 to 1655 cm^{-1} vibrational modes of R6G and RBITC at 532 nm.

	532 nm		
Analyte	**Max Ratio 615/625:1655**	**Min Ratio 615/625:1655**	**Factor Max/Min**
R6G 1	6:1	0.5:1	11
R6G 2	0.7:1	0.03:1	21
R6G 3	3:1	0.2:1	16
R6G 4	3:1	0.3:1	11
R6G 5	3:1	0.1:1	24
R6G 6	4:1	0.6:1	7
RBITC 1	**2:1**	**0.6:1**	**4**
RBITC 2	**5:1**	**0.1:1**	**37**

While the behavior of each molecule is unique due to the inherent heterogeneity of their environments, we are still able to observe trends in behavior across multiple molecules. In the above sections, we provide experimental evidence that exciting on resonance with

Table 5.2. Peak area ratios of the 615/625 to 1655 cm^{-1} vibrational modes of R6G and RBITC at 561 nm.

561 nm			
Analyte	**Max Ratio 615/625:1655**	**Min Ratio 615/625:1655**	**Factor Max/Min**
R6G 1	15:1	7:1	2
R6G 2	35:1	11:1	3
R6G 3	0.7:1	0.4:1	2
R6G 4	18:1	5:1	4
R6G 5	19:1	12:1	2
R6G 6	31:1	8:1	4
R6G 7	20:1	5:1	3
R6G 8	22:1	3:1	6
R6G 9	22:1	7:1	3
R6G 10	10:1	3:1	4
R6G 11	6:1	2:1	4
R6G 12	10:1	5:1	2
RBITC 1	**4:1**	**0.1:1**	**40**
RBITC 2	**4:1**	**1:1**	**3**
RBITC 3	**1:1**	**0.03:1**	**29**
RBITC 4	**4:1**	**0.1:1**	**47**
RBITC 5	**3:1**	**0.3:1**	**9**

the electronic absorption of the molecule is necessary for inducing the relative signal fluctuations. First, intensity "flips" of the low- and high-wavenumber modes are not observed for R6G with 561 nm excitation, which is red-shifted from the absorption of R6G. Second, there is a greater spread in the max to min ratio of peak area observed at 532 nm excitation (all $\geq$7) than at 561 nm excitation (all $\leq$6), indicating more intense

signal fluctuations. Third, strong relative fluctuations are observed for RBITC at both wavelengths which overlap with its absorption. Tables 5.1 and 5.2 present the max and min 615/625:1655 peak area ratios and the spread of max to min ratio for every time series collected.

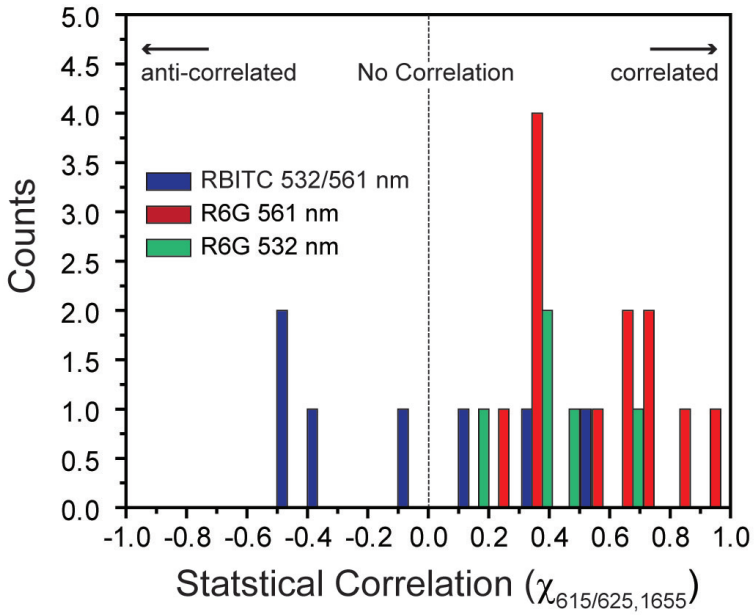

Figure 5.8. Histogram of statistical correlations between the 615/625 and 1655 cm^{-1} vibrational modes of R6G at 532 nm (green) and 561 nm (red) and RBITC at both wavelengths (blue), respectively, for all of the time series. R6G has small to large positive correlations with 561 nm excitation trending towards higher correlations than 532 nm excitation. RBITC has predominately small negative to zero correlation at both wavelengths.

Next, we calculated the statistical correlation, χ, between the integrated peak areas for the 615/625 and 1655 cm^{-1} modes for R6G and RBITC via Equation 4.4. Computed χ values lie within the range [-1,1], where $\chi = 1$ denotes perfectly correlated variables, χ

= -1 denotes perfectly anti-correlated variables, and $\chi = 0$ denotes variables that are not correlated. Values in between indicate partial correlation or partial anti-correlation. Figure 5.8 shows the statistical correlations, χ, for R6G at 532 nm (green) and 561 nm (red) and RBITC at both wavelengths (blue). R6G has small positive to large positive statistical correlations, with the tail end of the 561 nm distribution trending towards higher correlation than with 532 nm. The small positive correlations likely result from the overall intensity changes observed throughout the time series. We believe these overarching changes result from R6G diffusing around the nanoparticle hot spot experiencing different field strengths. The vibrational modes, however, are not fully correlated suggesting that the relative signal fluctuations of the vibrational modes are independent of each other, particularly, at 532 nm excitation. This can be visualized in Figure 5.4A where the signal of all vibrational modes gradually drops and rises together amongst rapid relative intensity fluctuations. The trend towards a higher correlation with 561 nm excitation indicates that the relative intensity fluctuations are weaker, and the signal intensities are more likely being dominated by R6G diffusing in the nanoparticle hot spot. No anti-correlation is observed for R6G meaning the signal fluctuations are not inversely related.

Unlike R6G, RBITC has predominately small negative to zero correlation for the signal intensities of the 625 and 1655 cm^{-1} modes. Since RBITC is bound to the nanoparticle surface the overall intensity changes due to diffusion are not present. For example, in Figure 5.6 gradual overall changes in intensity are not observed. The lack of correlation observed for RBITC further supports our claim that the relative intensity fluctuations of vibrational modes occur independently. The statistical counts, however, are small due to

the rarity of observing a long-lived SM event. Future studies will focus on improving the statistics to more rigorously confirm these trends.

5.4. Conclusion

That data presented above supports three main conclusions. First, we have verified that the relative intensity fluctuations, studied previously in SMTERS,[155] are observed with SMSERS. Second, we showed that the relative intensity fluctuations are more intense when SMSERS is excited on resonance with the analyte. Third, we observed relative intensity fluctuations for analytes physisorbed and chemisorbed to the nanoparticle surface, providing further evidence that these fluctuations are not the result of near field gradients in the hot spot. Future studies will focus on matching the experimentally obtained fluctuations with TDDFT calculations to probe the excited-state lifetime, energy, and geometry of the molecules. The ability to probe excited-state molecular properties will aide in understanding adsorbate-surface interactions and SM chemistry in future investigations.

CHAPTER 6

Single Molecule Chemistry and Future Directions for SMSERS

SMSERS has matured into a powerful vibrational spectroscopy. Recently, researchers have begun to extend this technique to answering questions about molecular reactivity at its most fundamental limit. This Chapter will highlight recent application of SMSERS towards monitoring catalytic and electrochemical reactions, observing single molecule tautomerization, and more. Then, we will conclude with a discussion of future directions for SMSERS studies.*

6.1. Single Molecule Chemistry

6.1.1. Electrochemical SMSERS

As the study of electrochemistry shrinks to the nanoscale[162,163] interest has grown in monitoring the electrochemistry of single molecules with vibrational spectroscopy.[164] Combining electrochemistry with SMSERS (EC-SMSERS) is advantageous because SM detection is readily attainable with rich chemical information. Thus, it is possible to monitor structural changes of a molecule in close proximity to a nanostructured metallic surface as a function of applied potential.

SMSERS was first combined with electrochemistry in 2010. For this study, a bianalyte approach with R6G and NB adsorbed on a Ag mirror-Ag nanoparticle substrate working

*This Chapter is reproduced in part with permission from reference [14]. Copyright 2016 American Chemical Society.

electrode was used.[165] As the potential was swept positive from -0.5 V to -0.1 V, the $2H^+$, $2e^-$ oxidation of NB was observed by the appearance of NB signal. Upon the negative sweep, the reduction of NB was indicated by the loss of NB signal. The authors observed slight differences in the bulk surface cyclic voltammogram versus the single molecule histogram, which demonstrates the power of using SMSERS for resolving heterogeneous behaviors in single molecule electrochemistry. In later work, the authors extended the study with a high-resolution grating. This allowed the authors to observe changes in the NB vibrational frequencies as a function of applied potential, which were attributed to reorientation of the NB molecule.[166] EC-SMSERS was also implemented in a study by Wang et al. to understand photoelectrochemical charge transfer dynamics in hemin, an iron protoporphyrin, where it was found that local thermal fluctuations govern electron transfer dynamics in the protoporphyrin system.[167]

More recently, EC-SMSERS was implemented to study single, heterogeneous electron transfer events of R6G in non-aqueous conditions.[111] SMSERS detection was first validated by the isotopologue proof with R6G.[40] The sample consisted of R6G physisorbed on Ag nanoparticle aggregates covalently tethered to an ITO coverslip.[40] The electrochemical conversion of a single R6G molecule to its neutral radical form was observed by stepping the potential of the working electrode from 0 V to -1.2 V in -0.1 V steps and monitoring the SMSERS spectra as a function of the applied potential. The potential at which the R6G SMSERS signal was no longer observed was counted as a loss event, indicating the reduction of R6G to its neutral radical form. The majority of SMSERS signal loss events, however, did not have a subsequent oxidative signal return, indicative

of electrochemically-induced desorptive losses. This issue can be addressed using a covalently tethered molecule to the Ag nanoparticle surface, as demonstrated in recent work from the Willets group.[64] Despite the occurrence of electrochemical desorptive losses, the total SMSERS loss events followed the profile of an ensemble-surface voltammogram of R6G on a Ag surface. Interestingly, there were a small number of SMSERS signal loss events that occurred in the underpotential region of the surface voltammogram which are attributed to site-specific reduction potentials on the Ag nanoparticle surface. Observing single electron transfer with EC-SMSERS strongly demonstrates the electrochemical heterogeneity of nanoparticles and elucidates the importance of site-specific electrochemical activity on surfaces.

Other studies have exploited the 5-10 nm spatial precision of super-localization SERS, as discussed in Section 1.2.2, to understand the spatial dependence of electrochemical events on Ag nanoparticles.[65,168] As in previous studies, NB was physisorbed onto Ag nanoparticle aggregates to observe the $2H^+$, $2e^-$ reduction reaction.[165,166] At single molecule level coverage, the fitted SMSERS emission centroid displays two unique reduction potentials that are observed upon subsequent potential sweeps, which correspond to two distinct positions of the molecule on the Ag nanoparticle aggregate. This result suggests that the reduction potential of NB is dependent upon molecular location on the Ag nanoparticle surface. Single molecules, however, remained emissive for only a small number of potential sweep cycles. Thus, in order to confirm the site-specific electrochemical behavior of NB, the authors performed the same experiment at few-molecule coverage. At this coverage, the intensity-weighted SMSERS centroid position shifted as a function of potential suggesting that single NB molecules are being oxidized or reduced at unique

potentials based on their location on the Ag nanoparticle electrode surface. Later work further confirmed the site-specific redox activity of NB on Ag nanoparticles when performing super-localization EC-SERS along with spatially correlated SEM. At highly reducing potentials, the SERS emission is centered at junctions between nanoparticles, whereas at more oxidizing potentials the SERS emission is localized close to the center of the nanoparticle aggregates.[65] The change in centroid position as a function of applied potential implies that higher energies are required to reduce NB molecules in the nanoparticle junction. Overall, EC-SMSERS and super-localization EC-SERS demonstrate the power of SERS to study site-specific electrochemical reactions at the few to single molecule level.

6.1.2. Observing Catalytic Reactions

As demonstrated by EC-SMSERS studies, SMSERS is a powerful tool for monitoring site-specific chemical reactions. Recent efforts have also pushed towards studying heterogeneous catalysis at the single molecule limit. The metallic nanoparticles can serve both as the catalyst material and the SERS-substrate. In particular, many studies have focused on examining the model dimerization reaction of *para*-nitrothiophenol (*p*-NTP) or *para*-aminothiophenol (*p*-ATP) to 4,4-dimercaptoazobenzene (DMAB).[169–180]

Zhang et al., for example, explored the effect of *p*-NTP coverage on Au nanoparticles on DMAB formation.[169] At incubation concentrations greater than 5 x 10^{-8} M of *p*-NTP, the coverage of *p*-NTP on the Au nanoparticle surface is sufficiently dense such that dimerization to DMAB still occurs upon illumination. Below 5 x 10^{-8} M, the coverage of *p*-NTP is too sparse and there is no apparent DMAB formation on the Au nanoparticle surface. Therefore, the authors assume that there are 1-2 molecules in the Au nanoparticle

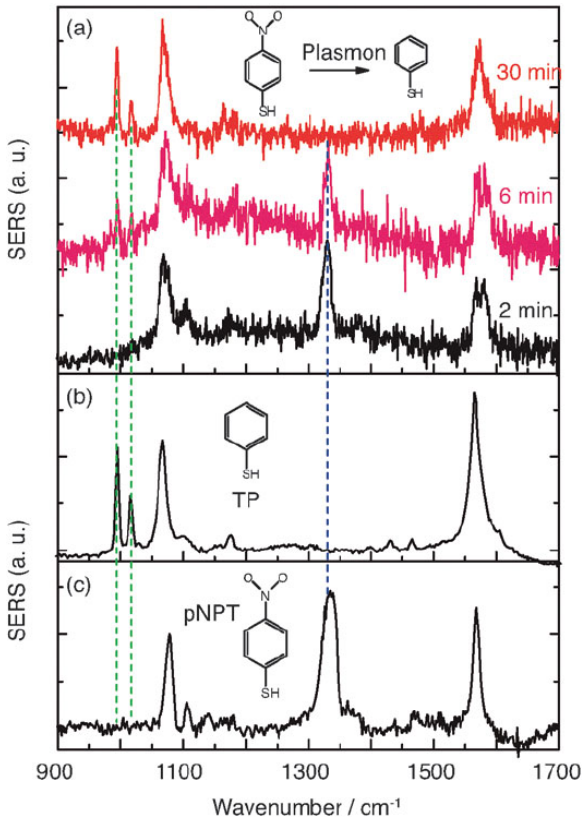

Figure 6.1. A) Time-dependent SERS spectra of reacting 10^{-9} M *p*-NTP on Au nanoparticles with $P_{ex} = 3$ mW after 2 (black trace), 6 (pink trace) and 30 (red trace) minutes. Over time, two peaks associated with TP appear and the major peak (~1340 cm^{-1}) of *p*-NTP disappears. B) and C) high coverage SERS spectra of TP and *p*-NTP, respectively. Reproduced from reference [169] with permission from the Royal Society of Chemistry.

hot spot junction. Upon sample illumination, however, new vibrational modes appeared indicating the cleavage of the nitro group of *p*-NTP to form thiophenol (TP) (Figure 6.1). They rationalize the formation of TP via plasmon-induced hot electron generation, which provides sufficient energy to cleave the nitro group from the *p*-NTP molecule. In a

separate study, Choi et al. demonstrated the heterogeneity of reactivity of single pairs of *p*-NTP molecules dimerizing to DMAB, which they attribute to the relative location of the *p*-NTP molecules within the hot spot junction.[171] They demonstrate "hot" and "mild" photoswitching regimes, as defined by two unique types of temporal fluctuations in the DMAB signal. These studies demonstrate the power of monitoring single molecule reactions on plasmonic nanoparticle surfaces using SERS, where understanding site-specific behavior is essential. As discussed in Chapter 2, a multi-analyte SERS approach could be utilized to rigorously prove SMSERS of catalyic reactions by using isotopically-substituted molecules, where the dimerization of isotope pairs (e.g., *p*-NTP or *p*-ATP) occur to form a single molecule.[57,170]

6.1.3. Detecting *Cis-Trans* Tautomerism

SMSERS can also be used to observe transient intermediates, such as the rare cis tautomeric form of porphycene, as studied by Gawinkowski and coworkers.[97] SMSERS detection of porphycene was proven using the isotopologue method. Statistically valid SMSERS detection occurred when the total isotopologue concentration of 1:1 porphycene-d_0:porphycene-d_{12} was 10^{-9} or 10^{-10} M. It is interesting to note that in each SMSERS histogram collected, more porphycene-d_0 counts were measured than porphycene-d_{12}, indicating that the porphycene-d_0 had a higher surface diffusion coefficient on the nanoparticle surface. This result highlights the importance of taking into account the subtle differences in molecular properties (e.g., Raman scattering cross section, diffusion coefficient) when conducting a statistically valid SMSERS proof as discussed in Chapter 2.[57]

After proving SM detection, the authors sought to observe the *cis* tautomeric form of porphycene, which had previously only been observed on Cu(110) single crystals using scanning tunneling microscopy. They relied on density functional theory calculations to predict that the major change of the Raman spectra was a 20 cm^{-1} blueshift in the band at 180 cm^{-1} between the *trans* and *cis* forms. Additionally, they predicted the appearance of a Raman peak at 1420 cm^{-1} upon formation of the *cis* form of the d_{12} isotopologue. Time trajectories of a single nanoparticle aggregate were taken of both isotopologues and instances of *trans-cis-trans* switching were observed. The authors observed the theoretically predicted peak shifts along with new modes and found that the tautomerization is independent of temperature; as they observe the *cis* form at both low temperature and at room temperature. As such, they attribute the tautomerization to a hot spot-dominated effect. This work demonstrates the potential for studying similar molecules such as substituted porphycenes and porphyrins with SMSERS, and how the nanoparticle hot spot environment can affect the chemical behavior of molecules.

6.1.4. Monitoring Host-Guest Interactions

In addition to the previous studies, SMSERS can monitor host-guest interactions, as demonstrated by Sigle and coworkers.[76] The authors used the host molecule cucurbit[7]uril (CB[7]) as a means of detecting single molecule binding events within a Au mirror-Au nanoparticle junction (GM-SERS configuration). Cucurbit[n]urils (CB[n]s) are macrocyclic molecules with a barrel-like structure consisting of a glycouril monomer unit where [n] is the total number of monomers in the CB[n] molecule.[181] CB[n]s are ideal for sensing

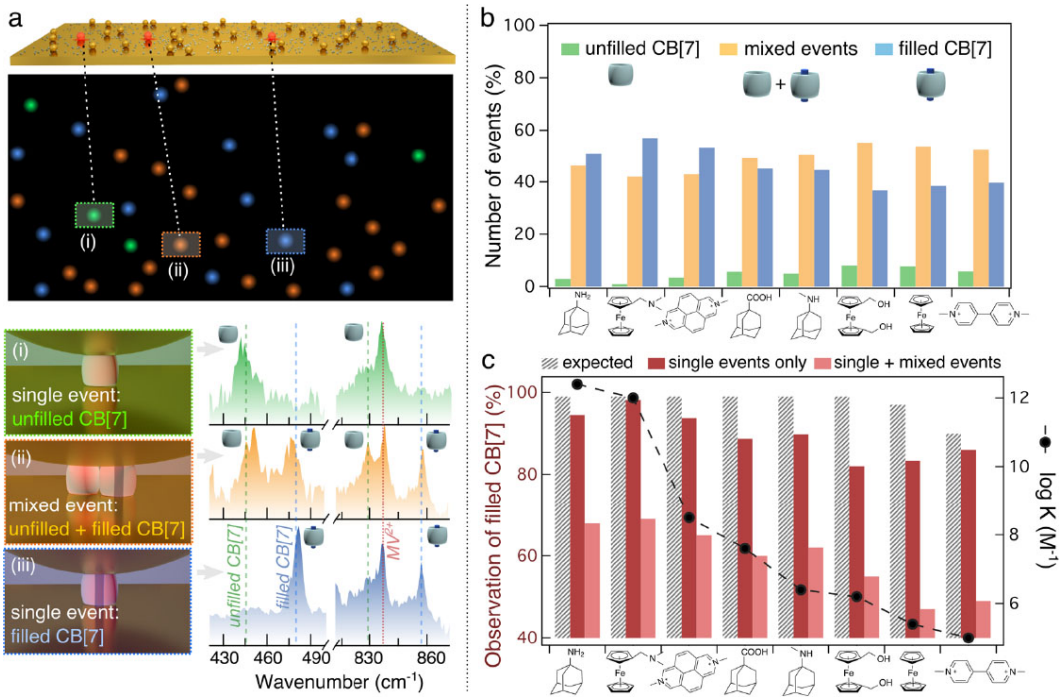

Figure 6.2. A) Schematic of the experimental set-up for CB[7] and MV^{2+} and representative SERS spectra of the characteristic CB[7] Raman modes at 440 and 830 cm^{-1} (green and blue dashed lines) and MV^{2+} modes (red dotted lines). Each spectrum corresponds to (i) unfilled CB[7] (green), (ii) a mix of filled and unfilled CB[7] (orange), and (iii) filled CB[7] (blue). B) Statistical representation of the number of events observed. C) Comparison of the number of times the signal from filled CB[7] was observed for single molecule and mixed events as a function of decreasing order of binding affinities of the guests for CB[7]. The overlaid black trace is the log of binding strengths of the guest molecules. Adapted with permission from reference [76]. Copyright 2016 American Chemical Society.

applications because when a single guest molecule binds in the CB[n] cavity, the CB[n] undergoes structural changes, which are readily detectable using Raman spectroscopy.[182] In the CB[7] SMSERS experiment, a Au mirror was incubated with CB[7] at sub-monolayer coverage. Then, Au nanoparticles were dropcast onto the sample in a GM-SERS configuration (Figure 1.8D). The authors claim bianalyte SMSERS spectra of either the empty CB[7] or filled CB[7] with 8 different molecules including methyl viologen (MV), adamantane, or various ferrocene derivatives. Binding events were indicated by the appearance of the guest molecule SERS spectra, as well as a -5 and 10 cm^{-1} shift in the 440 cm^{-1} mode of CB[7] (Figure 6.2). Despite the clear distinction between empty and filled CB[7] used to claim bianalyte SMSERS detection, nearly half of complex binding events detected indicated both filled and unfilled CB[7] for all guest molecules studied. While the molecular coverage of the SERS-active substrate needs to be optimized in order to rigorously demonstrate SMSERS, this work is a promising step forward towards using SMSERS to probe biologically relevant molecules including cellular metabolites[183] (e.g., pyruvate and lactate), proteins, and DNA.

6.2. Future Directions for SMSERS

As discussed in this chapter, SMSERS has matured into a powerful vibrational spectroscopy with applications in electrochemistry, catalysis, identifying intermediate species, and more. There are two main directions for future studies with SMSERS: 1) fundamental investigations and 2) applications of SM detection. The former will focus on improving the fundamental understanding, reproducibility, and generality of SMSERS. The latter will use our improved understanding to study relevant chemistries.

To further advance our fundamental understanding, future SMSERS studies should improve the reproducibility of nanoparticle fabrication for enhancing the Raman signal, develop methods for controlling molecular location, and increase hot spot density. Using more reproducible plasmonic structures, such as the NSL-nanopyramid arrays discussed in Chapter 3, would allow us to systematically investigate SERS mechanisms. Moreover, coupling controlled molecular location with higher hot spot densities would increase the statistical power of SMSERS, thereby strengthening experimental reproducibility and interpretation of single molecule chemistry. Similarly, applying the rigorous SMSERS proofs discussed in Chapter 2 will increase the robustness of SMSERS as an analytical technique. In addition, future studies should develop theoretical models to describe observed SM behaviors, such as the relative intensity fluctuations presented in Chapter 5. Combining theoretical calculations with experimental SMSERS promotes the study of molecular properties, providing detail on interactions between molecules and their environments that are normally obscured by ensemble averaging.

In future studies we also need to broaden the scope of molecules studiable with SMSERS. Expanding the molecular "toolbox," is crucial to generalize SMSERS for new applications. For instance, we highlight recent efforts towards studying biologically-relevant systems with SMSERS and efforts towards the detection of nonresonant molecules. To achieve nonresonant detection will likely require investigation of the chemical enhancement mechanisms and exploiting the additional signal enhancements.

Due to great strides in the fundamentals of SMSERS, the technique is now widely accepted and is being used to study relevant chemistries at the SM level. Electrochemistry and site-specific catalysis are a few fields where the vibrational characterization

of single molecules has provided new insight that cannot be gained from an ensemble-averaged experiment. In addition, single to few molecule level studies have been used to observe rare transient intermediates and monitor host-guest interactions. Future endeavors with SMSERS have potential to answer questions in photochemistry, acid-base chemistry, plasmon-driven chemistry, and more. Alternatively, in Chapter 4, we explore the potential use of SMSERS for measuring temperature in plasmonic cavities, wherein light is magnified and focused within nanoscale volumes. These plasmonic cavities are used in a broad array of technologies where knowledge of local temperatures is useful, including optoelectronics, catalysis, and sensing. These are a few of the exciting new prospects for application of SMSERS that will benefit from the combination of site-specific chemical and structural information.

References

(1) Ambrose, W. P.; Goodwin, P. M.; Jett, J. H.; Van Orden, A.; Werner, J. H.; Keller, R. A. *Chem. Rev.* **1999**, *99*, 2929–2956.

(2) Anger, P.; Bharadwaj, P.; Novotny, L. *Phys. Rev. Lett.* **2006**, *96*, 113002.

(3) Kinkhabwala, A.; Yu, Z.; Fan, S.; Avlasevich, Y.; Mullen, K.; Moerner, W. E. *Nat. Photon.* **2009**, *3*, 654–657.

(4) Kühn, S.; Håkanson, U.; Rogobete, L.; Sandoghdar, V. *Phys. Rev. Lett.* **2006**, *97*, 017402.

(5) Moerner, W. E.; Fromm, D. P. *Rev. Sci. Instrum.* **2003**, *74*, 3597–3619.

(6) Betzig, E.; Chichester, R. J. *Science* **1993**, *262*, 1422–1422.

(7) Gimzewski, J. K.; Joachim, C. *Science* **1999**, *283*, 1683–1688.

(8) Xie, X. S.; Dunn, R. C. *Science* **1994**, *265*, 361–361.

(9) Hayazawa, N.; Tarun, A.; Inouye, Y.; Kawata, S. *J. Appl. Phys.* **2002**, *92*, 6983–6986.

(10) Celedon, A.; Nodelman, I. M.; Wildt, B.; Dewan, R.; Searson, P.; Wirtz, D.; Bowman, G. D.; Sun, S. X. *Nano Lett.* **2009**, *9*, 1720–1725.

(11) Neuman, K. C.; Nagy, A. *Nat. Methods* **2008**, *5*, 491–505.

(12) Nie, S.; Emory, S. R. *Science* **1997**, *275*, 1102–1106.

(13) Kneipp, K.; Wang, Y.; Kneipp, H.; Perelman, L. T.; Itzkan, I.; Dasari, R. R.; Feld, M. S. *Phys. Rev. Lett.* **1997**, *78*, 1667–1670.

(14) Zrimsek, A. B.; Chiang, N.; Mattei, M.; Zaleski, S.; McAnally, M. O.; Chapman, C. T.; Henry, A.-I.; Schatz, G. C.; Van Duyne, R. P. *Chem. Rev.* **2016**, *Under Review*.

(15) Le Ru, E.; Blackie, E.; Meyer, M.; Etchegoin, P. *J. Phys. Chem. C* **2007**, *111*, 13794–13803.

(16) Kleinman, S. L.; Frontiera, R. R.; Henry, A.-I.; Dieringer, J. A.; Van Duyne, R. P. *Phys. Chem. Chem. Phys.* **2013**, *15*, 21–36.

(17) Dieringer, J. A.; McFarland, A. D.; Shah, N. C.; Stuart, D. A.; Whitney, A. V.; Yonzon, C. R.; Young, M. A.; Zhang, X.; Van Duyne, R. P. *Faraday Discuss.* **2006**, *132*, 9–26.

(18) Shim, S.; Stuart, C. M.; Mathies, R. A. *Chem. Phys. Chem.* **2008**, *9*, 697–699.

(19) Kleinman, S. L.; Ringe, E.; Valley, N.; Wustholz, K. L.; Phillips, E.; Scheidt, K. A.; Schatz, G. C.; Van Duyne, R. P. *J. Am. Chem. Soc.* **2011**, *133*, 4115–4122.

(20) Lawless, M. K.; Matheis, R. A. *J. Chem. Phys.* **1992**, *96*, 8037–8045.

(21) Willets, K. A.; Van Duyne, R. P. *Annu. Rev. Phys. Chem.* **2007**, *58*, 267–297.

(22) Camden, J. P.; Dieringer, J. A.; Wang, Y.; Masiello, D. J.; Marks, L. D.; Schatz, G. C.; Van Duyne, R. P. *J. Am. Chem. Soc.* **2008**, *130*, 12616–12617.

(23) Wustholz, K. L.; Henry, A.-I.; McMahon, J. M.; Freeman, R. G.; Valley, N.; Piotti, M. E.; Natan, M. J.; Schatz, G. C.; Duyne, R. P. V. *J. Am. Chem. Soc.* **2010**, *132*, 10903–10910.

(24) Schatz, G. C.; Van Duyne, R. P. In *Handbook of Vibrational Spectroscopy*; John Wiley and Sons, Ltd: Hoboken, NJ, 2006.

(25) Zhang, Q.; Moran, C. H.; Xia, X.; Rycenga, M.; Li, N.; Xia, Y. *Langmuir* **2012**, *28*, 9047–9054.

(26) Kneipp, K. *J. Phys. Chem. C* **2016**, *120*, 21076–21081.

(27) Morton, S. M.; Jensen, L. *J. Am. Chem. Soc.* **2009**, *131*, 4090–4098.

(28) Morton, S. M.; Ewusi-Annan, E.; Jensen, L. *Phys. Chem. Chem. Phys.* **2009**, *11*, 7424–7429.

(29) Lombardi, J. R.; Birke, R. L. *J. Phys. Chem. C* **2008**, *112*, 5605–5617.

(30) Kambhampati, P.; Child, C. M.; Foster, M. C.; Campion, A. *J. Chem. Phys.* **1998**, *108*, 5013–5026.

(31) Valley, N.; Greeneltch, N.; Van Duyne, R. P.; Schatz, G. C. *J. Phys. Chem. Lett.* **2013**, *4*, 2599–2604.

(32) Arenas, J. F.; Fernández, D. J.; Soto, J.; López-Tocón, I.; Otero, J. C. *J. Phys. Chem. B* **2003**, *107*, 13143–13149.

(33) Otto, A. *J. Raman Spectrosc.* **2005**, *36*, 497–509.

(34) Park, W.-H.; Kim, Z. H. *Nano Lett.* **2010**, *10*, 4040–4048.

(35) Kubin, R.; Fletcher, A. *J. Lumin.* **1982**, *27*, 455–462.

(36) Zhao, J.; Jensen, L.; Sung, J.; Zou, S.; Schatz, G. C.; Van Duyne, R. P. *J. Am. Chem. Soc.* **2007**, *129*, 7647–7656.

(37) Jensen, L.; Schatz, G. C. *J. Phys. Chem. A* **2006**, *110*, 5973–5977.

(38) Watanabe, H.; Hayazawa, N.; Inouye, Y.; Kawata, S. *J. Phys. Chem. B* **2005**, *109*, 5012–5020.

(39) Guthmuller, J.; Champagne, B. *J. Phys. Chem. A* **2008**, *112*, 3215–3223.

(40) Dieringer, J. A.; Lettan, R. B.; Scheidt, K. A.; Van Duyne, R. P. *J. Am. Chem. Soc.* **2007**, *129*, 16249–16256.

(41) Daré-Doyen, S.; Doizi, D.; Guilbaud, P.; Djedaïni-Pilard, F.; Perly, B.; Millié, P. *J. Phys. Chem. B* **2003**, *107*, 13803–13812.

(42) Kasha, M. *Radiat. Res.* **1963**, *20*, 55–70.

(43) Kasha, M.; Rawls, H.; El-Bayoumi, A. M. *Pure Appl. Chem.* **1965**, *11*, 371–392.

(44) Klingsporn, J. M.; Jiang, N.; Pozzi, E. A.; Sonntag, M. D.; Chulhai, D.; Seideman, T.; Jensen, L.; Hersam, M. C.; Duyne, R. P. V. *J. Am. Chem. Soc.* **2014**, *136*, 3881–3887.

(45) Michaels, A. M.; Jiang; Brus, L. *J. Phys. Chem. B* **2000**, *104*, 11965–11971.

(46) McFarland, A. D.; Young, M. A.; Dieringer, J. A.; Van Duyne, R. P. *J. Phys. Chem. B* **2005**, *109*, 11279–11285.

(47) Rodríguez-Lorenzo, L.; Álvarez-Puebla, R. A.; Pastoriza-Santos, I.; Mazzucco, S.; Stéphan, O.; Kociak, M.; Liz-Marzán, L. M.; García de Abajo, F. J. *J. Am. Chem. Soc.* **2009**, *131*, 4616–4618.

(48) Haynes, C. L.; Van Duyne, R. P. *J. Phys. Chem. B* **2001**, *105*, 5599–5611.

(49) Hulteen, J. C.; Treichel, D. A.; Smith, M. T.; Duval, M. L.; Jensen, T. R.; Van Duyne, R. P. *J. Phys. Chem. B* **1999**, *103*, 3854–3863.

(50) Jensen, T. R.; Schatz, G. C.; Van Duyne, R. P. *J. Phys. Chem. B* **1999**, *103*, 2394–2401.

(51) Jensen, T. R.; Malinsky, M. D.; Haynes, C. L.; Van Duyne, R. P. *J. Phys. Chem. B* **2000**, *104*, 10549–10556.

(52) Zrimsek, A. B.; Henry, A.-I.; Van Duyne, R. P. *J. Phys. Chem. Lett.* **2013**, *4*, 3206–3210.

(53) Fang, Y.; Seong, N.-H.; Dlott, D. D. *Science* **2008**, *321*, 388–392.

(54) Le Ru, E. C.; Etchegoin, P. G.; Meyer, M. *J. Chem. Phys.* **2006**, *125*, 204701.

(55) Etchegoin, P. G.; Lacharmoise, P. D.; Le Ru, E. C. *Anal. Chem.* **2008**, *81*, 682–688.

(56) Blackie, E. J.; Ru, E. C. L.; Etchegoin, P. G. *J. Am. Chem. Soc.* **2009**, *131*, 14466–14472.

(57) Zrimsek, A. B.; Wong, N. L.; Van Duyne, R. P. *J. Phys. Chem. C* **2016**, *120*, 5133–5142.

(58) Thompson, M. A.; Lew, M. D.; Moerner, W. E. *Annu. Rev. Biophys.* **2012**, *41*, 321–342.

(59) Huang, B.; Bates, M.; Zhuang, X. *Annu. Rev. Biochem.* **2009**, *78*, 993–1016.

(60) Willets, K. A.; Stranahan, S. M.; Weber, M. L. *J. Phys. Chem. Lett.* **2012**, *3*, 1286–1294.

(61) Willets, K. A. *Front. Phys.* **2014**, *9*, 3–16.

(62) Stranahan, S. M.; Willets, K. A. *Nano Lett.* **2010**, *10*, 3777–3784.

(63) Titus, E. J.; Weber, M. L.; Stranahan, S. M.; Willets, K. A. *Nano Lett.* **2012**, *12*, 5103–5110.

(64) Wilson, A. J.; Molina, N. Y.; Willets, K. A. *J. Phys. Chem. C* **2016**, *120*, 21091–21098.

(65) Weber, M. L.; Wilson, A. J.; Willets, K. A. *J. Phys. Chem. C* **2015**, *119*, 18591–18601.

(66) Weber, M. L.; Willets, K. A. *J. Phys. Chem. Lett.* **2011**, *2*, 1766–1770.

(67) Ahmed, A.; Gordon, R. *Nano Lett.* **2012**, *12*, 2625–2630.

(68) Wang, D.; Zhu, W.; Best, M. D.; Camden, J. P.; Crozier, K. B. *Nano Lett.* **2013**, *13*, 2194–2198.

(69) Haes, A. J.; Haynes, C. L.; McFarland, A. D.; Schatz, G. C.; Van Duyne, R. P.; Zou, S. *MRS Bull.* **2005**, *30*, 368–375.

(70) Haes, A. J.; Zou, S.; Schatz, G. C.; Van Duyne, R. P. *J. Phys. Chem. B* **2003**, *108*, 109–116.

(71) Vlçková, B.; Moskovits, M.; Pavel, I.; Šišková, K.; Sládková, M.; Šlouf, M. *Chem. Phys. Lett.* **2008**, *455*, 131–134.

(72) Yin, H. J.; Liu, L.; Shi, C. A.; Zhang, X.; Lv, M. Y.; Zhao, Y. M.; Xu, H. J. *Appl. Phys. Lett.* **2015**, *107*, 193106.

(73) Graham, D.; Thompson, D. G.; Smith, W. E.; Faulds, K. *Nat. Nano* **2008**, *3*, 548–551.

(74) Lim, D.-K.; Jeon, K.-S.; Hwang, J.-H.; Kim, H.; Kwon, S.; Suh, Y. D.; Nam, J.-M. *Nat. Nano* **2011**, *6*, 452–460.

(75) Liu, K.; Bai, Y.; Zhang, L.; Yang, Z.; Fan, Q.; Zheng, H.; Yin, Y.; Gao, C. *Nano Lett.* **2016**, *16*, 3675–3681.

(76) Sigle, D. O.; Kasera, S.; Herrmann, L. O.; Palma, A.; de Nijs, B.; Benz, F.; Mahajan, S.; Baumberg, J. J.; Scherman, O. A. *J. Phys. Chem. Lett.* **2016**, *7*, 704–710.

(77) Le Ru, E. C.; Grand, J.; Sow, I.; Somerville, W. R. C.; Etchegoin, P. G.; Treguer-Delapierre, M.; Charron, G.; Félidj, N.; Lévi, G.; Aubard, J. *Nano Lett.* **2011**, *11*, 5013–5019.

(78) Chen, H.-Y.; Lin, M.-H.; Wang, C.-Y.; Chang, Y.-M.; Gwo, S. *J. Am. Chem. Soc.* **2015**, *137*, 13698–13705.

(79) Ikeda, K.; Sato, J.; Fujimoto, N.; Hayazawa, N.; Kawata, S.; Uosaki, K. *J. Phys. Chem. C* **2009**, *113*, 11816–11821.

(80) Hu, J.; Tanabe, M.; Sato, J.; Uosaki, K.; Ikeda, K. *J. Am. Chem. Soc.* **2014**, *136*, 10299–10307.

(81) Ikeda, K.; Sato, J.; Uosaki, K. *J. Photochem. Photobiol., A* **2011**, *221*, 175–180.

(82) Wang, H.; Levin, C. S.; Halas, N. J. *J. Am. Chem. Soc.* **2005**, *127*, 14992–14993.

(83) Fang, C.; Brodoceanu, D.; Kraus, T.; Voelcker, N. H. *RSC Adv.* **2013**, *3*, 4288–4293.

(84) Tay, L.-L.; Hulse, J.; Kennedy, D.; Pezacki, J. P. *J. Phys. Chem. C* **2010**, *114*, 7356–7363.

(85) Moskovits, M. *J. Raman Spectrosc.* **2005**, *36*, 485–496.

(86) Zheng, Y.; Soeriyadi, A. H.; Rosa, L.; Ng, S. H.; Bach, U.; Justin Gooding, J. *Nat. Commun.* **2015**, *6*, 1–8.

(87) Treussart, F.; Clouqueur, A.; Grossman, C.; Roch, J.-F. *Opt. Lett.* **2001**, *26*, 1504–1506.

(88) Berezin, M. Y.; Achilefu, S. *Chem. Rev.* **2010**, *110*, 2641–2684.

(89) Darby, B. L.; Le Ru, E. C. *J. Am. Chem. Soc.* **2014**, *136*, 10965–10973.

(90) Bosnick, K. A.; Jiang; Brus, L. E. *J. Phys. Chem. B* **2002**, *106*, 8096–8099.

(91) Moyer, P. J.; Schmidt, J.; Eng, L. M.; Meixner, A. J.; Sandmann, G. W.; Dietz, H.; Plieth, W. *J. Am. Chem. Soc.* **2000**, *122*, 5409–5410.

(92) Andersen, P. C.; Jacobson, M. L.; Rowlen, K. L. *J. Phys. Chem. B* **2004**, *108*, 2148–2153.

(93) Kudelski, A.; Pettinger, B. *Chem. Phys. Lett.* **2000**, *321*, 356–362.

(94) Emory, S. R.; Jensen, R. A.; Wenda, T.; Han, M.; Nie, S. *Faraday Discuss.* **2006**, *132*, 249–259.

(95) Domke, K. F.; Zhang, D.; Pettinger, B. *J. Phys. Chem. C* **2007**, *111*, 8611–8616.

(96) Le Ru, E. C.; Meyer, M.; Etchegoin, P. G. *J. Phys. Chem. B* **2006**, *110*, 1944–1948.

(97) Gawinkowski, S.; Pszona, M.; Gorski, A.; Niedziolka-Jonsson, J.; Kaminska, I.; Nogala, W.; Waluk, J. *Nanoscale* **2016**, *8*, 3337–3349.

(98) Goulet, P. J. G.; Pieczonka, N. P. W.; Aroca, R. F. *J. Raman Spectrosc.* **2005**, *36*, 574–580.

(99) Goulet, P. J. G.; Aroca, R. F. *Anal. Chem.* **2007**, *79*, 2728–2734.

(100) Darby, B. L.; Etchegoin, P. G.; Le Ru, E. C. *Phys. Chem. Chem. Phys.* **2014**, *16*, 23895–23899.

(101) Weiss, A.; Haran, G. *J. Phys. Chem. B* **2001**, *105*, 12348–12354.

(102) Sharaabi, Y.; Shegai, T.; Haran, G. *Chem. Phys.* **2005**, *318*, 44–49.

(103) Kitahama, Y.; Enogaki, A.; Tanaka, Y.; Itoh, T.; Ozaki, Y. *J. Phys. Chem. C* **2013**, *117*, 9397–9403.

(104) Kitahama, Y.; Araki, D.; Yamamoto, Y. S.; Itoh, T.; Ozaki, Y. *Phys. Chem. Chem. Phys.* **2015**, *17*, 21204–21210.

(105) Wang, Z.; Rothberg, L. J. *J. Phys. Chem. B* **2005**, *109*, 3387–3391.

(106) Futamata, M.; Maruyama, Y.; Ishikawa, M. *J. Phys. Chem. B* **2004**, *108*, 13119–13127.

(107) Yamamoto, Y. S.; Ishikawa, M.; Ozaki, Y.; Itoh, T. *Front. Phys.* **2014**, *9*, 31–46.

(108) Itoh, T.; Iga, M.; Tamaru, H.; Yoshida, K.-i.; Biju, V.; Ishikawa, M. *J. Chem. Phys.* **2012**, *136*, 024703.

(109) Kitahama, Y.; Tanaka, Y.; Itoh, T.; Ozaki, Y. *Phys. Chem. Chem. Phys.* **2010**, *12*, 7457–7460.

(110) Dickson, R. M.; Cubitt, A. B.; Tsien, R. Y.; Moerner, W. E. *Nature* **1997**, *388*, 355–358.

(111) Zaleski, S.; Cardinal, M. F.; Klingsporn, J. M.; Van Duyne, R. P. *J. Phys. Chem. C* **2015**, *119*, 28226–28234.

(112) Etchegoin, P. G.; Le Ru, E. C. *Anal. Chem.* **2010**, *82*, 2888–2892.

(113) Etchegoin, P. G.; Le Ru, E. C.; Meyer, M. *J. Am. Chem. Soc.* **2009**, *131*, 2713–2716.

(114) Artur, C.; Le Ru, E. C.; Etchegoin, P. G. *J. Phys. Chem. Lett.* **2011**, *2*, 3002–3005.

(115) Goulet, P. J. G.; Pieczonka, N. P. W.; Aroca, R. F. *Anal. Chem.* **2003**, *75*, 1918–1923.

(116) Pozzi, E. A.; Zrimsek, A. B.; Lethiec, C. M.; Schatz, G. C.; Hersam, M. C.; Van Duyne, R. P. *J. Phys. Chem. C* **2015**, *119*, 21116–21124.

(117) Galloway, C. M.; Le Ru, E. C.; Etchegoin, P. G. *Phys. Chem. Chem. Phys.* **2009**, *11*, 7372–7380.

(118) Dos Santos, D. P.; Temperini, M. L. A.; Brolo, A. G. *J. Am. Chem. Soc.* **2012**, *134*, 13492–13500.

(119) Dos Santos, D. P.; Temperini, M. L. A.; Brolo, A. G. *J. Phys. Chem. C* **2016**, *120*, 20877–20885.

(120) Maher, R. C.; Galloway, C. M.; Le Ru, E. C.; Cohen, L. F.; Etchegoin, P. G. *Chem. Soc. Rev.* **2008**, *37*, 965–979.

(121) Fu, Y.; Dlott, D. D. *J. Phys. Chem. C* **2015**, *119*, 6373–6381.

(122) Dieringer, J. A.; Wustholz, K. L.; Masiello, D. J.; Camden, J. P.; Kleinman, S. L.; Schatz, G. C.; Van Duyne, R. P. *J. Am. Chem. Soc.* **2008**, *131*, 849–854.

(123) Etchegoin, P. G.; Meyer, M.; Blackie, E.; Le Ru, E. C. *Anal. Chem.* **2007**, *79*, 8411–8415.

(124) Blackie, E.; Le Ru, E. C.; Meyer, M.; Timmer, M.; Burkett, B.; Northcote, P.; Etchegoin, P. G. *Phys. Chem. Chem. Phys.* **2008**, *10*, 4147–4153.

(125) Weber, M. L.; Litz, J. P.; Masiello, D. J.; Willets, K. A. *ACS Nano* **2012**, *6*, 1839–1848.

(126) Meyer, S. A.; Ru, E. C. L.; Etchegoin, P. G. *J. Phys. Chem. A* **2010**, *114*, 5515–5519.

(127) Li, W.; Camargo, P. H. C.; Lu, X.; Xia, Y. *Nano Lett.* **2008**, *9*, 485–490.

(128) Lim, D.-K.; Jeon, K.-S.; Kim, H. M.; Nam, J.-M.; Suh, Y. D. *Nat. Mater.* **2010**, *9*, 60–67.

(129) Taylor, R. W.; Lee, T.-C.; Scherman, O. A.; Esteban, R.; Aizpurua, J.; Huang, F. M.; Baumberg, J. J.; Mahajan, S. *ACS Nano* **2011**, *5*, 3878–3887.

(130) Voelcker, N. H.; Brodoceanu, D.; Kraus, T.; Cheng, F. *RSC Adv.* **2013**, *3*, 4288–4293.

(131) Kleinman, S. L.; Bingham, J. M.; Henry, A. I.; Wustholz, K. L.; Van Duyne, R. P. *Proceedings of SPIE* **2010**, *7757*, 77570J.

(132) Alabastri, A.; Toma, A.; Malerba, M.; De Angelis, F.; Proietti Zaccaria, R. *ACS Photonics* **2015**, *2*, 115–120.

(133) Baffou, G.; Quidant, R. *Laser Photon. Revs.* **2013**, *7*, 171–187.

(134) Pissuwan, D.; Valenzuela, S. M.; Cortie, M. B. *Trends Biotechnol.* **2006**, *24*, 62–67.

(135) Adleman, J. R.; Boyd, D. A.; Goodwin, D. G.; Psaltis, D. *Nano Lett.* **2009**, *9*, 4417–4423.

(136) Garnett, E. C.; Cai, W.; Cha, J. J.; Mahmood, F.; Connor, S. T.; Greyson Christoforo, M.; Cui, Y.; McGehee, M. D.; Brongersma, M. L. *Nat. Mater.* **2012**, *11*, 241–249.

(137) Majumdar, A. *Annu. Rev. Mater. Sci.* **1999**, *29*, 505–585.

(138) Vetrone, F.; Naccache, R.; Zamarrón, A.; Juarranz de la Fuente, A.; Sanz-Rodríguez, F.; Maestro, L. M.; Rodriguez, E. M.; Jaque, D.; Solé, J. G.; Capobianco, J. A. *ACS Nano* **2010**, *4*, 3254–3258.

(139) Gao, Y.; Bando, Y. *Nature* **2002**, *415*, 599–599.

(140) Millen, J.; Deesuwan, T.; Barker, P.; Anders, J. *Nat. Nanotechnol.* **2014**, *9*, 425–429.

(141) Mecklenburg, M.; Hubbard, W. A.; White, E. R.; Dhall, R.; Cronin, S. B.; Aloni, S.; Regan, B. C. *Science* **2015**, *347*, 629–632.

(142) Maher, R. C.; Etchegoin, P. G.; Le Ru, E. C.; Cohen, L. F. *J. Phys. Chem. B* **2006**, *110*, 11757–11760.

(143) Fryling, M.; Frank, C. J.; McCreery, R. L. *Appl. Spectrosc.* **1993**, *47*, 1965–1974.

(144) McCreery, R. L., *Raman Spectroscopy for Chemical Analysis*; Winefordner, J. D., Ed.; John Wiley & Sons, Inc.: 2005; Vol. 225.

(145) Kip, B. J.; Meier, R. J. *Appl. Spectrosc.* **1990**, *44*, 707–711.

(146) Albrecht, A. C.; Hutley, M. C. *J. Chem. Phys.* **1971**, *55*, 4438–4443.

(147) Kneipp, K.; Wang, Y.; Kneipp, H.; Itzkan, I.; Dasari, R.; Feld, M. *Phys. Rev. Lett.* **1996**, *76*, 2444–2447.

(148) Haslett, T. L.; Tay, L.; Moskovits, M. *J. Chem. Phys.* **2000**, *113*, 1641–1646.

(149) Brolo, A.; Sanderson, A.; Smith, A. *Phys. Rev. B* **2004**, *69*, 045424.

(150) Maher, R. C.; Cohen, L. F.; Gallop, J. C.; Le Ru, E. C.; Etchegoin, P. G. *J. Phys. Chem. B* **2006**, *110*, 6797–6803.

(151) Maher, R. C.; Cohen, L. F.; Etchegoin, P.; Hartigan, H. J. N.; Brown, R. J. C.; Milton, M. J. T. *J. Chem. Phys.* **2004**, *120*, 11746–11753.

(152) Lee, P. C.; Meisel, D. *J. Phys. Chem.* **1982**, *86*, 3391–3395.

(153) Palik, E. D., *Handbook of optical constants of solids*; Academic press: 1998; Vol. 3.

(154) Sonntag, M. D.; Klingsporn, J. M.; Garibay, L. K.; Roberts, J. M.; Dieringer, J. A.; Seideman, T.; Scheidt, K. A.; Jensen, L.; Schatz, G. C.; Van Duyne, R. P. *J. Phys. Chem. C* **2012**, *116*, 478–483.

(155) Sonntag, M. D.; Chulhai, D.; Seideman, T.; Jensen, L.; Van Duyne, R. P. *J. Am. Chem. Soc.* **2013**, *135*, 17187–17192.

(156) Kleinman, S. L.; Sharma, B.; Blaber, M. G.; Henry, A.-I.; Valley, N.; Freeman, R. G.; Natan, M. J.; Schatz, G. C.; Van, D. R. P. *J. Am. Chem. Soc.* **2013**, *135*, 301–308.

(157) Pozzi, E. A.; Sonntag, M. D.; Jiang, N.; Chiang, N.; Seideman, T.; Hersam, M. C.; Duyne, R. P. V. *J. Phys. Chem. Lett.* **2014**, *5*, 2657–2661.

(158) Sonntag, M. D.; Pozzi, E. A.; Jiang, N.; Hersam, M. C.; Duyne, R. P. V. *J. Phys. Chem. Lett.* **2014**, *5*, 3125–3130.

(159) Lombardi, J. R.; Birke, R. L.; Haran, G. *J. Phys. Chem. C* **2011**, *115*, 4540–4545.

(160) Gu, G. H.; Suh, J. S. *J. Raman Spectrosc.* **2010**, *41*, 624–627.

(161) Tadayyoni, M. A.; Farquharson, S.; Li, T. T. T.; Weaver, M. J. *J. Phys. Chem.* **1984**, *88*, 4701–4706.

(162) Oja, S. M.; Fan, Y.; Armstrong, C. M.; Defnet, P.; Zhang, B. *Anal. Chem.* **2016**, *88*, 414–430.

(163) Lemay, S. G.; Kang, S.; Mathwig, K.; Singh, P. S. *Acc. Chem. Res.* **2013**, *46*, 369–377.

(164) Mathwig, K.; Aartsma, T. J.; Canters, G. W.; Lemay, S. G. *Annu. Rev. Anal. Chem.* **2014**, *7*, 383–404.

(165) Cortés, E.; Etchegoin, P. G.; Le Ru, E. C.; Fainstein, A.; Vela, M. E.; Salvarezza, R. C. *J. Am. Chem. Soc.* **2010**, *132*, 18034–18037.

(166) Cortés, E.; Etchegoin, P. G.; Le Ru, E. C.; Fainstein, A.; Vela, M. E.; Salvarezza, R. C. *J. Am. Chem. Soc.* **2013**, *135*, 2809–2815.

(167) Wang, Y.; Sevinc, P. C.; He, Y.; Lu, H. P. *J. Am. Chem. Soc.* **2011**, *133*, 6989–6996.

(168) Wilson, A. J.; Willets, K. A. *Nano Lett.* **2014**, *14*, 939–945.

(169) Zhang, Z.; Deckert-Gaudig, T.; Singh, P.; Deckert, V. *Chem. Commun.* **2015**, *51*, 3069–3072.

(170) Brooks, J. L.; Frontiera, R. R. *J. Phys. Chem. C* **2016**, *120*, 20869–20876.

(171) Choi, H.-K.; Park, W.-H.; Park, C.-G.; Shin, H.-H.; Lee, K. S.; Kim, Z. H. *J. Am. Chem. Soc.* **2016**, *138*, 4673–4684.

(172) Dong, B.; Fang, Y.; Chen, X.; Xu, H.; Sun, M. *Langmuir* **2011**, *27*, 10677–10682.

(173) Huang, Y.-F.; Zhu, H.-P.; Liu, G.-K.; Wu, D.-Y.; Ren, B.; Tian, Z.-Q. *J. Am. Chem. Soc.* **2010**, *132*, 9244–9246.

(174) Kang, L.; Xu, P.; Zhang, B.; Tsai, H.; Han, X.; Wang, H.-L. *Chem. Commun.* **2013**, *49*, 3389–3391.

(175) Ren, X.; Tan, E.; Lang, X.; You, T.; Jiang, L.; Zhang, H.; Yin, P.; Guo, L. *Phys. Chem. Chem. Phys.* **2013**, *15*, 14196–14201.

(176) Takeyasu, N.; Kagawa, R.; Sakata, K.; Kaneta, T. *J. Phys. Chem. C* **2016**, *120*, 12163–12169.

(177) Van Schrojenstein Lantman, E. M.; Deckert-Gaudig, T.; Mank, A. J. G.; Deckert, V.; Weckhuysen, B. M. *Nat. Nano* **2012**, *7*, 583–586.

(178) Xu, J.-F.; Liu, G.-K. *Spectrochim. Acta, Part A* **2015**, *138*, 873–877.

(179) Xu, J.-F.; Luo, S.-Y.; Liu, G.-K. *Spectrochim. Acta, Part A* **2015**, *143*, 35–39.

(180) Zhang, M.; Zhao, L.-B.; Luo, W.-L.; Pang, R.; Zong, C.; Zhou, J.-Z.; Ren, B.; Tian, Z.-Q.; Wu, D.-Y. *J. Phys. Chem. C* **2016**, *120*, 11956–11965.

(181) Masson, E.; Ling, X.; Joseph, R.; Kyeremeh-Mensah, L.; Lu, X. *RSC Adv.* **2012**, *2*, 1213–1247.

(182) Chen, Y.; Klimczak, A.; Galoppini, E.; Lockard, J. V. *RSC Adv.* **2013**, *3*, 1354–1358.

(183) Lussier, F.; Brulé, T.; Vishwakarma, M.; Das, T.; Spatz, J. P.; Masson, J.-F. *Nano Lett.* **2016**, *16*, 3866–3871.

(184) Morris, H. R.; C. Hoyt, C.; Miller, P.; Treado, P. J. *Appl. Spectrosc.* **1996**, *50*, 805–811.

(185) Martin, M. M.; Lindqvist, L. *J. Lumin.* **1975**, *10*, 381–390.

APPENDIX A

Towards Nonresonant SMSERS

Achieving reliable SM detection of nonresonant molecules would significantly advance the field of SMSERS. As discussed in Chapter 1 Section 1.4, to achieve SM detection of nonresonant molecules requires EFs on the order of 10^9-10^{11} (typical nonresonant cross sections of $\sim 10^{-29}$ to 10^{-30} cm^2 sr^{-1} molecule^{-1}). Nonresonant SMSERS detection has been claimed for BPE with a benzotriazole dye acting as the bianalyte partner to verify SM detection.[56] The proof of SMSERS, however, does not meet the rigorous thresholds proposed in Chapter 2. In an attempt to rigorously achieve SMSERS with nonresonant molecules, we used the isotopologue approach with commercially available 4,4'-Bipyridine (BPY-d_0) and its deuterated analog (BPY-d_8).

A.1. Experimental Methods

For this experiment, 40 μL of 50-fold concentrated borohydride-reduced Ag colloids (synthesis provided in 2.2.1) were dropcast onto a 45 nm thick Ag mirror prepared via thermal evaporation (PVD75 Lesker) on glass coverslips (#1.5, 25 mm). The aggregated colloids were dried in a small circle ($\sim$0.5-1 mm^2) to obtain high nanoparticle coverage and, therefore, a higher hot spot density. This is essential to increase the likelihood of locating a BPY molecule in a highly enhancing hot spot. The Ag mirror was implemented to aid in reflecting additional Raman scattering into the objective. Onto the dropcast colloids, 50 μL mixture of 2x10^{-9} M BPY-d_0 and BPY-d_8 was incubated for 30 sec. The SMSERS

substrate was then flashed dried with N_2 to remove the excess solution. Borohydride-reduced Ag colloids were selected because they do not have an organic capping agent, which can provide stronger Raman scattering than the analyte of interest.

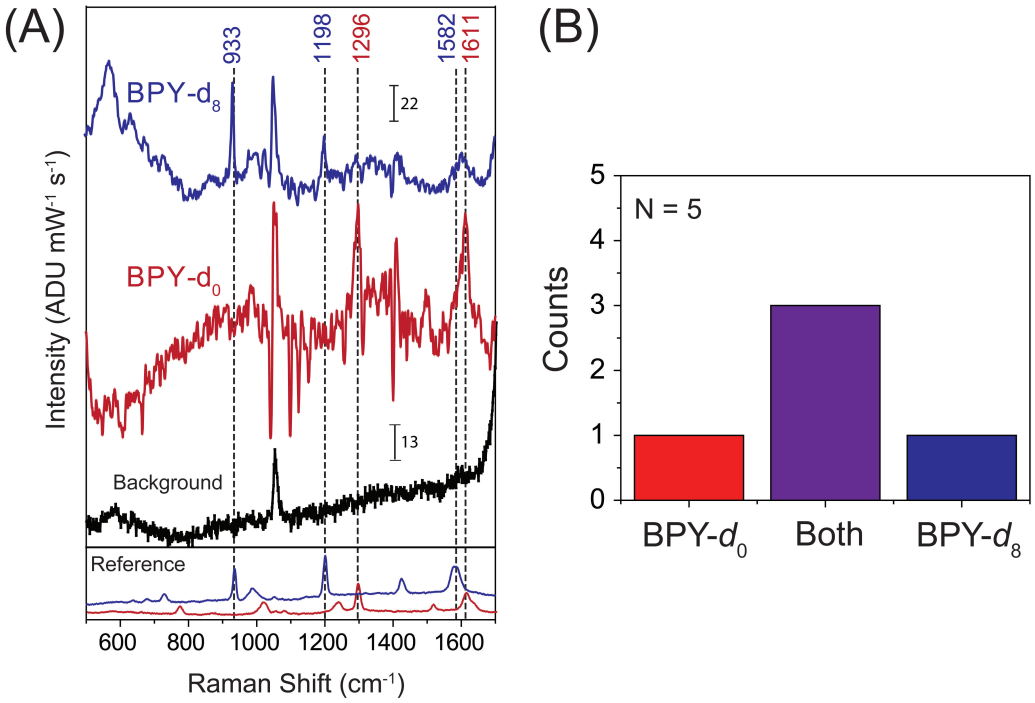

Figure A.1. A) Spectra of BPY-d_0 (red) and BPY-d_8 (blue) collected near SM level molecular coverage. A blank Ag colloid background spectrum is shown in black. Reference spectra were collected with Ag colloids incubated in 1 mM BPY-d_0 or BPY-d_8. B) Histogram of counts collected from Ag colloids incubated with a mixture of $2\text{x}10^{-9}$ BPY-d_0 and BPY-d_8.

The SMSERS substrates were scanned with a piezo-controlled stage (E-710 Digital PZT) with a step size of 5 μm in the x- and y-directions. The step size was chosen to be larger than the laser spot size ($\sim$1 μm^2) to limit exposure of the molecules to the laser during long scans. At each step of the scan, a spectrum was collected for 15 seconds

with an incident power of 207 μW. The SMSERS signal was collected in a backscattering geometry on an inverted microscope (Nikon TE300) with a 100× air objective (Nikon, NA = 0.9). The excitation wavelength was 532 nm (Spectra-Physics, Millenia X). A long-pass filter was used to filter the Rayleigh scattering (Semrock, LP03-532RS-25). The collected signal was dispersed with a 1200 grooves/mm grating and detected with a liquid N_2-cooled CCD (Action 300i, Spec-10 400B).

A.2. Current Results

Figure A.1A provides spectra of BPY-d_0 (red) and BPY-d_8 (blue) collected from Ag colloids with near SM level coverage. The background signal from blank Ag colloids is shown (black). The reference spectra were collected from Ag colloids incubated with high coverage (1 mM) of BPY-d_0 or BPY-d_8. Peaks used for the identification of both analytes are indicated on the plot. Notably, the large peak shift from 1296 to 1195 cm^{-1} upon deuteration is used. Figure A.1B provides the histogram of counts collected for these experiments at N = 5.

The collection efficiency for the nonresonant SMSERS experiments was very low due to the rarity of locating a molecule in a highly enhancing hot spot. Specifically, we observed 1 event with BPY for every 616 scan spectra. If this trend continued, to achieve a minimum of 50 counts for verifying SMSERS would require the collection of 30,800 spectra. At 15 sec per acquisition (necessary to achieve adequate signal to noise) and 1 sec scan stage delays between spectra, data collection would require a 137 hours. In addition, the histogram indicates molecular coverage at the few-molecule level. To reach single molecule level coverage would require lowering the concentration, further decreasing

the collection efficiency, and increasing data collection time. While we believe rigorously verifying SMSERS with nonresonant molecules is possible, the current approach is not experimentally practical. Therefore, in order to expand the scope of molecules which can be studied with SMSERS, it is necessary to gain additional enhancement from avenues besides molecular resonance.

A.3. Potential Avenues for Detecting Nonresonant Molecules

1. Physically smaller molecules will be able to penetrate deeper into nanoparticle junctions. Due to larger EM fields in these crevice sites, smaller molecules may experience up to 100× greater signal strength, aiding in detection. Thiocyanate (SCN^-) is a good candidate because of its small size, large Raman scattering cross section, strong affinity to Ag, and commercial availability of its isotopologues ($S^{13}CN^-$). Additional options include $CN^-/^{13}CN^-$ and $N{=}N{=}N^-/^{15}N{=}N{=}N^-$.

2. Theoretical calculations by Morton et, al., have found that by tailoring an analyte with different functional groups, the chemical enhancement can surpass 10^3 due to changes in the energy difference between the HOMO of the metal and the LUMO of the analyte.[27] Utilization of chemical and EM enhancement may help probe a wider spectrum of molecular systems.

3. Utilization of a wide-field data collection scheme for Raman imaging of large areas with a high-resolution liquid crystal tunable filter (LCTF) or acousto optical tunable fitler (AOTF),[184] could improve the data collection efficiency and decrease data collection time in combination with the above approaches.

APPENDIX B

Towards Monitoring Acid-Base Chemistry with SMSERS

The future of SERS is to monitor single molecule chemistry. In Chapter 6, we discussed several applications of single molecule chemistry including electrochemistry and catalysis. Acid-base chemistry is another potential avenue for study. The goal being to elucidate site-specific properties of proton exchange between the analyte and solution. In this appendix, we cover experimental considerations and potential analytes for the study of monitoring acid-base chemistry.

B.1. Experimental Considerations

1. We have verified that Ag colloids are stable in highly acidic and basic solutions, but in order to prevent desorption of the colloids into the solution, the colloids must be covalently tethered to the glass coverslips. The procedure for silanization is as follows: *a)* piranha clean glass coverslips immediately before silanization, *b)* base-treat glass coverslips for a minimum of 30 min at ∼70°C, *c)* remove coverslips from the base-treatment, rinse thoroughly with Millipore water, dry completely, and place into a solution of (3-Mercaptopropyl)trimethoxysilane (MPS) (0.25 mL in 25 mL HPLC grade 2-propanol at ∼70°C), *d)* leave the coversips in the MPS solution for 6-12 minutes, remove, and rinse throughly with 2-propanol and then with Millipore water, *e)* immediately dropcast colloid/dye mixture onto coverslips and allow to dry in a N_2 environment, *f)* rinse with

water to remove any excess Ag colloids which did not stick to the glass coverslip. (3-Aminopropyl)trimethoxysilane (APS) is an alternative silanizing agent.

2. SMSERS can be verified using: *a)* a bianalyte partner which is stable under highly acidic and basic conditions and meets the requirements discussed in Chapter 2, *b)* an isotopically-edited partner, *c)* a single analyte in a 50:50 mixture of D_2O/H_2O. The latter will require significant peak shifts between the deuterated and nondeuterated forms for unambiguous identification.

3. The proton exchange can be initiated via altering the solution pH or using a photo-induced proton donor such as Pyranine. When exciting with a ∼400 nm laser pyranine deprotonates. In addition, we observed no SERS or fluorescence of pyarnine at 532 nm excitation, meaning its presence will not provide background signal.

B.2. Experimental Requirements for the Analyte of Study

1. The ideal analyte will be a resonant dye with an acid-base functional group such as an amine, carboxylic acid, or hydroxyl group. The analyte should reversibly exchange protons with the environment either through altering solution pH or photo-drive proton transfers.

2. The analyte requires a clearly distinguishable spectral change between the acidic and basic forms.

3. The analyte should bind to the nanoparticle surface to prevent desorption, signal loss, and residual fluorescence from unbound molecules.

4. The analyte should be in resonance with the excitation wavelength in both its acidic and basic form. This will allow the chemical signature of the proton exchange to be

observed instead of using signal loss to signify the event. Alternatively, a two laser experiment can be performed with one laser being on resonance with the acidic form and one on resonance with the basic form. Potential analytes for investigation are shown below:

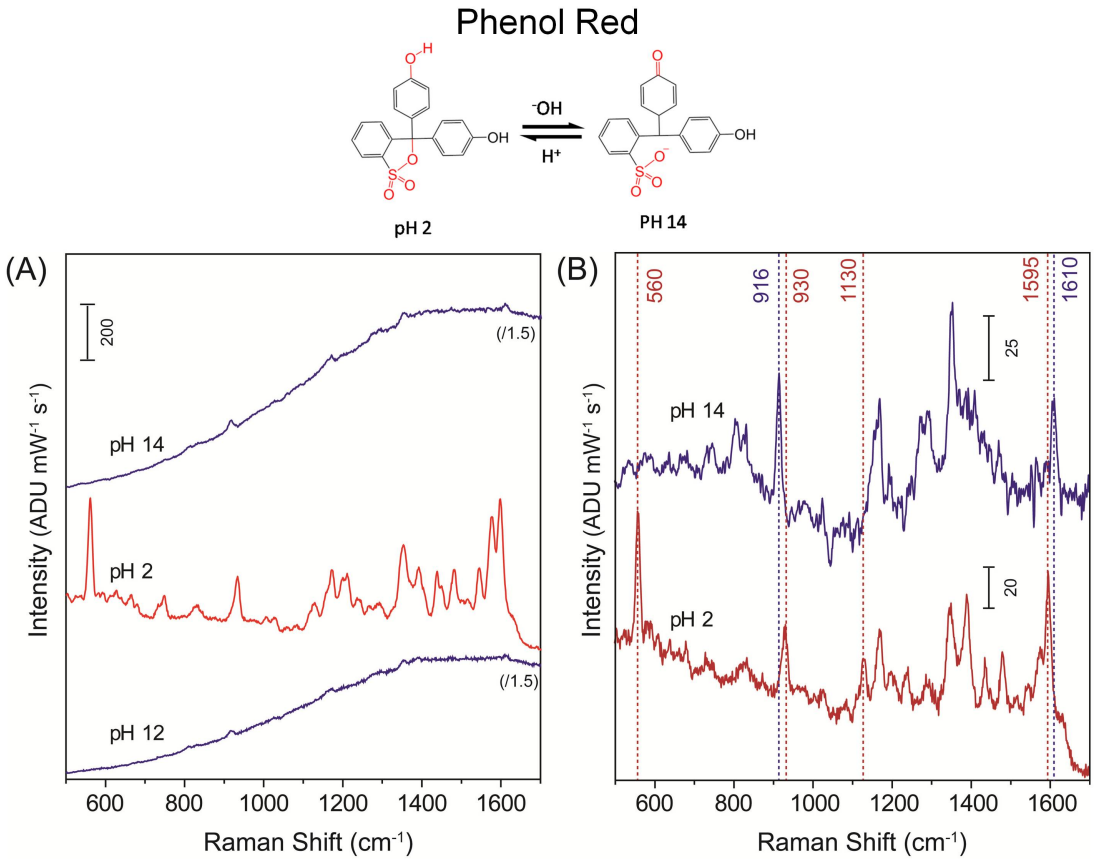

Figure B.1. Structural changes for phenol red under acidic (pH 2) and basic (pH 12-14) conditions. A) Ensemble spectra of phenol red collected from Ag colloids at the indicated pH, showing the structural changes are reversible. A few μL of HCL and NaOH were added to the Ag colloid/dye mixture to alter the pH. A strong fluorescence background grows in under basic conditions. B) Background subtracted spectra to clearly show the Raman peak shifts between the acidic and basic forms of phenol red.

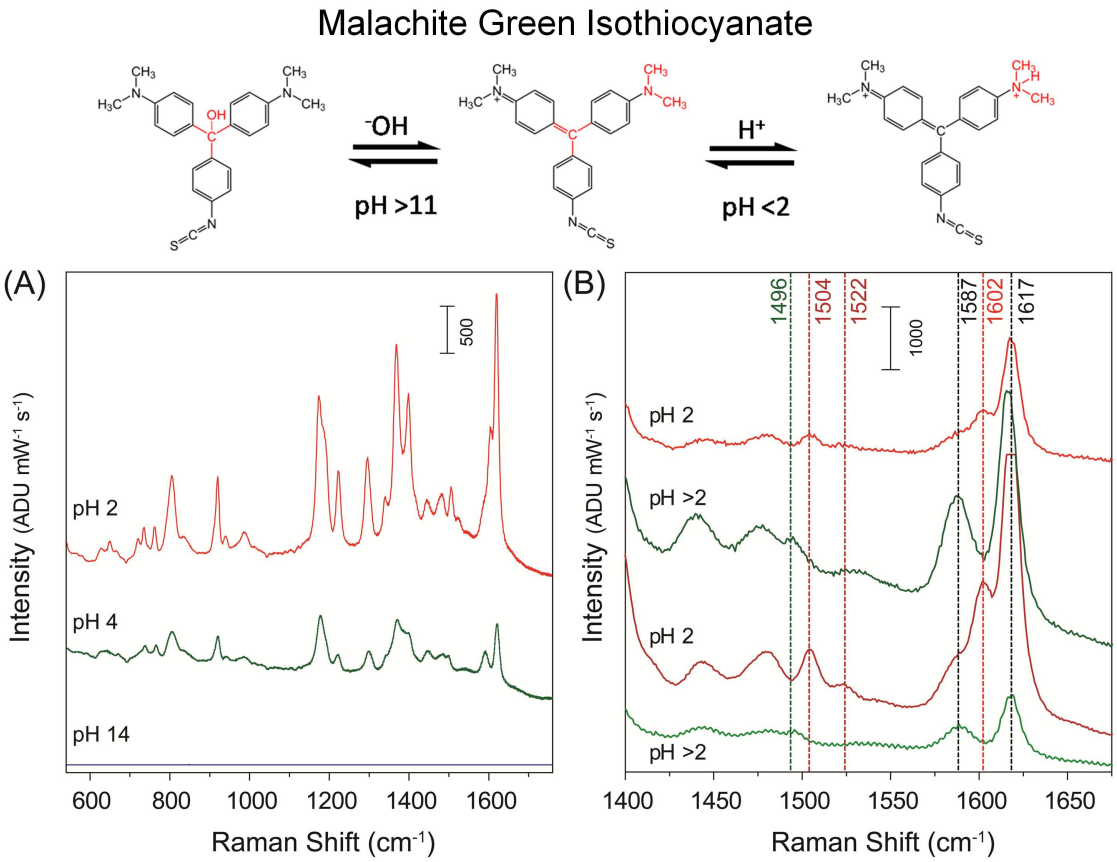

Figure B.2. Structural changes of malachite green isothiocyanate under acidc, neutral, and basic conditions. A) Ensemble SERS spectra from Ag colloids at the indicated pH. No signal is observed at pH 14. B) The pH changes are reversible (added a few μL of HCL and/or NaOH to the Ag colloid/dye mixture). Peaks grows in at 1602, 1505, and 1522 cm^{-1} under acidic conditions. However, the 1505 and 1522 cm^{-1} are very weak and likely undetectable at the SM level and the 1602 cm^{-1} peak overlaps with the 1587 and 1616 cm^{-1} peaks, complicating identification.

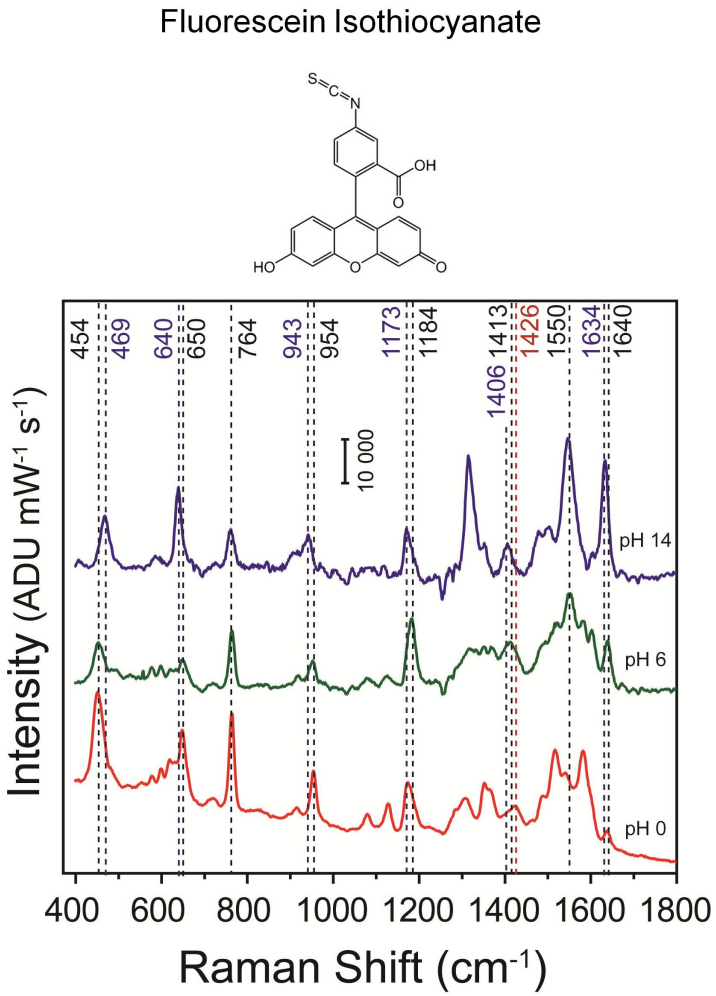

Figure B.3. Structure of fluorescein isothiocyanate. A) Ensemble spectra of fluorescein isothiocyanate collected from Ag colloids at the indicated pH. Multiple spectral shifts are indicated on the spectra. At a pH = 6 the spectra appears to be a combination of the highly acidic (pH = 0) and basic (pH = 14) spectra, indicating a mixture of species at this pH. Six forms of fluorescein have been identified in the literature,[185] potentially complicating spectral analysis.

B.3. Summary of Potential Analytes

All of the potential candidates mentioned above have advantages and disadvantages. RBITC was also investigated (not shown) but distinguishable spectral shifts were not observed at different pH. Phenol red a has clearly distinguishable spectral change between the acidic and basic forms of the molecule, but the molecule does not bind to the nanoparticle surface. Synthesizing the molecule with a linker group (e.g., thiol or SCN) could overcome this challenge. Malachite green isothiocyanate, on the other hand, strongly binds to the nanoparticle surface, but the spectral change is very minimal and may be challenging to distinguish at the SM level. Fluorescein isothiocyanate also strongly binds to the surface and undergoes multiple spectral shifts for identification, but has six possible forms (cation, 3 neutral isomers, monoanion, and dianion)[185] which may complicate spectral analysis.